Solution aggregation and interfacial adsorption of novel acyl-L-carnitine surfactants

A thesis submitted to The University of Manchester for the degree of Doctor of Philosophy in the Faculty of Science and Engineering

2021

Huayang Liu

School of Physics and Astronomy

Table of Contents

List of Figures

Chapter 1 Introduction

Chapter 2 Dynamic light scattering (DLS), small angle neutron scattering (SANS) and neutron reflection (NR)

wavenumber of reflected neutron is k_f. 2θ is the scattering angle. Q is the momentum transfer and d is the thickness of the layer. ρ_l, ρ_s and ρ_e are the SLD values of the layer, substrate and environment. The illuminated area from the neutron beam is constrained by $-L_x < x < L_x$ and $-L_y < y < L_y$.

Chapter 3 Surface adsorption and solution aggregation of a novel lauroyl-L-carnitine surfactant

Chapter 3 supporting information

Chapter 4 How do acyl chain lengths of acyl-L-carnitines affect their surface adsorption and solution aggregation?

Chapter 4 supporting information

Chapter 5 Structural features of interfacially adsorbed acyl-L-carnitines

Chapter 5 supporting information

List of Tables

Chapter 1 Introduction

Chapter 2 Dynamic light scattering (DLS), small angle neutron scattering (SANS) and neutron reflection (NR).

Chapter 3 Surface adsorption and solution aggregation of a novel lauroyl-L-carnitine surfactant

Chapter 3 supporting information

Chapter 4 How do acyl chain lengths of acyl-L-carnitines affect their surface adsorption and solution aggregation?

Chapter 4 supporting information

Chapter 5 Structural features of interfacially adsorbed acyl-L-carnitines

Chapter 5 supporting information

Abstract

Solution aggregation and interfacial adsorption of novel acyl-L-carnitine surfactants

L-carnitine has been widely used as a nutrition supplement to help with weight loss, as it plays an important role in the generation of energy by the transport of fatty acids into mitochondria. Acyl-L-carnitines are biosurfactants with amphiphilic behavior and potential in antimicrobial and personal care applications. However, the understanding of their physicochemical properties remains lacking, limiting the development of their practical applications. The work in this thesis has focused on the physicochemical properties including solubility, stability, solution aggregation and interfacial adsorption (air/liquid and solid/liquid interfaces) of this novel series of biosurfactants.

The aqueous solubility of acyl-L-carnitines (C_nLC, n=12, 14 and 16) is influenced by temperature, pH and acyl chain length as investigated by dynamic light scattering (DLS). Our studies showed that $C_{12}LC$ has the highest solubility followed by $C_{14}LC$ and $C_{16}LC$. Higher temperature and lower pH could improve their solubility. The hydrodynamic radii of the micelles of C_nLC were firstly measured by DLS. The size and shape of the micelles were further investigated by small angle neutron scattering (SANS) with protonated and deuterated samples. Our studies have revealed that the micelles of C_nLC have a core-shell spherical structure. The thickness of the shell of the three C_nLC micelles is similar as the shell consists of the same head groups (L-carnitines) and water molecules. The micellar shape of C_nLC micelles remained unchanged, but pH-responsive carboxyl groups in head groups switched the zwitterionic surfactants at neutral pH into cationic surfactants in an acidic environment. As the pH decreases, C_nLC micelles carry more positive charges on the micellar surface leading to stronger electrostatic repulsion between micelles. However, this repulsive interaction could be screened under high ionic strength.

Interfacial adsorption was studied at two typical interfaces including air/liquid and solid/liquid interfaces. At the air/water interface, surface tension measurements were used to determine their critical micelle concentrations (CMCs). The surface excess and area per molecule of C_nLC at the air/water interface were calculated in combination with the Gibbs equation. The structure of the adsorbed layer was examined by neutron reflection (NR) by taking advantage of deuterium labelled C_nLCs. Our studies showed that the C_nLC molecules form a monolayer at the air/water interface with the tilted acyl chains in the air. The thickness of the layer, adsorbed amount, area per molecule and tilting angle are dependent on concentration, acyl chain length, pH, and ionic strength. At the SiO_2/water interface, the adsorption dynamics and equilibrium adsorption amount were firstly investigated by spectroscopic ellipsometry (SE) and NR was used to provide detailed structural information. C_nLC molecules tended to form surface aggregates at the interface which then became into the surfactant bilayer as the concentration increased.

This project provided a detailed investigation of the solution aggregation and interfacial adsorption of C_nLC under different environmental conditions. These features make C_nLCs potentially more attractive biosurfactants than many synthetic ones.

Declaration

I confirm that no portion of the work referred to in the thesis has been submitted in support of an application for another degree or qualification of this or any other university or other institute of learning.

Huayang Liu

20 Sep 2021

Copyright Statement

i. The author of this thesis (including any appendices and/or schedules to this thesis) owns certain copyright or related rights in it (the "Copyright") and s/he has given the University of Manchester certain rights to use such Copyright, including for administrative purposes.

ii. Copies of this thesis, either in full or in extracts and whether in hard or electronic copy, may be made only in accordance with the Copyright, Designs and Patents Act 1988 (as amended) and regulations issued under it or, where appropriate, in accordance with licensing agreements which the University has from time to time. This page must form part of any such copies made.

iii. The ownership of certain Copyright, patents, designs, trademarks and other intellectual property (the "Intellectual Property") and any reproductions of copyright works in the thesis, for example, graphs and tables ("Reproductions"), which may be described in this thesis, may not be owned by the author and may be owned by third parties. Such Intellectual Property and Reproductions cannot and must not be made available for use without the prior written permission of the owner(s) of the relevant Intellectual Property and/or Reproductions.

iv. Further information on the conditions under which disclosure, publication and commercialisation of this thesis, the Copyright and any Intellectual Property and/or Reproductions described in it may take place is available in the University IP Policy (see http://documents.manchester.ac.uk/DocuInfo.aspx?DocID=24420), in any relevant Thesis restriction declarations deposited in the University Library, the University Library's regulations (see http://www.library.manchester.ac.uk/about/regulations/) and in the University's policy on Presentation of Theses.

Acknowledgments

First and foremost, I would like to express my sincere gratitude to my supervisor, Prof. Jian Lu, for his guidance, suggestions and help over my PhD. He gave me a meaningful project which started my research career.

I wish to thank the studentship support from Lonza, Rutherford Appleton Laboratory and the University of Manchester.

I would like to thank Prof. Robert Thomas and Prof. Jordan Petkov, who shared their invaluable experience with me. Without their advice and assistance, the project I have done is impossible.

A big thank you to Dr John Webster, Dr Peixun Li, Dr Stephen King, Dr Mario Campana, Dr Kun Ma and other instrument scientists in ISIS and ILL for the knowledge of neutron scattering and assistance on neutron experiments. They helped me a lot with neutron data reduction and analysis during my experiments in ISIS and ILL.

I appreciate the assistance and support from all members of our biological physics group: Dr Thomas Waigh, Mr Jamie Fearnley, Dr Zongyi Li, Dr Jing Zhang, Dr Charles Smith, Dr Daniela Ciumac, Dr Ruiheng Li, Dr Xuzhi Hu, Dr Haoning Gong, Dr Jessica Carter, Dr Sean Ruane, Ke Fa, Lin Zhang, Mingrui Liao, Peter Hollowell, Kangcheng Shen, Zeyuan Zhuang and Tianhao Ge.

Thanks for the help and encouragement from all my friends. I am very grateful for the beautiful moments we had together and the happiness they brought to my life.

Finally, I want to thank my parents for the fantastic life given to me. Thanks to them for always supporting my work and decisions, and for believing in my ability.

List of Publications

1. **H. Liu**, X. Hu, Z. Li, K. Fa, H. Gong, K. Ma, M. Liao, P. Li, J.R. Webster, J.T. Petkov, R.K. Thomas, J.R. Lu, Surface Adsorption and Solution Aggregation of a Novel Lauroyl-L-Carnitine Surfactant, *Journal of Colloid and Interface Science* 591 (2021) 106-114.

2. M. Liao, **H. Liu**, X. Wang, X. Hu, Y. Huang, X. Liu, K. Brenan, J. Mecha, M. Nirmalan, J.R. Lu, A Technical Review of Face Mask Wearing in Preventing Respiratory Covid-19 Transmission, *Current Opinion in Colloid & Interface Science* (2021) 101417.

3. X. Hu, H. Gong, P. Hollowell, M. Liao, Z. Li, S. Ruane, **H. Liu**, E. Pambou, N. Mahmoudi, R.M. Dalgliesh, J.R. Lu, What Happens When Pesticides Are Solubilised in Binary Ionic/Zwitterionic-Nonionic Mixed Micelles?, *Journal of Colloid and Interface Science* 586 (2021) 190-199.

4. X. Hu, E. Pambou, H. Gong, M. Liao, P. Hollowell, **H. Liu**, W. Wang, C. Bawn, J. Cooper, M. Campana, K. Ma, P. Li, J.R.P. Webster, F. Padia, G. Bell, J.R. Lu, How Does Substrate Hydrophobicity Affect the Morphological Features of Reconstituted Wax Films and Their Interactions with Nonionic Surfactant and Pesticide?, *Journal of Colloid and Interface Science* 575 (2020) 245-253.

5. X. Hu, H. Gong, Z. Li, S. Ruane, **H. Liu**, P. Hollowell, E. Pambou, C. Bawn, S. King, S. Rogers, How Does Solubilisation of Plant Waxes into Nonionic Surfactant Micelles Affect Pesticide Release?, *Journal of Colloid and Interface Science* 556 (2019) 650-657.

6. X. Hu, H. Gong, Z. Li, S. Ruane, **H. Liu**, E. Pambou, C. Bawn, S. King, K. Ma, P. Li, What Happens When Pesticides Are Solubilized in Nonionic Surfactant Micelles, *Journal of Colloid and Interface Science* 541 (2019) 175-182.

7. H. Gong, J. Zhang, X. Hu, Z. Li, K. Fa, **H. Liu**, T.A. Waigh, A. McBain, J.R. Lu, Hydrophobic Control of the Bioactivity and Cytotoxicity of De Novo-Designed Antimicrobial Peptides, *ACS Appl Mater Interfaces* 11(38) (2019) 34609-34620.

Conferences

"ILL and ESS European Users Meeting 2018", held by ILL and ESS, France, Oct 2018.

"Deuteration for Neutron Science Meeting 2019", held by ISIS, STFC, UK, May 2019 (Poster: Solution aggregation of acyl-L-carnitines studied by small angle neutron scattering).

"10th International Colloid Conference 2020", held by ELSEVIER, Online, Dec 2020

Chapter 1 Introduction

Contents

1.1 Scientific background and motivation

Surfactants are surface-active compounds that can decrease the surface tension or interfacial tension. Surfactants have been widely used in our daily life, such as soaps, detergents, lubricants. Due to their varied functions, several problems have attracted attention, like their toxicity during contact with human skin and the environmental risk from wastewater with relatively high concentrations. Therefore, humans focus on searching and designing new types of surfactants to ameliorate their behaviors in varied applications. However, before their practical applications, experimental studies on the physicochemical properties of these surfactants are helpful to explore their potential abilities in different conditions.

L-carnitine, synthesized in the kidney and liver, is important in some physiological processes (e.g., energy generation) and related to some diseases (e.g., diabetes, metabolic disorders, and chronic hemodialysis) [1-3]. Alky/acyl carnitine derivatives have an effective antimicrobial ability and some of them show good biocompatibility [4, 5]. Long-chain acyl carnitines play essential roles in the transport of fatty acids into mitochondria to provide energy for other body cells [6]. These derivatives are amphiphilic and behave like surfactants as they consist of hydrophobic chains and hydrophilic carnitine groups. However, the lack of experimental studies on the physicochemical properties of acyl carnitines limits their potential applications.
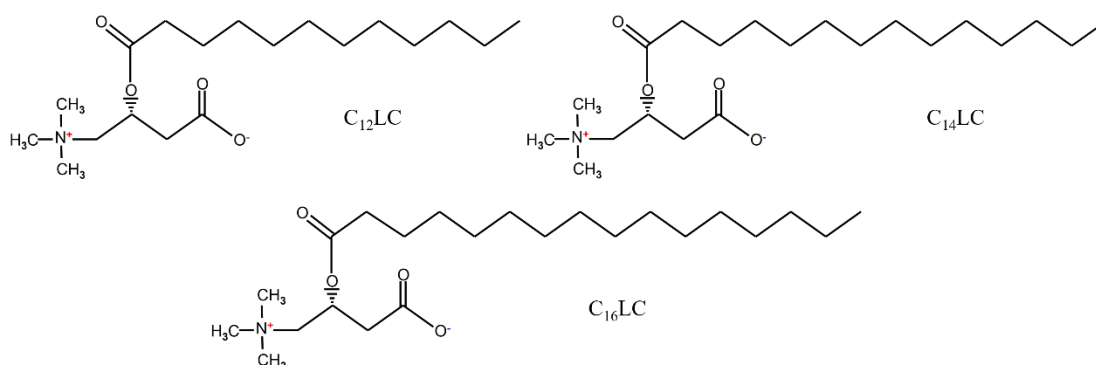
Figure 1.1. Chemical structures of acyl-L-carnitines (C_nLC, n = 12, 14 and 16). The trimethyl ammonium group bears a positive charge and the carboxyl group carries a negative charge at pH 7 leading to zwitterionic form. The carboxyl group is protonated in acidic environment leading to cationic form.

A novel series of acyl-L-carnitines (C_nLC) with the structures shown in **Figure 1.1** has been synthesized by Lonza [7]. Though the acyl-L-carnitines are essential in the transport of long fatty acids and potentially valuable for biological applications, their basic physicochemical properties like solubility, solution aggregation, and interfacial adsorption are still unexplored. Experimental studies on their physicochemical properties will not only provide us a better understanding of this series of biosurfactants but also provide constructive suggestions for their potential applications and further structural design.

This thesis project describes the synthesis and purification methods for C_nLC (protonated and deuterated) and the purity of the samples has been examined by surface tension measurements. The solubilities of C_nLCs in water under different temperatures and pH have been examined by detecting the appearance and disappearance of the insoluble substance from dynamic light scattering (DLS). DLS was also used to investigate the hydrodynamic radii of C_nLC aggregation and then their structures were determined by small-angle neutron scattering (SANS). The interfacial adsorption was mainly studied at air/water and SiO_2/water interfaces. In the work of adsorption at the air/water interface, surface tension measurements were used to determine their critical micelle concentrations (CMCs) and surface excess changes when combined with the Gibbs equation. The structure of the adsorbed layer was studied via neutron reflection (NR). In the work of adsorption at the SiO_2/water interface, the dynamic process and adsorbed amount were monitored by spectroscopic ellipsometry (SE) and further structural information was investigated by NR. Thus, this thesis work has introduced a novel biosurfactant, acyl-L-carnitine, and examined their solution aggregation and interfacial adsorption by using SANS and NR.

1.2 Surfactants

1.2.1 Definition and classification

Surfactants are amphiphilic compounds as they typically consist of a hydrophobic tail group and a hydrophilic head group. The tail usually is an oil-soluble hydrocarbon chain with different lengths and its structure can be linear, branched, or unsaturated. The head group has several types with different charges or hydrophilicity and it commonly determines the type of

surfactant. Thus, the amphiphilic property of surfactants is determined by their hydrophobic and hydrophilic groups leading to different behavior in solution aggregation and interfacial adsorption.
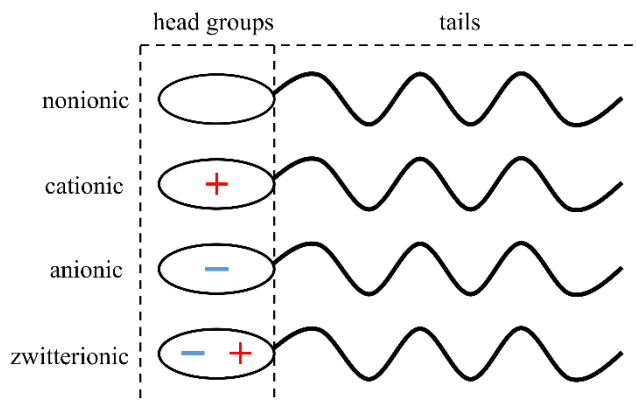
Figure 1.2. General classification of surfactants according to the net charge of their head groups.

The main structural feature of surfactants is schematically shown in **Figure 1.2**. The head of nonionic surfactants has no charge and is often an ethoxylate group. Alkyl ethoxylates are widely used in detergency and as emulsifiers. Ionic surfactants include cationic and anionic ones, such as quaternary ammonium and sulfate, respectively. Cationic surfactants are usually used in fabric and hair conditioners as they have a strong attraction to negatively charged fibers. Anionic surfactants are used in soaps and shampoos. Zwitterionic surfactants carry both a positive and a negative charge, leading to net zero charge, like betaine and sulfobetaine with an alkyl chain. Some of them show attractive biocompatibility, so they are widely added into high end skincare and wound care products [8].

1.2.2 Solution aggregation

Surfactant molecules tend to adsorb at interfaces, e.g. air/water and oil/water interfaces, to remove their hydrophobic tails from the aqueous environment. As concentration increases, surfactant molecules tend to increase their interfacial adsorption, but at a certain concentration point interfacial adsorbed is saturated and a further increase in surfactant concentration contributes to the formation of micelles in the bulk solution. These micelles

form a hydrated shell consisting of hydrophilic head groups and the cores are comprised of hydrophobic tails as shown in **Figure 1.3**. The concentration at which the micelles firstly occur is known as critical micelle concentration (CMC). The CMC can be measured by several techniques, such as surface tension, conductivity, dynamic light scattering, and so on. The CMC can be determined by the critical point where these properties have significant changes as the concentration increases. CMC values are influenced by not only the structure of the surfactant, such as the charge of head and chain length but also environmental conditions, like temperature, ionic strength, and pH.
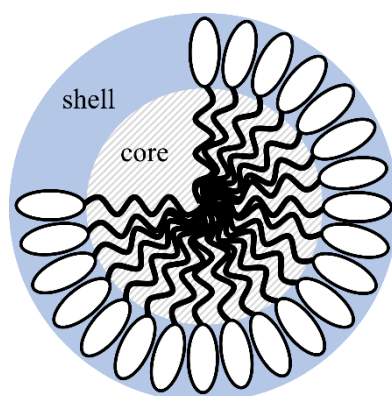
Figure 1.3. The schematic depiction of a core-shell spherical micelle. The hydrophobic tails for the core are protected by a hydrated shell from aqueous environment.

The shape of micelles is diverse, ranging from sphere, ellipsoid, cylinder, vesicle to multi-layered lamellae. The micellar shape differs due to varied structures of surfactant molecules and some of the shape changes are related to other parameters such as concentration, temperature, ionic strength. These various structures of micelles have led to their different applications in detergency, drug delivery, and antimicrobial actions under different environmental conditions.

1.2.3 Adsorption at the air/liquid interface

As indicated already, surfactant molecules tend to adsorb at the air/water interface with the hydrophobic tails in the air and hydrophilic head groups in water. The adsorption of surfactant molecules leads to lower surface tension than pure water as shown in **Figure 1.4(a)**.

In the low concentration region below CMC, most surfactant molecules accumulate at the air/water interface and the surface tension of the solution decreases with the concentration. The interfacial adsorption reaches saturation at CMC. At and above CMC, surfactant molecules start to form micelles in the bulk solution. As the monomer concentration is fixed, surface tension and surface adsorbed amount remain almost constant above CMC as shown in **Figure 1.4(a)(b)**.
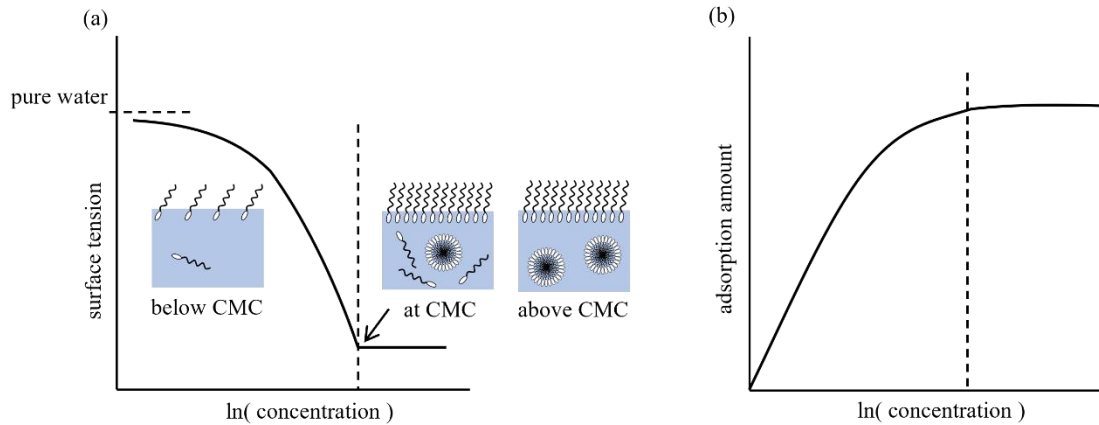
Figure 1.4. (a) A typical plot of surface tension against concentration. The adsorption of surfactants at the air/water interface is depicted by inset figures. (b) The plot of the adsorbed amount against concentration. The vertical dashed line indicates the CMC.

Surface tension measurements are usually used to calculate the adsorbed amount and area per molecule by combining with the Gibbs equation as shown below

$$-d\gamma = \sum_i \Gamma_i d\mu_i \qquad (1.1)$$

where γ is the surface tension, Γ_i and μ_i represent the surface excess and chemical potential for component i in an aqueous solution. μ_i can be expressed by the following equation

$$d\mu_i = RT \cdot d\ln a_i \qquad (1.2)$$

where R is the gas constant, T is the temperature and a_i is the activity of component i which is approximated to its concentration c_i when the surfactant concentration is low. In an aqueous

system with one ionic surfactant, each surfactant ion has a counterion and equation (1.1) and (1.2) then become

$$\frac{d\gamma}{RT} = \Gamma_s dlnc_s + \Gamma_c dlnc_c. \tag{1.3}$$

In this project, the ionic strength is fixed and in excess, so $dlnc_c = 0$ the equation is reduced to

$$\Gamma_s = -\frac{1}{RT}\left(\frac{d\gamma}{dlnc_s}\right). \tag{1.4}$$

The area per surfactant molecule can be calculated from

$$A_s = \frac{1}{\Gamma_s N_a} \tag{1.5}$$

where N_a is the Avogadro number.

1.2.4 Adsorption at the solid/liquid interface

In an aqueous system in contact with a solid substrate, surfactant also has a tendency to adsorb at the solid/liquid interface. Its adsorption kinetics and equilibrium adsorption behavior are related to the nature of the surfactant and the solid surface. The adsorption of surfactant at the solid/liquid interface is important to several areas, such as, corrosion inhibition [9, 10], detergency [11], and mineral flotation [12, 13]. Thus, the property of interfacial adsorption is useful to assess the behavior of a new surfactant.

SiO_2 surfaces are widely used to characterise the adsorption features of surfactants, as the properties of SiO_2 surfaces are well known. In this project, the adsorption behavior of C_nLC has been investigated at the SiO_2/water interface under different conditions. Spectroscopic ellipsometry is used to study the dynamic and equilibrium adsorbed amount of C_nLC. Neutron reflection is well established for investigating the structure of the adsorbed layer [14, 15], as it is highly sensitive to different parts of the adsorbed interfacial layer when deuterated surfactant samples are used.

1.3 Novel acyl-L-carnitine surfactants

1.3.1 Carnitine

Carnitine has a chiral molecular structure, including L-carnitine and D-carnitine. The D-form is toxic [16, 17], whereas the L-form is predominantly present in mammalian bodies [18, 19]. L-carnitines contribute to the transport of long-chain fatty acids into mitochondria, which is essential for the oxidation of fats and energy generation [20]. Although L-carnitines can be naturally synthesized in our kidneys and livers, some people with medical conditions cannot make enough [1]. The lack of L-carnitine in our bodies is related to excess weight which has been a substantial concern for decades [21]. Obesity can lead to many other health problems, such as type II diabetes, fatty liver, and cardiovascular diseases [22]. As a result, L-carnitines are commonly added into nutritional supplements.

1.3.2 Acyl-L-carnitine

Acyl-L-carnitines and their derivatives can be formed during the transport of fatty acids, and they have also been reported as antimicrobial compounds against bacteria, fungi, and yeasts [4]. Besides, their derivatives show good biocompatibility and have potential use in gene delivery [5, 23]. As the acyl chain is hydrophobic and L-carnitine is hydrophilic, acyl-L-carnitines behave like a typical surfactant. There have been a number of studies exploiting their biological applications, but experimental studies to investigate their physicochemical properties remain lacking. This situation limits their potential use as new biosurfactants. This project has studied their solubility, solution aggregation, and interfacial adsorption to unravel their properties. These basic studies will provide a useful basis to develop their technological applications.

This project studied three acyl-L-carnitines, including Lauroyl-L-carnitine ($C_{12}LC$), Myristoyl-L-carnitine ($C_{14}LC$), and Palmitoyl-L-carnitine ($C_{16}LC$). They were synthesized separately following a method developed at Lonza [7]. The chain deuterated samples of these three acyl-L-carnitines were synthesized by the following method. TLC was firstly used to monitor the reaction of deuterated saturated fatty acid and excess thionyl chloride. The

deuterated n-acyl chloride was produced by this process. Then, the mixture of L-carnitine hydrochloride salt and trichloroacetic acid was heated to 70 °C and kept at this temperature until it is melted. Then the mixture was cooled down to 50 °C and deuterated n-acyl chloride was added dropwise into the mixture. The solution was reheated to 70 °C with stirring. After 16 hr, 1-propanol was added into the cooled solution to precipitate the crude product and the product was filtered. Finally, the chain deuterated acyl-L-carnitine hydrochloride salt was recrystallized from acetone.

Protonated and chain deuterated C_nLC was purified by a same method. C_nLC samples were dissolved in water and the solution was titrated with NaOH solution to pH 7 at 45 °C. Then the water was removed by freeze-drying to give intermediate white powder. The powder was dissolved in excess absolute ethanol and the cloudy solution was filtered to remove NaCl. The residual ethanol was removed by a rotary evaporator to give crude product. Finally, C_nLC samples were purified by three recrystallizations.

1.3.3 Current studies of L-carnitine and acyl-L-carnitine

L-carnitine contributes to lipid metabolism and plays an essential role in mitochondrial β-oxidation of long-chain fatty acids for cellular energy generation [24, 25]. L-carnitine was identified as an essential multifunctional nutrient for the human body [26] and has been used in nutrition supplements to treat L-carnitine deficiency [27]. Moreover, carnitine protects DNA and cell membrane from the damage caused by free oxygen radicals and also prevents protein oxidation and lactate oxidative damage [26, 28]. There are also studies indicating that the initiation of sperm motility is related to an increase of L-carnitine and L-acetyl-carnitine which is important for sperm metabolism [29-31]. Thus, many clinical trials attempted to prove the positive therapeutic effects of L-carnitine on infertile men with various forms of sperm dysfunction. Besides, carnitine has been approved by Food and Drug Administration (FDA) to use in medication in order to treat carnitine nutritional deficiency [26]. In addition to its vital role in energy production, L-carnitine also contributes to the pathogen-free

environment, especially in male genital tracts [32, 33] and shows an attractive antimicrobial effect against bacteria and yeasts [34].

Acyl-L-carnitine derivatives are formed during fat metabolic processes and also play other physiological roles [35]. The extramitochondrial ratio of acyl-L-carnitine to L-carnitine can be used to monitor the intramitochondrial relationship between CoA (co-enzyme A) and acyl-CoA [36] which is a critical indicator for the identification of mitochondrial dysfunction in clinical cases [18]. Acyl-L-carnitines with short chains also show a relationship with insulin resistance [37], but those with long chains could cause harmful effects on human red blood cells which is possibly related to its membrane-lytic activity [38]. In addition, acyl-L-carnitine and its esters are amphiphilic compounds and show good activity against a wide range of bacteria, yeasts and fungi, as broad-spectrum antimicrobials [4]. Moreover, acyl-L-carnitines show attractive biocompatibility [5] and are potential in gene delivery [23]. Though the research about their biological properties has been pursued extensively, it is urgent to apply our knowledge in physical chemistry to help understand their physiochemical properties. There are a few key issues requiring furthermore experimental studies:

(1) How do acyl-L-carnitine molecules aggregate in the bulk solution under different stimuli and what is the structure of their aggregates?

(2) How do acyl-L-carnitine molecules adsorb at the air/water and SiO_2/water interfaces and what is the structure of the adsorbed layer?

(3) How do the acyl-L-carnitines interact with membranes of different cell types including human cells, bacteria, and fungi?

This thesis work aims to address some of the technical issues underlined by the first two challenges and bridge our current understanding of the physicochemical properties of acyl-L-carnitine from the colloid science side with potential biological or clinical applications.

1.4 Outline of the thesis plan

The broad aim of this project is to investigate the physicochemical properties of C_nLCs under different conditions using neutron scattering, neutron reflection and other complementary techniques. This thesis is submitted in the journal format to provide a better illustration of the main results. Chapters 1 describes the introduction to the project background, broad literature work underlining this thesis work, and motivation. Chapter 2 introduces the main experimental methodology, underlying theories, and data analysis approaches. Chapters 3, 4, and 5 are the manuscripts prepared in the format of publications that have either been published, just submitted or in the process of being submitted. The main conclusion of the thesis work and future work are presented in Chapter 6. Further details concerning each chapter are provided below.

Chapter 1 introduces the scientific background of this project. It then introduces the basic properties of surfactants and the current literature studies about carnitines and acyl-L-carnitines.

Chapter 2 provides a simple introduction to the main techniques applied in this project, including dynamic light scattering (DLS), small angel neutron scattering (SANS) and neutron reflection (NR) covering basic technical descriptions of the techniques, underlying theories and data analysis approaches.

Chapter 3 discusses the surface adsorption and solution aggregation of the new biosurfactant, lauroyl-L-carnitine ($C_{12}LC$). This work examines the surface tension, CMC, micellar structure and adsorption of $C_{12}LC$ at the air/water interface. This work was published in the Journal of Colloid and Interface Science in February 2021.

Chapter 4 reports the effect of acyl chain length on the physicochemical properties of acyl-L-carnitines (C_nLCs). The results manifested the effect of molecular structure and provided constructive suggestions on its further design. This work is in the process of being submitted to the Journal of Colloid and Interface Science.

Chapter 5 reports the adsorption behavior of C_nLCs at the SiO_2/water interface, including adsorption kinetics, adsorption isotherm and structure of the adsorbed layer. This work will be submitted to the Journal of Colloid and Interface Science as well.

Chapter 6 provides an overall conclusion for this project and also offers some suggestions for future work.

The candidate is the first author for the three papers in **Chapters 3-5**. He has contributed to the design and delivery of experimental studies, data analysis and interpretation.

Reference

[1] P.B. Celestino-Soper, S. Violante, E.L. Crawford, R. Luo, A.C. Lionel, E. Delaby, G. Cai, B. Sadikovic, K. Lee, C. Lo, A Common X-Linked Inborn Error of Carnitine Biosynthesis May Be a Risk Factor for Nondysmorphic Autism, Proceedings of the National Academy of Sciences 109(21) (2012) 7974-7981.

[2] J.L. Flanagan, P.A. Simmons, J. Vehige, M.D. Willcox, Q. Garrett, Role of Carnitine in Disease, Nutrition & metabolism 7(1) (2010) 1-14.

[3] S. Ahmad, L-Carnitine in Dialysis Patients, Seminars in Dialysis, Wiley Online Library, 2001, pp. 209-217.

[4] M. Calvani, L. Critelli, G. Gallo, F. Giorgi, G. Gramiccioli, M. Santaniello, N. Scafetta, M.O. Tinti, F. De Angelis, L-Carnitine Esters as "Soft", Broad-Spectrum Antimicrobial Amphiphiles, Journal of Medicinal Chemistry 41(13) (1998) 2227-2233.

[5] J. Nivet, M. Le Blanc, J. Riess, Synthesis and Preliminary Evaluation of Perfluoroalkylacyl Carnitines as Surfactants for Biomedical Use, European Journal of Medicinal Chemistry 26(9) (1991) 953-960.

[6] T.N. Tarasenko, K. Cusmano-Ozog, P.J. McGuire, Tissue Acylcarnitine Status in a Mouse Model of Mitochondrial B-Oxidation Deficiency During Metabolic Decompensation Due to Influenza Virus Infection, Molecular Genetics and Metabolism 125(1-2) (2018) 144-152.

[7] D.L.M. Smida, TN), Process for the Production of a Fatty Acid/Carnitine Derivative, Lonza Ltd. (Visp, CH), United States, 2013.

[8] J.H. Clint, Surfactant Aggregation, Springer Science & Business Media2012.

[9] G. Mu, T. Zhao, M. Liu, T. Gu, Effect of Metallic Cations on Corrosion Inhibition of an Anionic Surfactant for Mild Steel, Corrosion 52(11) (1996) 853-856.

[10] M.L. Free, Understanding the Effect of Surfactant Aggregation on Corrosion Inhibition of Mild Steel in Acidic Medium, Corrosion Science 44(12) (2002) 2865-2870.

[11] Y. Yangxin, Z. Jin, A.E. Bayly, Development of Surfactants and Builders in Detergent Formulations, Chinese Journal of Chemical Engineering 16(4) (2008) 517-527.

[12] Y.-S. Cho, J. Laskowski, Effect of Flotation Frothers on Bubble Size and Foam Stability, International Journal of Mineral Processing 64(2-3) (2002) 69-80.

[13] H. Sis, S. Chander, Improving Froth Characteristics and Flotation Recovery of Phosphate Ores with Nonionic Surfactants, Minerals engineering 16(7) (2003) 587-595.

[14] X. Hu, E. Pambou, H. Gong, M. Liao, P. Hollowell, H. Liu, W. Wang, C. Bawn, J. Cooper, M. Campana, K. Ma, P. Li, J.R.P. Webster, F. Padia, G. Bell, J.R. Lu, How Does Substrate Hydrophobicity Affect the Morphological Features of Reconstituted Wax Films and Their Interactions with Nonionic Surfactant and Pesticide?, Journal of Colloid and Interface Science 575 (2020) 245-253.

[15] G. Fragneto, R.K. Thomas, A.R. Rennie, J. Penfold, Neutron Reflection from Hexadecyltrimethylammonium Bromide Adsorbed on Smooth and Rough Silicon Surfaces, Langmuir 12(25) (1996) 6036-6043.

[16] C.J. Gross, L.M. Henderson, Absorption of D-and L-Carnitine by the Intestine and Kidney Tubule in the Rat, Biochimica et Biophysica Acta (BBA)-Biomembranes 772(2) (1984) 209-219.

[17] I. Tamai, R. Ohashi, J.-i. Nezu, H. Yabuuchi, A. Oku, M. Shimane, Y. Sai, A. Tsuji, Molecular and Functional Identification of Sodium Ion-Dependent, High Affinity Human Carnitine Transporter Octn2, Journal of Biological Chemistry 273(32) (1998) 20378-20382.

[18] S.E. Reuter, A.M. Evans, Carnitine and Acylcarnitines, Clinical Pharmacokinetics 51(9) (2012) 553-572.

[19] J. Harmeyer, The Physiological Role of L-Carnitine, Lohman Information 27 (2002) 15-21.

[20] F.M. Vaz, R.J. Wanders, Carnitine Biosynthesis in Mammals, Biochemical Journal 361(3) (2002) 417-429.

[21] M. Fried, V. Hainer, A. Basdevant, H. Buchwald, M. Deitel, N. Finer, J.W. Greve, F. Horber, E. Mathus-Vliegen, N. Scopinaro, Interdisciplinary European Guidelines on Surgery of Severe Obesity, Obesity Facts 1(1) (2008) 52-59.

[22] M. Pooyandjoo, M. Nouhi, S. Shab-Bidar, K. Djafarian, A. Olyaeemanesh, The Effect of (L-) Carnitine on Weight Loss in Adults: A Systematic Review and Meta-Analysis of Randomized Controlled Trials, Obesity Reviews 17(10) (2016) 970-976.

[23] J. Wang, X. Guo, Y. Xu, L. Barron, F.C. Szoka, Synthesis and Characterization of Long Chain Alkyl Acyl Carnitine Esters. Potentially Biodegradable Cationic Lipids for Use in Gene Delivery, Journal of Medicinal Chemistry 41(13) (1998) 2207-2215.

[24] J. Bremer, Carnitine--Metabolism and Functions, Physiological Reviews 63(4) (1983) 1420-1480.

[25] J. Kerner, C. Hoppel, Genetic Disorders of Carnitine Metabolism and Their Nutritional Management, Annual Review of Nutrition 18(1) (1998) 179-206.

[26] X. Zhou, F. Liu, S. Zhai, Effect of L-Carnitine and/or L-Acetyl-Carnitine in Nutrition Treatment for Male Infertility: A Systematic Review, Asia Pacific Journal of Clinical Nutrition 16 (2007) 383.

[27] A.G. Engel, C. Rebouche, Carnitine Metabolism and Inborn Errors, Journal of Inherited Metabolic Disease 7(1) (1984) 38-43.

[28] A. Arduini, Carnitine and Its Acyl Esters as Secondary Antioxidants?, American Heart Journal 123(6) (1992) 1726-1727.

[29] L. Johansen, T. Bøhmer, Carnitine-Binding Related Supressed Oxygen Uptake by Spermatozoa, Archives of Andrology 1(4) (1978) 321-324.

[30] C. Jeulin, L.M. Lewin, Role of Free L-Carnitine and Acetyl-L-Carnitine in Post-Gonadal Maturation of Mammalian Spermatozoa, Human Reproduction Update 2(2) (1996) 87-102.

[31] C. Radigue, S. Es-Slami, J. Soufir, Relationship of Carnitine Transport across the Epididymis to Blood Carnitine and Androgens in Rats, Archives of Andrology 37(1) (1996) 27-31.

[32] E. Vicari, A. Calogero, Effects of Treatment with Carnitines in Infertile Patients with Prostato-Vesiculo-Epididymitis, Human Reproduction 16(11) (2001) 2338-2342.

[33] E. Vicari, C. Rubino, A. De Palma, G. Longo, M. Lauretta, S. Consoli, A. Arancio, Antioxidant Therapeutic Efficiency after the Use of Carnitine in Infertile Patients with Bacterial or Non Bacterial Prostato-Vesiculo-Epididymitis, Archivio Italiano di Urologia, Andrologia: Organo Ufficiale [di] Societa Italiana di Ecografia Urologica e Nefrologica 73(1) (2001) 15-25.

[34] A. Olgun, O. Kisa, S. Yildiran, S. Tezcan, S. Akman, M. Erbil, Antimicrobial Efficacy of L-Carnitine, Annals of Microbiology 54(1) (2004) 95-102.

[35] H. Liu, X. Hu, Z. Li, K. Fa, H. Gong, K. Ma, M. Liao, P. Li, J.R. Webster, J.T. Petkov, R.K. Thomas, J.R. Lu, Surface Adsorption and Solution Aggregation of a Novel Lauroyl-L-Carnitine Surfactant, Journal of Colloid and Interface Science 591 (2021) 106-114.

[36] R. Pons, D.C. De Vivo, Primary and Secondary Carnitine Deficiency Syndromes, Journal of Child Neurology 10(2_suppl) (1995) 2S8-2S24.

[37] M.G. Schooneman, F.M. Vaz, S.M. Houten, M.R. Soeters, Acylcarnitines: Reflecting or Inflicting Insulin Resistance?, Diabetes 62(1) (2013) 1-8.

[38] A. Kobayashi, H. Watanabe, S. Fujisawa, T. Yamamoto, N. Yamazaki, Effects of L-Carnitine and Palmitoylcarnitine on Membrane Fluidity of Human Erythrocytes, Biochimica et Biophysica Acta (BBA) - Biomembranes 986(1) (1989) 83-88.

Chapter 2 Dynamic light scattering (DLS), small angle neutron scattering (SANS), and neutron reflection (NR)

This chapter introduces the main techniques used in this project and provides a brief discussion about neutron experimental setup and data analysis. Other experimental techniques including synthesis and purification of the surfactants, surface tension measurements, spectroscopic ellipsometry (SE) also play important roles in this project but they have been fully described in the three papers in **Chapter 3-5**.

Contents

2.1 DLS

2.1.1 Introduction for DLS

DLS is a powerful technique to measure the size of particles typically in the sub-micron region. DLS uses a monochromatic, coherent light source (laser) to illuminate the particles and records the signal of scattered light. The laser beam used in DLS has a signal wavelength (e.g., the wavelength of the laser in Zetasizer Nano-ZS is 633 nm) and low divergence relative to other light sources. In a DLS instrument, the laser light scatters when the laser light encounters particles in solution and scattering intensity is recorded by a detector. Because of the continuous motion of particles in solution, the incident laser light will undergo a phenomenon called Doppler broadening [1, 2]. The scattered light will lead to constructive phases to give a signal or destructive phases and cancel each other out. DLS measures the Brownian motion of the particles caused by bombardment by the solvent molecules. Thus, the larger particles have slower speeds and the smaller particles move more rapidly. The sizes of the particles could be calculated by the following equation [3]:

$$d = \frac{kT}{3\pi\eta D}$$
(2.1)

where d is the hydrodynamic diameter, k is Boltzmann's constant, T is absolute temperature, η is the viscosity in $N \cdot s/m^2$ and D is translational diffusion coefficient which is related to the hydrodynamic size of particles. The diameter measured by DLS is the hydrodynamic diameter which refers to how a hypothetical spherical particle diffuses within a fluid.

2.1.2 Size information from correlograms

The DLS instrument detects the intensity of the scattered light which fluctuates as a function of time. Then the digital autocorrelator correlates intensity fluctuations of scattered light against time to show how fast the intensity fluctuates which is related to the diffusion behavior of particles [2]. The correlograms as shown in **Figure 2.1** are

used to describe the degree of similarity between the intensity signal with itself at varying time intervals. The correlation reduces with time. The signal of large spherical particles (hydrodynamic radius is around 200 nm) changes slowly due to the low velocity and the correlation will persist for a longer time as shown in **Figure 2.1(a)**. In contrast, small spherical particles (hydrodynamic radius is around 2 nm) move rapidly leading to a sharp decrease in correlation as shown in **Figure 2.1(b)**. Thus, the time where the correlation starts to decay could be used to estimate the mean size of the particles. The line is steeper means that the sample is more monodisperse. Conversely, the decay becomes more extended, the sample is more polydisperse [3]. Thus, the correlograms in **Figure 2.1** are monodisperse.
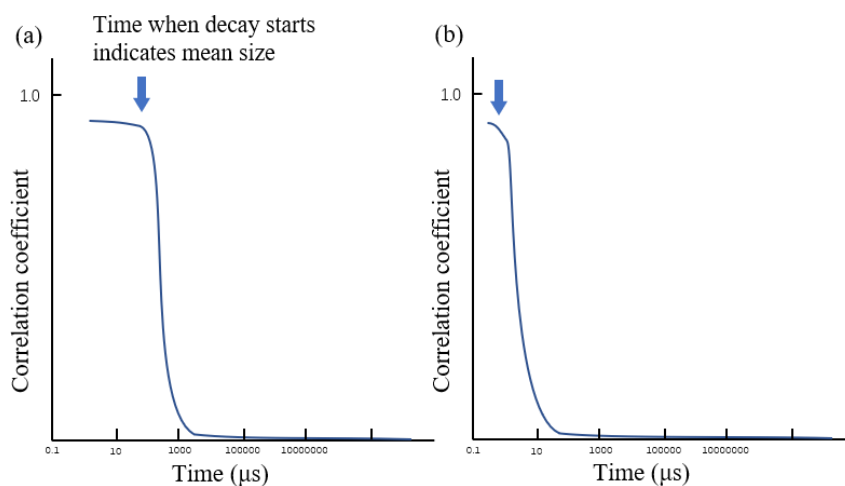
Figure 2.1. Typical correlograms of a sample containing large spherical particles (a) or small spherical particles (b). The correlation coefficient with respect to time is calculated by a digital autocorrelator. The time when the correlation coefficient starts to decay can be used to estimate the mean size of particles.

2.2 SANS

2.2.1 Introduction for SANS

SANS has been widely used as a powerful technique for detecting nanostructures in various areas, such as physics, chemistry, and materials. Because it is non-destructive

to the materials, SANS is highly popular for studying nanostructures in soft matter and biophysics. SANS can provide information about the size and shape of the aggregates of surfactants under different conditions. This explains why it will be used as a main technique for unraveling micellar structures of acyl-L-carnitines.

2.2.1.1 Neutron beam sources and SANS instruments

The neutron experiments in this project were undertaken in ISIS Neutron and Muon Facility (Didcot, UK) and Institute Laue Langevin (ILL, Grenoble, France). ISIS produces neutron beams from a spallation source. High-speed protons are accelerated by the synchrotron and then collide with a tungsten target so that the neutrons are produced from the collisions and form the neutron pulses. Before being used by different instruments, these neutrons are slowed down to the appropriate speeds by the hydrogenous moderator [4]. In the ILL, the neutron beams are produced from a reactor source by the controlled chain reactions [5]. Thus, the neutron beams in ILL usually involve higher flux and energy in comparison with ISIS.

The SANS measurements were performed on the instrument LOQ in ISIS Neutron and Muon Facility and D11 in Institute Laue Langevin. LOQ is a time-of-flight instrument with a λ range of 2.2 – 10 Å leading to a Q range from 0.01 to 0.34 Å^{-1} [6]. D11 used the neutron beam with a fixed wavelength of 5.5 Å. The distance between the sample and detector can be set at 1.4 and 8 m to give a Q range of 0.01 – 0.5 Å^{-1} [7].

2.2.1.2 Scattering vector

Figure 2.2 describes the scattering of a neutron deflected by a sample particle. The incident neutron has an initial wavenumber, $\mathbf{k_i}$, and a final wavenumber $\mathbf{k_f}$ after the scattering happens. Due to the elastic scattering, $|\mathbf{k_i}|=|\mathbf{k_f}|=2\pi/\lambda$. The scattering vector or momentum transfer, $\mathbf{Q}$, can be expressed by $\mathbf{Q = k_f - k_i}$, and its magnitude is calculated by the following equation

$$Q = \left| k_f - k_i \right| = \frac{4\pi sin\theta}{\lambda} \tag{2.2}$$

where λ is the wavelength and 2θ is the scattering angle. When θ is small, equation (2.2) could be transferred into

$$Q \approx \frac{4\pi}{\lambda} \frac{r_d}{L_{sd}} \tag{2.3}$$

where r_d is the radial distance and L_{sd} is the distance from the sample to the detector. Combing equation (2.3) with the Bragg law of diffraction $\lambda=2dsin\theta$, the equation can be simplified into the following expression

$$d = \frac{2\pi}{Q} \tag{2.4}$$

where d is the molecular-level length scale denoting the dimension of the scattering object such as the diameter of the scattering particle or the thickness of the lipid bilayer. Equation (2.4) can be used to estimate the size of the scattering object or determine the Q range used in the SANS measurements.
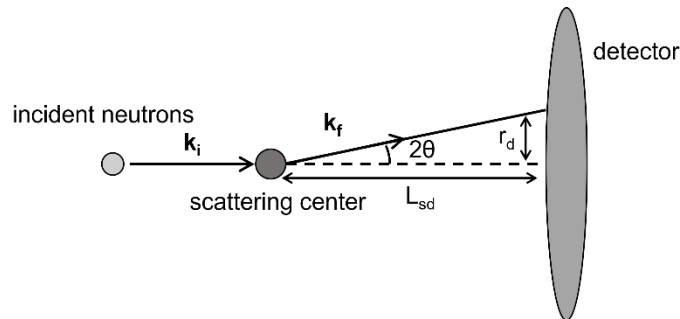
Figure 2.2. The ideal neutron scattering event in a SANS experiment. k_i is the initial wavenumber of the incident neutron and k_f is the final wavenumber of the scattered neutron. 2θ is the scattering angle. r_d is the radial distance and L_{sd} is the distance from the sample to the detector.

2.2.1.3 Scattering length density (SLD) and contrast

Nuclei have different levels of repulsive or attractive strength to neutrons which is described by neutron scattering length or scattering amplitude, b. The scattering

length density (SLD), ρ, of a molecule is used to model the nuclear interaction cross section of a sample which can be expressed by the following equation

$$\rho = \frac{\sum_i b_i}{V} \tag{2.5}$$

where b_i is the scattering length of nucleus i, V is the molecular volume and the unit of ρ is Å^{-2}. Thus, the isotopic substitution of nuclei can alter the molecular SLD value significantly without any influence on its chemical composition. For example, D_2O ($\rho=6.35\times10^{-6}$ Å^{-2}) is a common solvent in neutron experiments because of its significantly high SLD than H_2O ($\rho=-0.56\times10^{-6}$ Å^{-2}), so that many hydrocarbons samples ($\rho\approx0$ Å^{-2}) could be easily detected from the large SLD difference.
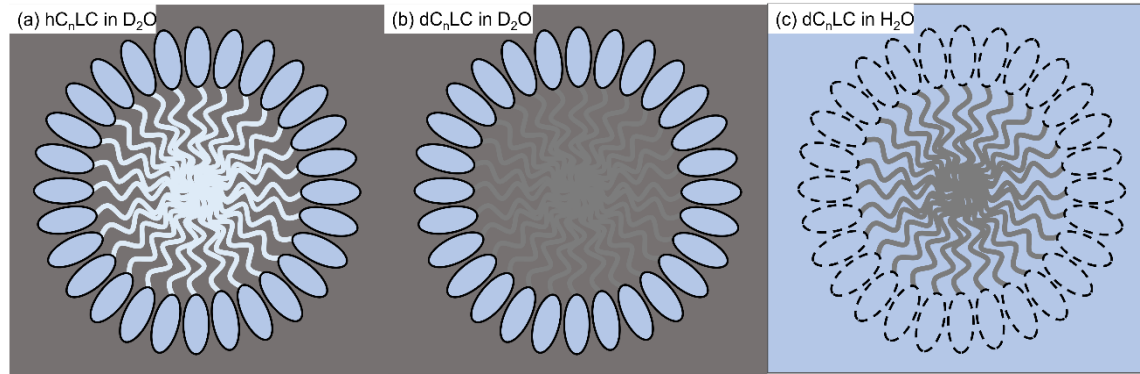
Figure 2.3. Three contrasts in SANS measurements with surfactant micelles including (a) hC_nLC (fully protonated) in D_2O, (b) dC_nLC (deuterated chain) in D_2O and (c) H_2O. Heads and tails show different visibilities in H_2O and D_2O.

The difference of SLDs between the bulk solution and the sample molecules plays an important part in the feasibility of a neutron experiment. Also, we can adjust the SLD of solvent to match with different parts of the samples so that the information about different parts in a self-assembled nanostructure can be obtained from varied contrasts as shown in **Figure 2.3**.

In the work undertaken in this project, SANS data were fitted with a core-shell sphere model involving model parameters of concentration, temperature, background, the radius of core, thickness of shell, SLD of core, SLD of shell, and SLD of solvent. The

radius, thickness, SLDs of core and shell are unknown but the others can be fixed or estimated from known physical parameters. For the acyl-L-carnitine systems, DLS data show that the aggregates are more monodisperse. Three contrasts including hC_nLC (fully protonated) in D_2O, dC_nLC (deuterated chain) in H_2O and D_2O were mostly used to measure their micellar structure from SANS in this project. As shown in **Figure 2.3**, in the contrast of hC_nLC in D_2O, the total radius and shape of micelles are clearer under this run as the difference between the SLD of surfactant molecules and the solvent is large. The contrast of dC_nLC in D_2O is more sensitive to the thickness and SLD of the shell as the SLD of D_2O is close to that of the deuterated tail, while the contrast of dC_nLC in H_2O provides a clear probe of the micellar core. Thus, SANS is a powerful technique to characterize the micellar structures by different isotopic contrasts with the help of protonated and deuterated samples and H_2O and D_2O.

2.2.2 SANS data analysis

The SANS experiments provide the intensity profiles I(Q) which are plotted as a function of Q. Before data analysis, the background is often removed and transmission effects are adjusted. The scattering intensity data of particles can be fitted by the suitable models determined by the structural properties and spatial distribution of the particles. The principal relation between particle structure and scattering intensity can be expressed by the following equation:

$$I(Q) = N_p(\Delta\rho)^2 V_p{}^2 P(Q)S(Q) \tag{2.6}$$

where N_p is the number density, $\Delta\rho$ is the difference of SLD, V_p is the volume of the particles, P(Q) is the form factor and S(Q) is the structure factor.

The term P(Q) describes how I(Q) is influenced by the interference effects between neutrons scattered by different parts of the same particles. Thus, the form factor is sensitive to the size and shape of the scattering particles. The structure factor, S(Q),

describes how I(Q) is modulated by the interference effects between neutrons scattered by different particles. As a result, the term S(Q) is related to the interaction between different particles. Several parameters derived from the form and structure factors can be adjusted to find the best fit. For micellar systems studied in this work, the particulate concentrations are usually low and thus S(Q)=1.

The SANS data profiles in this project were fitted using the analysis software, SasView. Firstly, a model was chosen based on the predicted shape of the particles and the interaction in the system. Then, parameters such as solvent and solute SLDs were fixed as the calculated values from equation (2.5) and the other parameters can be fitted by the software in a certain range to give a minimal chi-squared value, χ^2. Apart from the parameters obtained from the analysis software, associated parameters can also be derived to check the accuracy of the fitting model. For example, the number of head groups should be equal to that of the tails in a surfactant micelle.

2.3 NR

2.3.1 Introduction for NR

Neutron reflection (NR) has many advantages in studying the layer's structure at interfaces, such as high resolution, non-destruction, and can detect the buried interfaces. Besides, because of isotopic substitution, large contrasts in the SLD can be designed to obtain the structural information of different parts. Thus, NR has been used in studying the adsorption behaviors of surfactants, lipids, and proteins at different interfaces [8]. NR can provide a structural description of thin planar films at the air/liquid, solid/liquid and other interfaces including their thickness, composition, and related structural parameters such as roughness.
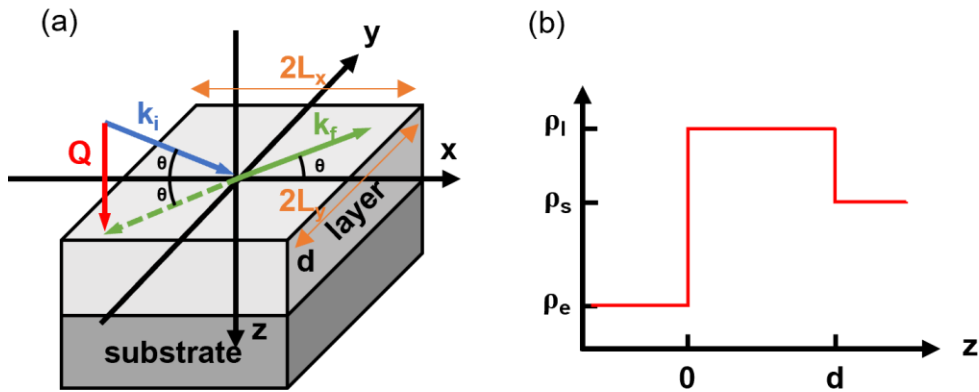
Figure 2.4. (a) A typical schematic representation of neutron beam reflected with the incident angle of θ from a planar interface. (b) A typical SLD profile $\rho(z)$ for a uniform layer where z denotes the distance normal to the interface. The initial wavenumber of incident neutron is k_i and the final wavenumber of reflected neutron is k_f. 2θ is the scattering angle. Q is the momentum transfer and d is the thickness of the layer. ρ_l, ρ_s, and ρ_e are the SLD values of the layer, substrate, and environment. The illuminated area from the neutron beam is constrained by $-L_x<x<L_x$ and $-L_y<y<L_y$.

A neutron beam can be reflected at the interface in an analogous way to the light as shown in **Figure 2.4(a)** which depicts the incident beam of neutrons with the angle of θ reflected on a planner interface. The illuminated area from the neutron beam is constrained by $-L_x<x<L_x$ and $-L_y<y<L_y$. The reflectivity of neutrons is dependent on their wavelength, incident angle, and the composition of the interfacial layers. Neutron reflection is an elastic scattering process i.e. there is no energy transfer during the process. Thus, the momentum transfer (Q) of scattered neutrons could be expressed by equation (2.1). The neutron reflectivity, R(Q), is calculated by the ratio of reflected neutron intensity, $I_r(Q)$, over incident neutron intensity, $I_i(Q)$. The reflectivity measured by neutron reflectometry can be expressed using the perpendicular momentum transfer (Q), SLD of the layer ($\rho(z)$), and the position in z direction as follows

$$R(Q) \approx \frac{(4\pi)^2}{Q^2} \left| \int_{-\infty}^{\infty} \rho(z) e^{izQ} dz \right|^2. \qquad (2.7).$$

After integrating by parts, equation (2.7) becomes [9]:

$$R(Q) \approx \frac{(4\pi)^2}{Q^4} \left| \int_{-\infty}^{\infty} \frac{d\rho(z)}{dz} e^{izQ} dz \right|^2. \qquad (2.8).$$

2.3.2 NR for the uniform layer

Figure 2.4(a) shows a uniform layer with a thickness of d in NR measurements, and the SLD in the uniform layer system is shown in **Figure 2.4(b)** with the following distribution:

$$\rho(z) = \begin{cases} \rho_e & z < 0 \\ \rho_l & 0 < z < d \\ \rho_s & z > d \end{cases} \qquad (2.9)$$

where ρ_e, ρ_l and ρ_s are SLD values of environment, layer, and substrate, respectively. Thus, the derivative of the SLD $(d\rho(z)/dz)$ is

$$\frac{d\rho(z)}{dz} = (\rho_l - \rho_e)\delta(z) + (\rho_s - \rho_l)\delta(z - d). \qquad (2.10).$$

By substitution into equation (2.8), the reflectivity is given by

$$R(Q) \approx \frac{(4\pi)^2}{Q^4} \left[(\rho_l - \rho_e) + (\rho_s - \rho_l) e^{idQ} \right]^2 \qquad (2.11)$$

then the reflectivity is evaluated as

$$R(Q) \approx \frac{(4\pi)^2}{Q^4} \left[(\rho_l - \rho_e)^2 + (\rho_s - \rho_l)^2 + 2(\rho_l - \rho_e)(\rho_s - \rho_l) \cos(Qd) \right] \qquad (2.12).$$

Equation (2.12) indicates that the reflectivity drops off as $1/Q^4$ and has a frequency of the oscillation equal to $2\pi/d$. And the maximum of R(Q) is 1 when the total external reflection occurs.

When the thickness of the uniform layer is zero, the system becomes an ideal interface with the SLD profile as

$$\rho(z) = \begin{cases} \rho_e & z < 0 \\ \rho_s & z > 0 \end{cases}.$$ (2.13).

In this situation, the reflectivity is determined by following

$$R(Q) \approx \frac{(4\pi)^2}{Q^4}(\rho_s - \rho_e)^2.$$ (2.14)

Thus the reflectivity is a function of $1/Q^4$, from a perfectly sharp interface. The actual air/D_2O interface under no external vibration can be approximated to this idealized scenario over the low Q range. However, thermal agitations (the kT effect, where k is Boltzmann constant) disturb the surface via capillary waves lead to an effective contribution of surface roughness, which is often taken into account during instrument calibration at the start of adsorption measurements.

2.3.3 NR for the multilayer film

In the NR analysis process, the NR data is commonly fitted by a multilayer model due to several layers with different SLD values as follows

$$\rho(z) = \begin{cases} \rho_0 & z < 0 \\ \rho_1 & 0 < z < d_1 \\ \rho_2 & d_1 < z < d_1 + d_2 \\ \quad \vdots \\ \rho_n & z > \sum_1^n d_n \end{cases}.$$ (2.15)

Then the derivative of SLD can be expressed as a series of δ-functions as follows

$$\frac{d\rho(z)}{dz} = (\rho_1 - \rho_0)\delta(z) + (\rho_2 - \rho_1)\delta(z - d_1) + \cdots (\rho_n - \rho_{n-1})\delta\left(z - \sum_1^n d_n\right).$$ (2.16)

Thus, the reflectivity can be evaluated by substituting equation (2.16) into (2.8)

2.3.4 NR data analysis

Motofit software based on Igor pro was used to fit the NR data profile in this project. The fitting of NR data profiles is based on the optical matrix method by Motofit and it

provides parameters including the thickness, SLD, and roughness of different layers. Consequently, Motofit provides a profile of SLD against depth to describe the structural information of the layers at the interface. With these parameters, other information of the layer, such as volume fraction, adsorbed amount, area per molecule, can be derived by the following equation

$$\rho_l = \rho_s \alpha_s + \rho_b \alpha_b \tag{2.17}$$

where ρ_l, ρ_s, and ρ_b are the SLD values of the layer, sample, and the bulk solution. α_s and α_b are the volume fractions of sample and bulk solution, with $\alpha_s + \alpha_b = 1$. Thus, equation (2.17) can be converted into the following expression

$$\alpha_s = \frac{\rho_l - \rho_b}{\rho_s - \rho_b}. \tag{2.18}$$

The area per molecule, A, can be calculated from thickness, z, and molecular volume of sample, v_s, from the following equation

$$A = \frac{v_s}{z \alpha_s}. \tag{2.19}$$

Thus, the adsorbed amount, Γ, can be expressed by

$$\Gamma = \frac{1}{A N_a}. \tag{2.20}$$

As described under SANS, parallel NR measurements are often undertaken under two or more different isotopic contrasts for a given system to enhance structural resolution across the interface. For an acyl-L-carnitine adsorbed at the air/water interface at its CMC, these often involve acyl chain deuterated sample in null reflecting water (NRW) and D_2O and hydrogenated sample in D_2O as well. The combined data analyses lead to the determination of the thickness of the acyl chain layer, the thickness of the head layer and its extent of mixing with water and the area per molecule. From these structural parameters, other structural details could be derived.

2.3.5 Experimental methods for NR

The NR measurements were performed on the instrument SURF in ISIS Neutron and Muon Facility and FIGARO in Institute Laue Langevin. SURF was used to study the adsorption at the air/water interface. SURF is a time-of-flight instrument and measured the sample at incident angles of 0.35°, 0.65° and 1.5° to give a Q range of 0.01 – 0.4 $Å^{-1}$ [10]. FIGARO was used to study the adsorption at the SiO_2/water interface. The sample in FIGARO was measured at two angles of 0.62° and 3.8° giving a Q range of 0.0045 to 0.42 $Å^{-1}$ [11].

NR measurements were carried out at air/liquid and solid/liquid interfaces. In air/liquid NR experiments, the sample solution was poured into Teflon troughs placed on the beam line. As the water surface is kept horizontal, only the height needs to be scanned to find the exact reflected surface before starting a NR measurement. The measurements in air/water NR experiments were performed in three contrasts, including protonated samples (h-samples) in D_2O, chain deuterated samples (d-samples) in D_2O and null reflection water (NRW). The SLD of NRW is same to that of air which is zero, so the contrast of d-samples in NRW is useful to detect the total thickness of the layer and adsorbed amount. With the help of three contrasts, the structure of the adsorbed layer can be studied, e.g. the thicknesses of the layers in the air and under water. In solid/liquid NR experiments, the sample solution was injected into a specially designed liquid cell which is clamped against the large polished surface of a silicon (Si) block ($50\times80\times10$ mm^3). Similarly, to air/liquid measurements, the height alignment scanning is carried out firstly. Then, the sample angle alignment scanning is carried out to determine the angle values where the intensity of reflected neutrons is maximal. The height and angle scanning are then repeated to maximise the reflectivity from the interface, so that the solid/liquid NR measurements can optically performed. The measurements in SiO_2/water NR experiments were performed in three contrasts, including h-samples in D_2O, d-samples in D_2O and CM1.31 (contrast matches 1.31), which are similar to those in air/water NR experiments. The contrast of

h-samples in D_2O is helpful to detect the total thickness of the layer and adsorbed amount. The contrast of d-samples in D_2O is sensitive to head groups. CM1.31 has the same SLD value to that of head groups of C_nLCs, so this contrast has a clear probe to the deuterated chain. With the help of three contrasts, the thicknesses of different layers and the water fraction can be examined. When neutrons are scattered from planar and laterally homogeneous layers, the specular reflection is observed. The inhomogeneities of samples lead to higher signal of off-specular scattering, such as roughness or voids [12]. For the interfacial adsorption of C_nLC, the adsorbed layer is planar and laterally homogeneous resulting in specular reflection in NR experiments.

Reference

[1] S.E. Harding, K. Jumel, Light Scattering, Current protocols in protein science 11(1) (1998) 7.8. 1-7.8. 14.

[2] J. Stetefeld, S.A. McKenna, T.R. Patel, Dynamic Light Scattering: A Practical Guide and Applications in Biomedical Sciences, Biophys Rev 8(4) (2016) 409-427.

[3] Dynamic Light Scattering: An Introduction in 30 Minutes, 2021. https://warwick.ac.uk/fac/cross_fac/sciencecity/programmes/internal/themes/am2/boo king/particlesize/intro_to_dls.pdf.

[4] How Isis Works, 2021. https://www.isis.stfc.ac.uk/Pages/How-ISIS-works.aspx.

[5] Description of the Ill High-Flux Reactor, 2021. https://www.ill.eu/reactor-and-safety/high-flux-reactor/technical-characteristics.

[6] R. Heenan, J. Penfold, S. King, Sans at Pulsed Neutron Sources: Present and Future Prospects, Journal of Applied Crystallography 30(6) (1997) 1140-1147.

[7] J. Zhang, H. Gong, M. Liao, Z. Li, R. Schweins, J. Penny, J.R. Lu, How Do Terminal Modifications of Short Designed Iikk Peptide Amphiphiles Affect Their Antifungal Activity and Biocompatibility?, Journal of Colloid and Interface Science 608 (2022) 193-206.

[8] R. Cubitt, G. Fragneto, Neutron Reflection:: Principles and Examples of Applications, Scattering, Elsevier2002, pp. 1198-1208.

[9] R.A. Pethrick, J. Dawkins, Modern Techniques for Polymer Characterisation, J. Wiley1999.

[10] H. Liu, X. Hu, Z. Li, K. Fa, H. Gong, K. Ma, M. Liao, P. Li, J.R. Webster, J.T. Petkov, R.K. Thomas, J.R. Lu, Surface Adsorption and Solution Aggregation of a Novel Lauroyl-L-Carnitine Surfactant, Journal of Colloid and Interface Science 591 (2021) 106-114.

[11] H. Liu, K. Fa, X. Hu, Z. Li, K. Ma, M. Liao, L. Zhang, R. Schweins, A. Maestro, P. Li, J.R.P. Webster, J.T. Petkov, R.K. Thomas, J. Lu, How Do Chain Lengths of Acyl-L-Carnitines Affect Their Surface Adsorption and Solution Aggregation?, Journal of Colloid and Interface Science (2021).

[12] R. Pynn, S.M. Baker, G. Smith, M. Fitzsimmons, Off-Specular Scattering in Neutron Reflectometry, Journal of Neutron Research 7(3, 4) (1999) 139-158.

Chapter 3

Surface Adsorption and Solution Aggregation of a Novel Lauroyl-L-Carnitine Surfactant

Huayang Liu[1], Xuzhi Hu[1], Zongyi Li[1], Ke Fa[1], Haoning Gong[1], Kun Ma[2], Mingrui Liao[1], Peixun Li[2], John RP Webster[2], Jordan T. Petkov[3], Robert K. Thomas[4], Jian Ren Lu[1,*]

[1] Biological Physics Laboratory, School of Physics and Astronomy, University of Manchester, Oxford Road, Manchester, M13 9PL, UK.

[2] ISIS Neutron Facility, Rutherford Appleton Laboratory, STFC, Chilton, Didcot, Oxon OX11 0QX, UK.

[3] Arch UK Biocides Ltd, Lonza, Hexagon Tower, Delaunays Road, Blackley, Manchester M9 8ZS, UK.

[4] Physical and Theoretical Chemistry, University of Oxford, South Parks, Oxford OX1 3QZ, UK

*Author to whom correspondence should be addressed. Email: j.lu@manchester.ac.uk

Abstract

Hypothesis: L-carnitine plays a crucial role in the cellular production of energy by transporting fatty acids into mitochondria. Acylated L-carnitines are amphiphilic and if appropriate physical properties were demonstrated, they could replace many currently used surfactants with improved biocompatibility and health benefits.

Experiments: This work evaluated the surface adsorption of lauroyl-L-carnitine ($C_{12}LC$) and its aggregation behavior. The size and shape of the aggregates of $C_{12}LC$ surfactant were studied at different temperatures, concentrations, pH and ionic strength by dynamic light scattering (DLS) and small-angle neutron scattering (SANS). Surface tension measurements were carried out to determine the critical micellar concentration (CMC) of $C_{12}LC$. Combining with the Gibbs equation, the surface excess at different concentrations could be determined. Neutron reflection (NR) was used to determine the structure of the adsorbed layer at the air/water interface with the help of isotopic contrast variations.

Findings: At pH 7, the limiting area per molecule (A_{CMC}) of the zwitterionic $C_{12}LC$ adsorbed layer at the air/water interface was found to be 46 $Å^2$ from surface tension and neutron reflection, smaller than the values of $C_{12}PC$, $C_{12}E_5$, DTAB, $C_{12}C_4$betaine and $C_{12}C_8$betaine but close to that of SDS. A pronounced surface tension minimum at pH 2 at the low ionic strength was linked to a minimum value of area per molecule of about 30 $Å^2$, indicating the competitive adsorption from traces of lauric acid produced by hydrolysis of $C_{12}LC$. As the concentration increased, the area per molecule reached a plateau of 37-39 $Å^2$, indicating the dissolution of the more surface-active lauric acid into the micelles of $C_{12}LC$. DLS and SANS showed that the size and shape of micelles has little response to temperature, concentration, ionic strength or pH. The SANS profiles measured under 3 isotopic contrasts could be well fitted by the core-

shell model, giving a spherical core radius of 15.7 ± 0.5 Å and a shell thickness of 10.5 ± 0.5 Å. The decrease of pH led to more protonated carboxyl groups and more positively charged micelles, but the micellar structures remained unchanged, in spite of their stronger interaction. These features make $C_{12}LC$ potentially attractive as a solubilizing agent.

1. Introduction

As a chiral molecule, carnitine exists as two stereoisomers, L-carnitine and D-carnitine, mirror images of each other. L-carnitine is the form that is predominantly present in animal bodies [1, 2]. L-carnitine molecules play an important role in the oxidation of fats. Thus, acylated L-carnitines act as transporters of long-chain fatty acids such as palmitic acids into mitochondria for oxidation and energy production. These carnitine species also facilitate the transport of the fatty acids across the different mitochondrial membrane spaces by forming long chain carnitine esters involving various carnitine acyltransferases and carnitine and acylcarnitine translocases [3]. Although our bodies can synthesize L-carnitine from lysine side chains to meet the demand of energy production, some individuals with genetic disorders or medical conditions cannot make enough and it must then come from external food sources or nutrient supplies.

L-carnitine has been claimed to contribute to weight loss in many studies of obesity, a topic of substantial concern in the past few decades [4]. Excess weight can cause health problems including type II diabetes, fatty liver and cardiovascular diseases [5]. By improving fat metabolism and glycogen breakdown in muscle [3] and β-oxidation of fatty acids in mitochondria [1], L-carnitine enhances fat consumption. It has also been suggested that L-carnitine intake could reduce reliance on exercise [6] and strengthen endurance capacity [7].

The intermediate acyl-L-carnitine derivatives formed during fat metabolic processes are surfactants by nature. And, as surfactants, they probably also play other physiological roles. The intramitochondrial relationship between CoA (co-enzyme A) and acyl-CoA can be detected by means of the extramitochondrial ratio of acyl-L-carnitine to L-carnitine [8] and this is also a critical indicator in the identification of mitochondrial dysfunction [1]. It has been suggested that long-chain acyl-L-carnitines

cause a harmful effect on human red blood cells, possibly associated with membrane-lytic activity due to their surfactant behavior [9]. In addition, L-carnitine esters with long alkyl or acyl chain have been reported as broad-spectrum antimicrobial compounds [10], and have potential application in gene delivery as well [11]. Alkyl/acyl carnitine derivatives also have potential biomedical use due to their biocompatibility [12]. Whilst extensive studies have been undertaken to exploit their biological functions, there is so far a lack of experimental work devoted to understanding their physical properties including their membrane-lytic actions on different cell types including bacteria and fungi. Such progress would also enable us to evaluate their potential as biocompatible emulsifiers and biocides and optimize their efficacy as a function of acyl chain length and concentration.

Lauroyl-L-carnitine ($C_{12}LC$) is an acyl-L-carnitine ester surfactant with a hydrophilic head (L-carnitine) and a hydrophobic tail (C_{12}-chain). Because of its amphiphilic nature, it has the potential to self-aggregate [13] and adsorb at surfaces in aqueous solution [12]. Like other surfactants, it is expected that $C_{12}LC$ aggregates to form micelles with a core-shell structure when the concentration is above the critical micelle concentration (CMC). The size and shape of surfactant micelles will depend on the differing lengths of alkyl chains and on head group modifications [14, 15], and the micellar structures may also be influenced by other stimuli such as surfactant concentration [16], pH, temperature [17, 18], and ionic strength [15]. However, the lack of studies on $C_{12}LC$ micellar properties limits our understanding to this novel surfactant and its potential application.

Adsorption at the air/water interface offers a useful assessment in the development of a new surfactant. The adsorbed amount and area per molecule depend on the particular molecular structure of the surfactant, its type, concentration range, pH and

ionic strength [19]. Surface tension measurements together with the application of the Gibbs equation can lead to the surface excess or adsorbed amount under different solution conditions. More direct information on the adsorbed layer structure at the air/water interface can be obtained from neutron reflectivity measurements in combination with deuterium labelling [20].

A better understanding of the physical properties of a biocompatible and surface active molecule has the potential to increase its applications and $C_{12}LC$ was chosen as an illustrative example. Dynamic Light Scattering (DLS) and Small Angle Neutron Scattering (SANS) have been used to study the size and shape of its self-assembled micelles. Its surface excess and the structure of its adsorbed layer on the surface of water were studied by surface tension measurements and neutron reflection. The results from these studies enable a comparison of the properties of $C_{12}LC$ with more common surfactants. Given the strong biological relevance of the acyl-L-carnitine series, this study also explores the surface properties of $C_{12}LC$ with respect to changes in pH and ionic strength.

2. Experimental Section

2.1. Materials

Lauroyl-L-carnitine ($C_{12}LC$) (purity ≥99%) was provided by Lonza. It was also synthesized separately following a method developed at Lonza [21]. The chain deuterated lauroyl-L-carnitine ($dC_{12}LC$) was synthesized at the ISIS Deuteration Laboratory, Rutherford Appleton Laboratory, STFC as follows. Deuterated dodecanoic acid (5.0 g, 22.4 mmol, >98%D) was dissolved in excess thionyl chloride (10 ml) and stirred at room temperature to form deuterated lauroyl chloride. The reaction was monitored by TLC. The L-carnitine hydrochloride salt (4.33 g, 21.9 mmol) was mixed with trichloroacetic acid (7.16 g, 43.8 mmol). The mixture was

heated to 70 °C for 30 min to melt. The temperature was then reduced to 50 °C and the deuterated lauroyl chloride was added dropwise. The system was then heated up to 70 °C with stirring for 16 hr. After cooling down, the crude product was precipitated out by adding 1-propanol. The white solid was filtered via a Bűchner funnel and recrystallized from acetone to give the chain deuterated lauroyl-L-carnitine hydrochloride salt. The characterization of the chain deuterated $C_{12}LC$ is given in **Table 3.S6** in **Supporting Information**.

Purification of the raw $C_{12}LC$ sample was as follows. 5-10 g of $C_{12}LC$ was first dissolved in 100 mL UHQ (ultrapure water) and titrated with 0.2 M NaOH solution with stirring to adjust the pH to 7. The solution was then freeze dried for 3-4 days to remove residual water. The dry powder was dissolved in hot absolute ethanol (purity ≥99%) and filtered to remove solid NaCl. The solvent was removed by rotary evaporation. The neutral $C_{12}LC$ was dissolved with dry acetone in a conical flask and heated to 50 °C. Absolute ethanol was titrated into the flask until the cloudy solution just became clear. The flask was then left at room temperature for at least a day to crystallize. Recrystallization was repeated 2-3 times to remove the trace impurities from the sample. Note that MS and H-NMR analyses could not identify any difference in the purity of the successive recrystallizations, and the final purity could only be confirmed by surface tension measurements.

2.2. Characterization measurements

Dynamic light scattering (DLS)

DLS uses a laser to illuminate the particles present in aqueous phase and detects the intensity fluctuation of the light scattered by them due to Brownian motion. The theory and method of DLS is described in the **Supporting Information**. The hydrodynamic radii of the micelles formed by the surfactant were measured by DLS

using a Malvern Instruments Zetasizer Nano-ZS adopting backscatter detection (173°

detection optics). 1 mL of surfactant solution was loaded in a cuvette (12.5×12.5×48

mm^3 with a path length of 10 mm). Before each measurement, the sample was

equilibrated for 20 min. The hydrodynamic radius from each measurement was

determined by averaging 10 runs.

Small angle neutron scattering (SANS)

SANS can provide the size and shape of surfactant assemblies in the range of 1 nm to

100 nm. SANS measurements were performed on the LOQ diffractometer and on the

SANS configuration Larmor instrument at ISIS Pulsed Neutron Source, STFC

Rutherford Appleton Laboratory, Didcot, UK. LOQ is a time-of-flight instrument

which utilizes a beam of neutrons with a wavelength (λ) range from 0.2 Å to 10 Å,

leading to a Q range of 0.008 – 0.3 Å^{-1}. Q = $(4\pi/\lambda)\sin(\theta)$ where 2θ is the scattering

angle [17]. Larmor was operated in the SANS mode with a wavelength between 0.9 Å

and 12.5 Å to provide a Q range of 0.003 - 0.5 Å^{-1}. Hydrogenated C_{12}LC (hC_{12}LC)

and dC_{12}LC were dissolved in D_2O and H_2O to provide three contrasts to determine

the structure of the different parts of the micelles. Surfactant samples in D_2O were

loaded in Hellma quartz cells with 2 mm path length, and samples in H_2O were in

quartz cells with 1 mm path length. Quartz cells were placed in the sample changer

connected with a Julabo water bath and the temperature was controlled at 10, 25 or

40 °C for the SANS runs. Empty cells, D_2O and H_2O were also measured at 10, 25

and 40 °C, and the scattering from the cell, air, and solvent were subtracted from the

data. SANS data profiles were initially fitted with a basic core-shell sphere model [22].

Combinations with more contrasts using the charged core-shell sphere model (core-

shell sphere with structure factor: hayter_msa) [23, 24] were used to fit charged

micelles at pH 2. The uncharged core-shell sphere model (core-shell sphere with

structure factor: hard sphere) [25] was used at pH 7 to fit zwitterionic micelles. The

resulting physical constants for C_{12}LC are listed in **Table 3.S1 of Supporting**

Information, and the analysis method and estimation of the shell and core from SLD is also described in the **Supporting Information**.

Surface tension measurements

A Krüss K11 tensiometer was used to measure the surface tension of surfactant solutions by the Du Noüy ring method. Typically a maximum of 2 h was required for the surface tension to equilibrate, and equilibrium surface tensions were determined until the standard deviation of 10 successive runs was less than 0.1 mN·m^{-1}. The critical micelle concentration (CMC) at 25 °C was estimated from the plot of surface tension against the natural logarithm of concentration where straight lines were drawn through the data points just below and above the break point. The CMC was taken to be at the intersection of the two lines.

The Gibbs equation is:

$$-d\gamma = RT \sum_i \Gamma_i dln a_i \qquad (3.1)$$

where γ is the surface tension, R is the gas constant, T is the temperature (usually 25 °C in this work), Γ_i is the surface excess with respect to water, and a_i is the activity of component i in solution [26]. Thus, the Gibbs equation relates surface concentration with bulk concentration through changes in surface tension. The activity describes how 'active' a component is compared to itself under the standard state conditions, a is normally approximated to the concentration c when the surfactant concentration is low. For an ionic surfactant the surfactant molecule is dissociated into a surfactant ion and a counterion and equation (3.1) then become [27]

$$-\frac{d\gamma}{RT} = \Gamma_s dln c_s + \Gamma_i dln c_i \quad . \qquad (3.2)$$

In this work, the concentration of salt ions was kept constant and in excess, so that the equation reduces to

$$\Gamma_s = -\frac{1}{nRT}\left(\frac{d\gamma}{dlnc_s}\right) = -\frac{1}{RT}\left(\frac{d\gamma}{dlnc_s}\right) \tag{3.3}$$

where n = 1 under all solution conditions studied.

Neutron reflection (NR)

Neutron reflectivity can provide structural characteristics of the adsorbed layer at the air/water interface when different contrasts are combined. Previous work has demonstrated that the contrast of deuterated chain surfactant in null reflecting water (NRW) can be used to determine the adsorption amount of the surfactant at the interface [20, 28]. Combined with the extra contrasts of h-surf and d-surf in different solvent conditions, further information can be obtained about the adsorbed layer structure.

NR measurements were performed on the SURF reflectometer, also at the ISIS Pulsed Neutron Source. SURF is a time-of-flight (TOF) instrument with the neutron wavelength range between 0.5 and 6.9 Å. A supermirror was used to provide 3 incidence angles of 0.35°, 0.65° and 1.5° to measure the momentum transfer range from 0.01 to 0.5 Å^{-1} [29]. Reflectivity at the air/D$_2$O interface was measured to calibrate the instrument. dC$_{12}$LC in NRW and D$_2$O and a hydrogenated version in D$_2$O were measured to determine the surface excess and structure of the adsorbed layer at room temperature (23±2 °C). NRW, with scattering length density (SLD) matched to air ($\rho_{Air} = 0$), contains 8.2vol% D$_2$O and 91.8vol% H$_2$O [20].

In NRW measurements, the surfactant layer can be fitted with a uniform layer model because the water is invisible. The SLD of the layer (ρ_l) can be calculated by using

$$\sigma_s \rho_s = \rho_l \tag{3.4}$$

where σ_s denotes the volume fraction of surfactant and ρ_s denotes the SLD of the surfactant. The area per molecule, A, can be related to the thickness of the layer, τ, and the volume of the surfactant molecule, V_s

$$A\tau\sigma_s = V_s. \tag{3.5}$$

Combining equations (3.4) and (3.5) in this model, the area per molecule can be expressed as

$$A = \frac{V_s \rho_s}{\tau \rho_l}. \tag{3.6}$$

The surface excess can be calculated from

$$\Gamma = \frac{1}{A N_a} \tag{3.7}$$

where N_a is the Avogadro number.

The SLD of D$_2$O ($\rho_{D_2O}=6.35\times10^{-6}$ Å^{-2}) is quite different from air ($\rho_{Air} = 0$) and a two-layer model is a suitable model for this set of measurements. The SLD of the layer in air (ρ_1) can be calculated by

$$\sigma_1 \rho_{s1} = \rho_1 \tag{3.8}$$

where σ_1 denotes the volume fraction of part of the surfactant in the air and ρ_{s1} denotes its SLD. This is similar to that in NRW. The SLD of the layer immersed in the water (ρ_2) can be determined by using

$$\sigma_2 \rho_{s2} + (1 - \sigma_2)\rho_{D_2O} = \rho_2 \tag{3.9}$$

where σ_2 is the volume fraction of water part of surfactant and ρ_{s2} is the SLD of the part containing surfactant and water. A and Γ values in each layer were calculated using equations (3.6) and (3.7) subject to the constraint of constant A.

3. Results and discussion

3.1. Surface tension and CMC

The surface tension for $C_{12}LC$ was measured at pH 7 under buffer solutions with 2 different ionic strengths. As shown in **Figure 3.1(a)**, the CMC (critical micellar concentration) was found to be 1 mM at pH 7 and 25 °C, with changes in ionic strength from 10 mM to 160 mM (close to the physiological ionic strength of human blood) showing little impact on the CMC or surface tension. At this pH, the carboxylic group on the head of the surfactant is almost fully dissociated and carries a negative charge, while the trimethylammonium group on the same head carries a positive charge. The net charge of $C_{12}LC$ is zero and so it is zwitterionic. Hence, the ionic strength has little effect on either its surface tension or CMC at pH 7. This feature is the same as alkyl phosphocholine surfactants such as $C_{12}PC$ [30] and is also consistent with the behavior of nonionic alkyl ethoxylate surfactants such as $C_{12}E_5$ [30].

Previous studies have indicated that the presence of surfactant-active impurities, even at very low levels, can cause a noticeable minimum close to the CMC in the surface tension-ln[Concentration] plot [31]. A well-known example is the presence of traces of dodecanol in the anionic surfactant sodium dodecyl sulphate (SDS) where the depth of the surface tension minimum around the CMC is dependent on the level of dodecanol contamination [32]. In contrast, the absence of a minimum around the CMC of $C_{12}LC$ at pH 7 suggests its high purity and hence absence of any surface active organic impurities.

Table 3.1 summarizes the CMC and surface tension of $C_{12}LC$ in comparison with other surfactants also with 12 carbon chains. The CMC of $C_{12}LC$ at pH 7 is close to $C_{12}PC$ and $C_{12}C_8$betaine, but is higher than that of $C_{12}E_5$ and lower than those of DTAB, SDS and $C_{12}C_4$betaine. In the presence of a physiological level of salt, the CMCs for SDS and DTAB would drop to 2-3 mM. The surface tension values at the CMC are around 40 mN·m^{-1}, except that for nonionic $C_{12}E_5$ which is 30 mN·m^{-1} and for $C_{12}C_4$betaine which is 45 mN·m^{-1}. The lack of impact of salt on both the CMC and the surface tension at the CMC, and the low values of CMC and surface tension at the CMC, are potentially useful features of the acyl carnitines.

Table 3.1. Comparison of CMC, surface tension and area per molecule at CMC of surfactants with 12 carbon chains.

Surfactant	CMC (mM)	Surface tension (mN·m^{-1})	A_{CMC} (Å^2)	Ref.
$C_{12}LC$	1.1	41	46	This work
$C_{12}PC$	0.9	40	52	[28]
$C_{12}E_5$	0.07	30	50	[33]
DTAB	14.5	40	50	[34]
SDS	8.0	41	48	[35]
$C_{12}C_4$betaine	3.3	45	53	[27]
$C_{12}C_8$betaine	1.0	42	77	[27]

When the pH is decreased to 2, the carboxylic group on the head of $C_{12}LC$ is almost fully protonated but the trimethylammonium group remains positively charged due to the quaternised nitrogen. The surfactant is now cationic. **Figure 3.1(a)** shows the surface tension profile at low ionic strength, which is strongly reduced in comparison with that measured at pH 7 at the same low ionic strength. There are two main differences between the surface tension profiles in the two situations. First, the surface tension at pH 2 shows a much steeper decline with increasing surfactant concentration and becomes lower than that measured at pH 7 when the concentration is close to 1 mM. Application of the Gibbs equation shows that the values of the apparent area per $C_{12}LC$ molecule at pH 2 are then much smaller than those estimated at pH 7, implying

a very different surface molecular packing. In addition, as the concentration of $C_{12}LC$ rises above 1 mM, the surface tension decreases even further, reaching a minimum at about 2.7 mM before it rises again up to a plateau of 38 mN/m.

The molecular basis underlying such surface tension behavior is uncertain. **Figure 3.1(b)** shows the chemical structure of $C_{12}LC$. As a carboxylic ester, $C_{12}LC$ is vulnerable to hydrolysis with one of the products being the highly surface active lauric acid as shown in **Figure. 3.1(b)**. The possible effect of lauric acid on $C_{12}LC$ at pH 2 can be assessed by comparison with that of dodecanol on the surface tension behavior of SDS, which is well understood [32]. Both dodecanol and lauric acid have low solubilities, neither forms micelles, and they can be spread on water to give extremely low surface tensions of about 25 $mN \cdot m^{-1}$ [36].

The surface tension data of lauric acid have been measured at pH 1 (no ionization of the acid) [37], pH 2 , pH 7 and pH 11 (with the salt) [37] and are plotted in **Figure 3.S1**. As shown in **Figure 3.S1**, the data at pH 1 and 2 are similar and the data at pH 7 are close to the average of the two limits (pH 1 and pH 11). Comparison with the dodecanol-SDS data reveals that a strong minimum in surface tension occurs when the solubility limit of the dodecanol is reached at or below the CMC of SDS. The amount of dodecanol in the solution can be written as βc where β is the mole fraction of dodecanol relative to the SDS concentration c. Thus, the surface tension drops to a very low value if βc is comparable with or less than the CMC. Above the CMC, the SDS micelles dissolve the dodecanol and essentially remove the monomers from the solution. Since the surface tension of the micellar SDS is about 35 mN/m, which is higher than the limiting surface tension of dodecanol, the result is a strong minimum in the surface tension. The addition of salt does not change the solubility of dodecanol but it lowers the CMC of SDS sufficiently that micellization may now occur well

below the solubility limit of dodecanol. Exactly the same arguments apply to the lauric acid-C_{12}LC system except that addition of electrolyte also increases the solubility of lauric acid, as can be seen in **Figure 3.S1**. Thus, addition of electrolyte is more effective to weaken the effect of lauric acid as impurity on surface tension in the lauric acid-C_{12}LC mixtures than in the dodecanol-SDS case.

From **Figure 3.S1** the solubility limit at pH 2 is around 0.02mM where the surface tension is close to 30 mN/m at room temperature. The low surface tension in **Figure 3.1(a)** is at about 2.5 mM for an ionic strength of 10 mM. Comparing these two numbers indicates that a molar fraction of about 1/125 (less than 1 mol%) of lauric acid would cause the effect observed. When the ionic strength is increased at pH 2, it has two effects. Firstly, the CMC of C_{12}LC drops to about 1 mM, at which point the 0.8 mol% impurity would give a total concentration of 0.008 mM of lauric acid, which is now below the solubility limit. The second effect is that the addition of electrolyte also increases the value of the solubility at the saturation point. As shown in **Figure 3.S1** the solubility limit at pH 2 with ionic strength (160mM) will increase to around 0.2 mM which is much higher than that at pH 2 with low ionic strength. This would further weaken the surface effect of the lauric acid. So the surface tension plot for this pH and concentration shows only a very small dip. For pH 7 the CMC at 1 mM would have less lauric acid than 0.008 mM at pH 2, because C_{12}LC is stable in the neutral environment. The amount of lauric acid is now well below its solubility limit of 1 mM at this pH as shown in **Figure 3.S1**. Thus, the surface tension measurements show no dip around CMC at 10 mM and 160 mM electrolyte, both as observed.

The surface tension - ln[concentration] measurements below their CMCs were fitted with a quadratic equation as described by the continuous lines in **Figure 3.1**.

Combining these fits with the Gibbs equation shown as equation (3) leads to the estimate of changes in surface adsorbed amount Γ, from which the area per molecule can be derived using equation (7). **Table 3.1** shows the area per molecule of $C_{12}LC$ at its CMC (A_{CMC}) and pH 7 is 46 Å^2. This value compares well with other surfactants summarized in Table 1 in spite of the large differences in their CMCs. Besides, these values from the surface tension data are listed in **Table 3.2**, allowing direct comparison with those from neutron reflection to be made.
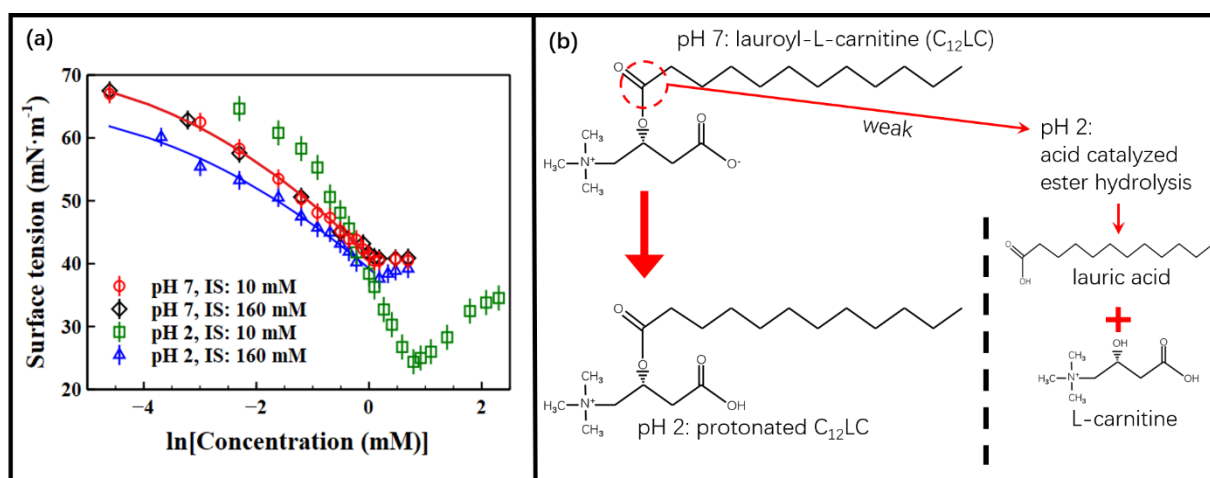
Figure 3.1. (a) Surface tension data plotted against ln[concentration] for $C_{12}LC$ at pH 7 and 2 with low and high ionic strengths (IS) of 10 mM and 160 mM, respectively. Data points below CMCs were fitted with the best quadratic equations against ln[concentration] as shown in continuous lines and then fed into the Gibbs equation to derive surface adsorbed amount and area per molecule. No fit is shown to the data measured at the low ionic strength of pH 2 due to the ambiguity of its CMC. (b) The chemical structures of $C_{12}LC$ at pH 7 and the protonated $C_{12}LC$ at pH 2. A small part of $C_{12}LC$ is hydrolyzed into lauric acid and L-carnitine at pH 2.

Table 3.2. CMC values of $C_{12}LC$ determined from surface tension, adsorbed amount at CMC (Γ_{CMC}) and area per molecule at CMC (A_{CMC}) from the Gibbs equation and

neutron reflection at pH 7 with different ionic strengths (IS). Because at pH 2 the CMC value is unclear, data at CMC in pH 2 could not be determined.

	Surface tension		Neutron reflection	
	pH 7			
	Ionic strength: 10 mM	Ionic strength: 160 mM	Ionic strength: 10 mM	Ionic strength: 160 mM
CMC (mM)	1.1±0.1	1.1±0.1		
Γ_{CMC} (mol·m^{-2}×10^{-6})	3.6±0.1	3.6±0.1	3.64±0.14	3.60±0.10
A_{CMC} (Å^2)	46±1	46±1	45.6±2.0	46.0±1.6

3.2. Solution aggregation in different concentrations and temperatures

Aggregation of the C$_{12}$LC solutions under different conditions was first checked by dynamic light scattering (DLS). Changes in the hydrodynamic radius of the C$_{12}$LC aggregates in the aqueous phase (pH 7 with ionic strength: 10 mM) at surfactant concentrations of 5, 20 and 80 mM in a temperature range from 10 to 40 °C with 5 °C interval are shown in **Table 3.S2**. It is evident from the data that the radii of the aggregates are similar at 25 ± 2 Å and the sizes do not change much at different concentrations and temperatures. Note that the radii measured from DLS were derived assuming spherical geometry for the aggregates. DLS does not have sufficient resolution to distinguish other shapes and hence is only a useful indicator for assessing micellar sizes when planning SANS experiments [14].

The shape and structural composition of the micellar aggregation was measured by SANS in combination with H/D substitution involving the fully hydrogenated and acyl chain deuterated C$_{12}$LC. SANS studies were undertaken under similar concentration and temperature combinations to the DLS measurements. A typical set of runs involves hC$_{12}$LC in D$_2$O, as exemplified in **Figure 3.S2**. It shows that there is a high scattering intensity from micelles at these concentrations, but the shape of the micelles shows little change as shown by the fitted parameters in **Table 3.S3**. The core-shell sphere model was used to make the simultaneous fits of the parallel SANS

profiles measured under different concentrations and temperatures to extract the key structural parameters of the $C_{12}LC$ micelles. The best-fit parameters as shown in **Table 3.S3** indicate that the micelles of $C_{12}LC$ were close to a sphere with a core radius of 15.7±0.5 Å and a shell thickness of 10.6±0.5 Å, giving a total radius of 26.3±1.0 Å, consistent with the DLS data. Patra et al [38] have synthesized a single chain cationic surfactant by forming an amide bond between the dodecyl amine and the acid group of the D,L-carnitine. In contrast to the T-shaped structure of $C_{12}LC$, their molecule is largely linear. As a result, it is cationic and its CMC is at 3.4 mM at 25 °C. it prefers to form a bilayer structure in the aqueous solution. H-bonding between the head groups strengthens the flat bilayer structuring with its preference to form vesicles increasing with concentration. High resolution transmission electron microscopic measurements revealed the diameters of the vesicles in the range of 30-70 nm [38]. These differences in their aggregational properties originate from the position of the hydrophobic tail and the removal of the weak acidic charge.

The aggregation number per micelle can be estimated using tail and head volumes based on the following equations [30, 39]:

$$V_{tail} = 27.4 + 26.9n_c \qquad (3.10)$$

$$V_{head} = V_{C_{12}LC} - V_{tail} \qquad (3.11)$$

where n_c is the number of carbon atoms on the acyl chain. For the lauroyl chain, the first 11 carbon chain was taken as the tail and the -C=O was considered as part of the head group. The calculated values are also shown in Table S1. The aggregation number as determined from the above method was 50±3, which was found to be invariant at the different surfactant concentrations and temperatures studied.

3.3. Aggregation in different pH and ionic strength

The influence of pH on the $C_{12}LC$ micellar structure was studied by SANS over the range from 7 to 5 and then to 2 at a concentration of 20 mM and temperature of 25 °C. The possible effects of pH dependent charge state and interaction for the surfactant micelles is shown schematically in **Figure 3.2(a)**. Due to the charge response of the carboxyl group, the head group of the surfactant varies from no net charge at pH 7, to a weak positive charge at pH 5 and then strongly positive at pH 2. As observed from the chemical structure of $C_{12}LC$ shown in **Figure 3.2(b)**, the deprotonation of the carboxyl in the head group at pH 7 and then its almost complete protonation at pH 2 are as expected [40]. As explained above, the quaternary ammonium is always positively charged from pH 7 to 2, so that the $C_{12}LC$ molecule is zwitterionic at pH 7 but becomes strongly cationic at pH 2. The SANS data measured from the hydrogenated $C_{12}LC$ ($hC_{12}LC$) in D_2O for pH = 7, 5 and 2 at 20 mM and 25 °C are shown in **Figure 3.2(c)**. The data analysis shows that when the effects of the different surface charges on the interparticle interactions are taken into account the scattering profiles can be fitted to almost exactly the same spherical micelle. **Table 3.3** provides a summary of the key structural parameters, showing the response of the structural characteristics of the micelles from a charged core-shell sphere as the environment becomes acidic to an almost zero charge at pH 7. During the pH change, however, the sizes of the micelles do not change in neutral or acidic environment. The fitted data in **Table 3.3** supports the models depicted in **Figure 3.2(a)** with no net charge at pH 7 and hence the formation of zwitterionic micelles, weakly charged micelles with net charges of 5±2 per micelle at pH 5 and then micelles with strong surface charges of 18±4 at pH 2, showing strong electrostatic repulsion between the cationic micelles in water.
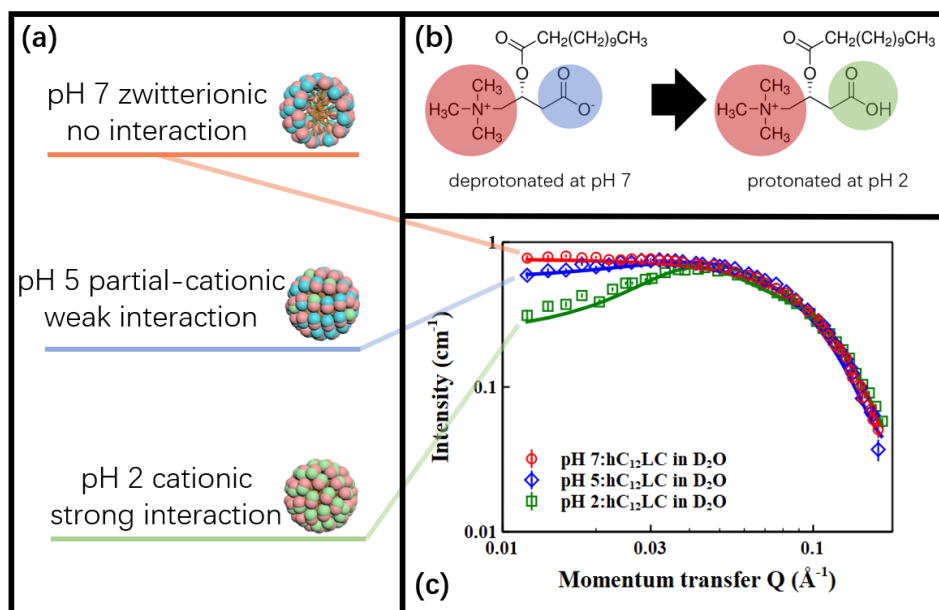
Figure 3.2. (a) Schematic depictions of different surface charges and interactions of the micelle model in response to pH changes with the total ionic strength fixed at 10 mM. (b) The chemical structural change of the zwitterionic $C_{12}LC$ from the deprotonated carboxyl group at pH 7 to the cationic $C_{12}LC$ with the protonated carboxyl group at pH 2. (c) SANS profiles measured from $hC_{12}LC$ in D_2O with pH changed from 7 (○), to 5 (◇) and then 2 (□) at the concentration of 20 mM, with the fitted curves shown as continuous lines following the core-shell charged sphere model.

Table 3.3. The average best-fit structure parameters from the core-shell charged sphere model for the $C_{12}LC$ (20mM) micelles in different pH and ionic strength. Further structural details from each contrast are shown in **Table 3.S4** in **Support Information**.

pH	Ionic strength (mM)	Core radius (Å)	Shell thickness (Å)	Aggregation number	Micelle charge
7		15.7±0.5	10.5±0.5	51±3	0
5	10	15.7±0.5	10.6±0.6	50±3	5±2
2		15.5±0.4	10.3±0.5	48±4	18±4
7	160	15.7±0.5	10.5±0.5	50±3	0
2	160	15.7±0.5	10.3±0.4	50±3	18±4

SANS measurements for each set of three contrasts were taken at 20 mM and 25 °C involving $hC_{12}LC$ in D_2O, $dC_{12}LC$ in H_2O and D_2O at pH 2 and 7 at low and high

ionic strengths. SANS profiles at pH 7 at 10 mM and 160 mM ionic strengths are shown in **Figure 3.3(a)**. The best-fit parameters at each contrast are shown in **Table 3.S4**. The average best-fit parameters, as summarized in **Table 3.3,** indicate that the net charge of the zwitterionic micelles is close to zero and an increase of ionic strength to 160 mM (data not shown) has no effect to the structure of the micelles at pH 7. Decreasing the pH to 2 has a significant effect on the interaction and charges of the micelles. **Figure 3.3(b)** shows that positively charged micelles have a strong repulsive interaction with each other at this pH, particularly at the low ionic strength. The micelle charge increases from 0 at pH 7 to 18 at pH 2 due to the protonation of the carboxyl groups on the heads of the surfactants in the micelles. The presence of high surface charges also implies that fewer Cl ions are attached to the surface of the cationic quaternary amine groups on the micelle surface. As already indicated, a change in the charge state from the lowering of pH has no effect on the size and shape of the micelles. As shown in **Figure 3.3(c)**, at a high ionic strength of 160 mM, the interaction is weaker than that at 10 mM ionic strength because of the electrostatic screening. The simultaneous data fitting also confirms the structural parameters shown in **Table 3.3** and the almost invariant shape and size of the micelles with pH and ionic strength. The equivalent amounts of Na^+ and Cl^- are distributed close to the surface of the micelles as the ionic strength increases, resulting in a reduced Debye length [41-43]. Since the Debye length decreases with increasing ionic strength, even to less than the radius of micelles, the effective gap between neighboring particles narrows. Thus, the electrostatic shielding weakens the repulsive interaction between the cationic micelles.
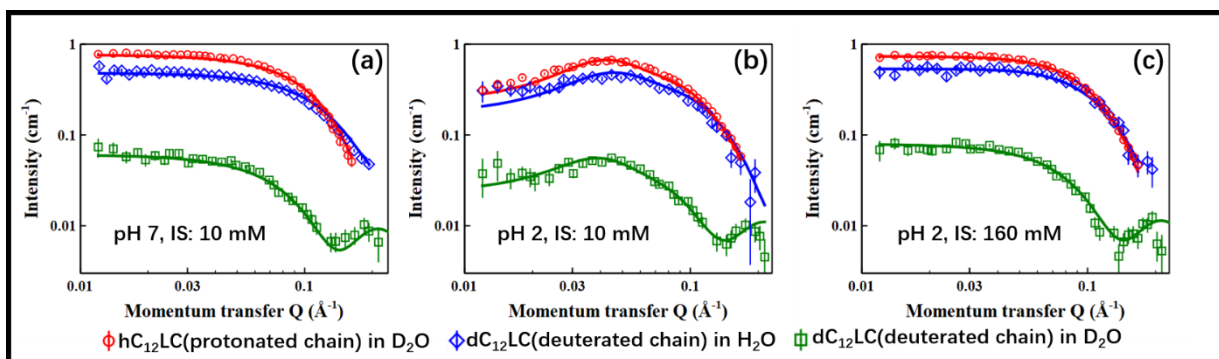
Figure 3.3. SANS profiles measured from three contrasts of $hC_{12}LC$ in D_2O ($\circ$), $dC_{12}LC$ in H_2O ($\diamond$) and D_2O ($\square$) (a) at pH 7 at a low ionic strength of 10 mM, (b) at pH 2 at a low ionic strength of 10 mM and (c) at pH 2 at a high ionic strength of 160 mM. The continuous lines represent the best-fit curves from the core-shell charged sphere model.

3.4. Neutron reflection

Neutron reflection measurements were carried out at different concentrations to examine how the adsorbed layer structure varies with surface coverage. The neutron reflectivity profiles of $dC_{12}LC$ in NRW at a range of concentrations from below to above the CMC at pH 7 and pH 2 were measured, with the reflectivity profiles shown in Supporting Information. As shown by the neutron profiles in **Figure 3.S3** and **Figure 3.S4**, the intensity of reflected neutrons from $dC_{12}LC$ layer increases to a maximum at 1.2 mM at pH 7. However, at pH 2, the intensity should have a higher value at 3 mM and should decrease as the concentration increases. As mentioned above, the measurement in NRW can be fitted with a one-layer model, because the SLDs of NRW and air are equal to zero. The results from the best-fit uniform layer model for NRW data are summarized in **Table 3.S5**. At pH 7, the thickness of the layer increases with concentration below the CMC, and the thickness of the layer is 22 ± 1 Å when the concentration is above CMC at pH 7. Γ and A can be calculated from equation (3.7) and their values Γ (red circles) and A (blue diamonds) are plotted

in **Figure 3.4(b)**. These show that the surface excess increases with concentration below the CMC (1 mM) with the area per molecule showing a concurrent decrease. The surface excess tends to a constant value around the CMC at $3.7\pm0.2\times10^{-6}$ mol·m^{-2}, indicating that $C_{12}LC$ reaches its plateau adsorption at the CMC at pH 7. The saturated area per molecule of $C_{12}LC$ of 46 ± 2 Å^2 is smaller than the values of $C_{12}PC$, $C_{12}E_5$, DTAB, $C_{12}C_4$betaine and $C_{12}C_8$betaine as summarized in **Table 3.1**, but is close to that of SDS. Compared with $C_{12}C_n$betaines, they have a similar carboxyl betaine as the head group, but the carbon chain in $C_{12}LC$ is connected to the middle position of the head group in L-carnitine, resulting in a T-shape head. Thus, the T-shape head group apparently occupies a smaller area at the air/water interface than the linear shape. The area calculated from surface tension data by the Gibbs equation (A_{Gibbs}) is also summarized in **Table 3.S5** for comparison with A_{NR}. As **Figure 3.S5** shows, the two independent results over the concentration range below CMC are consistent within error. Significantly, the zwitterionic $C_{12}LC$ at pH 7 is treated like nonionic surfactant with a prefactor n = 1 [26] in the Gibbs equation to calculate Γ and A.

The same neutron reflection measurements were carried out over a similar concentration range at pH 2. Data in **Table 3.S5** indicate that the thickness from the uniform layer model increases as the concentration goes up and reaches a maximum of 23 ± 1 Å at 3 mM which is slightly higher than the thickness at CMC at pH 7. It can also be seen from **Figure 3.4(c)** that the surface excess increases to a maximum as the concentration goes up, and then starts to decrease above 3 mM, finally reaching a plateau adsorption at around 8 mM. The area per molecule and surface tension change in the opposite direction. The practical limitation in the application of the Gibbs equation to ionic surfactants [44] associated with the occurrence of the surface tension minimum around the CMC leads to large discrepancies. The maximum surface excess at 3 mM is $5.7\pm0.2\times10^{-6}$ mol·m^{-2}, and both area per molecule and surface tension

reach their minimum values, 29 ± 2 Å^2 and 23 ± 1 mN·m^{-1}, respectively. As the concentration increases to 8 mM, C$_{12}$-L-canitine reaches a plateau adsorption with a surface excess of $4.3\pm0.2\times10^{-6}$ mol·m^{-2}, which is slightly higher than the plateau values at pH 7. The area per molecule and surface tension are correspondingly 38 ± 2 Å^2 and 34 ± 1 mN·m^{-1}, respectively.

Neutron reflectivity profiles at the 3 contrasts are shown in **Figure 3.4(a)**, hC$_{12}$LC in D$_2$O, dC$_{12}$LC in D$_2$O and NRW. The two-layer model was found to be appropriate to fit the neutron reflectivity data simultaneously, and the best-fit parameters are summarized in **Table 3.S6**. From the two-layer model, the chain region in air was found to be 12.2 ± 0.5 Å, and the underwater region involving the head groups was 9.3 ± 0.5 Å at 2 mM at pH 7. The number of water molecules associated with each L-carnitine head group (n_w) was estimated to be approximately 7 from the thickness and volume of the head group. This value is lower than n_w of 15 for C$_{12}$PC and that of 10 for C$_{12}$E$_5$ [20]. This suggests a lower level of hydration for L-carnitine than in the PC and E$_5$ head groups. These differences may reflect their relative affinity for water. As shown in the structure cartoon in **Figure 3.4(d)**, these structural parameters indicate that there are on average two carbons from the tail that are immersed in water, which is slightly higher than the chain fraction immersed in water for C$_{12}$PC [20]. At pH 2 and the same concentration, the thicknesses of the two regions increased to 13.0 ± 0.3 Å and 10.1 ± 0.7 Å, respectively, but the parameters from the two-layer model are consistent with those from the single one-layer model as described previously.

Figure 3.4(d) provides a schematic description of the structural changes of the adsorbed surfactant layer at the air/water interface over the concentration range below and above the CMC at pH 7 and 2, respectively. At pH 7, the C$_{12}$LC molecules are zwitterionic and they adsorb at the air/water interface with their head groups lying flat.

Increase in surfactant concentration simply increases surface packing, with saturated adsorption being reached above the CMC. From the two-layer model, the chain immersed fraction is estimated to be around 0.18. Salt addition has little impact due to the zwitterionic nature. As a result, the surface excess and area per molecule do not change much at pH 7. At pH 2, as mentioned above, there may be a small contribution from lauric acid produced by hydrolysis of $C_{12}LC$. At this pH, even a small concentration of lauric acid may reach its solubility limit and hence enhance the surface excess around CMC, resulting in smaller measured area per molecule. As the concentration of $C_{12}LC$ increases, the lauric acid is dissolved into the $C_{12}LC$ micelles. Addition of salt decreases the CMC of cationic $C_{12}LC$ and makes the micellization occur at a lower concentration.

In the opposite situation to the horizontal alignment of the head group, where the acyl tail is projected almost vertically, the head group must adopt a highly tilted conformation to occupy a smaller footprint area as depicted in **Figure 3.4(d)**. The head groups must also adopt a zig-zag arrangement to maximize the distance between charge groups. As depicted by the cartoon structure for close to the CMC at pH 2, the crowding of $C_{12}LC$ molecules at the interface probably also contributes to increasing the layer thickness. The head groups must now become highly inclined and the tails will be more vertical than at pH 7. As the concentration of $C_{12}LC$ increases, the lauric acid is dissolved into the bulk solution by $C_{12}LC$ micelles, and finally the interface is saturated with cationic and zwitterionic $C_{12}LC$ around 8 mM.
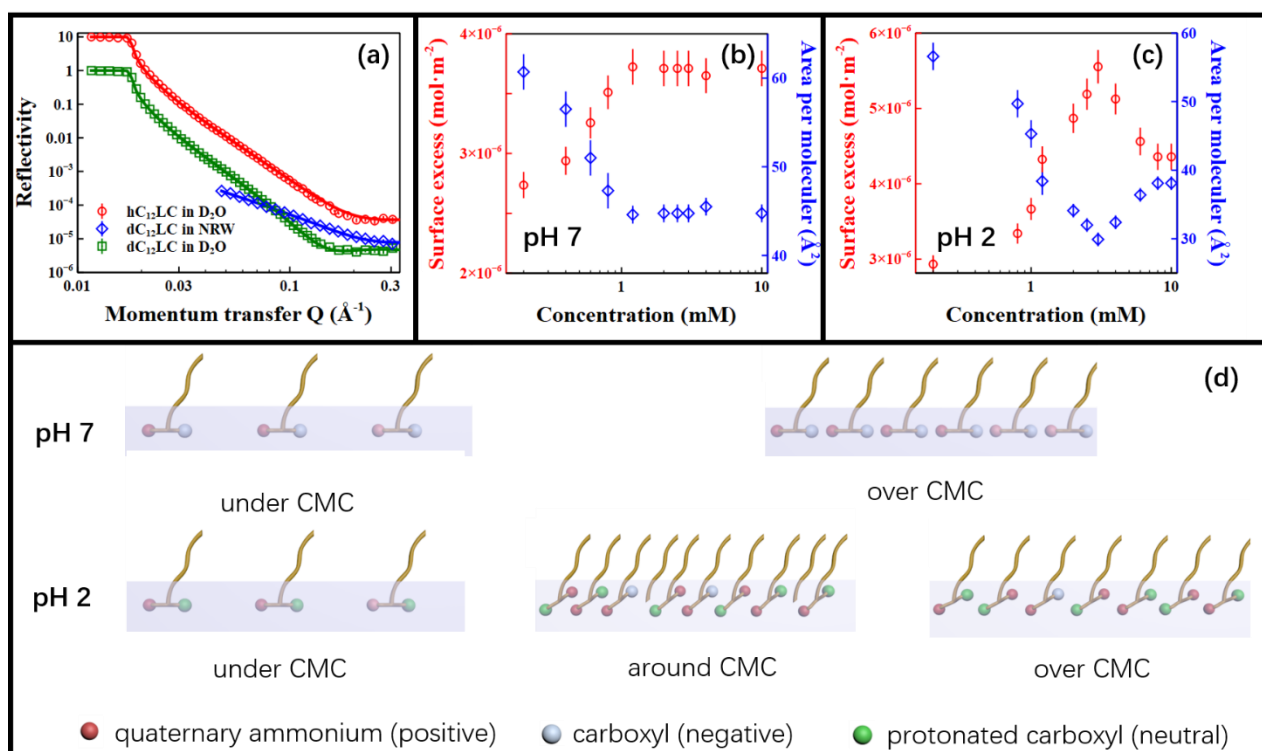
Figure 3.4. (a) Neutron reflection profiles from SURF reflectometer measured at 3 contrasts: $hC_{12}LC$ (2 mM) in D_2O (○), shifted by multiplying 10 times to give a clear view, $dC_{12}LC$ in NRW(◇) and D_2O (□) at pH 7 with an ionic strength of 10 mM. (b) Surface excess and area per molecule from the best simultaneous neutron reflectivity fits at pH 7. (c) Surface excess and area per molecule from the best simultaneous neutron reflectivity fits at pH 2. (d) Cartoon model to show the effects of pH and concentration below and above the CMC.

4. Conclusion

As natural biosurfactants, acyl-L-carnitines have been shown to play important roles in metabolic processes that manifest very interesting surface and colloidal behavior. But these properties have previously not been fully studied. $C_{12}LC$ is a good model for this group of molecules with their characteristic T-shaped head groups with a permanent cationic charge on one side and a pH responsive carboxyl group on the other side. The pH response dictates the surface and leads to a solution behavior that

is representative of both ionic and zwitterionic surfactants. DLS and SANS studies have shown that the actual physical structures of the micelles do not vary much with pH, temperature or ionic strength, but do respond to pH in terms of surface charges and their interaction. $C_{12}LC$ micelles remain predominantly spherical, with a core radius of 15.7 Å and a shell thickness of 10.5 Å, and the aggregation number remains approximately constant at 50, smaller than expected from the geometrical features of the micelles of $C_{12}PC$ [30], although $C_{12}LC$ has a similar shell thickness to $C_{12}PC$.

Whilst $C_{12}LC$'s surface adsorption at pH 7 follows a simple zwitterionic surfactant behavior, its adsorption at pH 2 displays an "unexpected" behavior characterised by the occurrence of a distinct surface tension minimum around 2.7 mM at low ionic strength. This pattern of behavior was significantly suppressed by an increase of ionic strength. This unusual phenomenon was explained by the weak hydrolysis of $C_{12}LC$. The surface-active lauric acid reaches its solubility limit under the conditions studied, leading to a minimum in the surface tension, similar to that caused by n-dodecanol as an impurity in SDS [32]. The surface tension minimum was matched by the highest surface excess with an average area per molecule below 30 $Å^2$, characteristic of competitive adsorption of lauric acid. However, addition of salt decreased the CMC of $C_{12}LC$ and increased the solubility limit of lauric acid, so the lauric acid was removed from surface via dissolution into the micelles of $C_{12}LC$. This process suppressed the minimum of surface tension. Neutron reflection revealed the area per molecule at pH 7 around the CMC to be 46 $Å^2$, slightly smaller than those of zwitterionic $C_{12}PC$ [20] and $C_{12}C_4$betaine [27] but their layer thicknesses of 21 - 23 Å were comparable. The range of surface and solution properties will help to develop novel applications utilizing this new T-shaped carnitine surfactant, exploiting its self-assembly features with pH-responsive surface charges. The pH responsive behavior of acyl-L-carnitines could work well as vehicles for loading drug/gene at neutral pH and then releasing under the acidic environment, a feature attractive for developing skin and cancer

treatments. However, the same pH-triggered loading and release response together with antimicrobial ability and biocompatibility could also offer potential for developing stomach treatments [45].

Acknowledgments

Supporting Information

Further information on the working principles of DLS, SANS and neutron reflection, data analysis to SANS and neutron reflectivity profiles are shown in the Supporting Information document. Supporting data are available on request from the corresponding author

Reference

[1] S.E. Reuter, A.M. Evans, Carnitine and Acylcarnitines, Clinical Pharmacokinetics 51(9) (2012) 553-572.

[2] J. Harmeyer, The Physiological Role of L-Carnitine, Lohman Information 27 (2002) 15-21.

[3] A. Jeukendrup, R. Randell, Fat Burners: Nutrition Supplements That Increase Fat Metabolism, Obesity Reviews 12(10) (2011) 841-851.

[4] M. Fried, V. Hainer, A. Basdevant, H. Buchwald, M. Deitel, N. Finer, J.W. Greve, F. Horber, E. Mathus-Vliegen, N. Scopinaro, Interdisciplinary European Guidelines on Surgery of Severe Obesity, Obesity Facts 1(1) (2008) 52-59.

[5] M. Pooyandjoo, M. Nouhi, S. Shab-Bidar, K. Djafarian, A. Olyaeemanesh, The Effect of (L-) Carnitine on Weight Loss in Adults: A Systematic Review and Meta-Analysis of Randomized Controlled Trials, Obesity Reviews 17(10) (2016) 970-976.

[6] B.T. Wall, F.B. Stephens, D. Constantin-Teodosiu, K. Marimuthu, I.A. Macdonald, P.L. Greenhaff, Chronic Oral Ingestion of L-Carnitine and Carbohydrate Increases Muscle Carnitine Content and Alters Muscle Fuel Metabolism During Exercise in Humans, The Journal of Physiology 589(4) (2011) 963-973.

[7] J.H. Kim, J.H. Pan, E.S. Lee, Y.J. Kim, L-Carnitine Enhances Exercise Endurance Capacity by Promoting Muscle Oxidative Metabolism in Mice, Biochemical and Biophysical Research Communications 464(2) (2015) 568-573.

[8] R. Pons, D.C. De Vivo, Primary and Secondary Carnitine Deficiency Syndromes, Journal of Child Neurology 10(2_suppl) (1995) 2S8-2S24.

[9] A. Kobayashi, H. Watanabe, S. Fujisawa, T. Yamamoto, N. Yamazaki, Effects of L-Carnitine and Palmitoylcarnitine on Membrane Fluidity of Human Erythrocytes, Biochimica et Biophysica Acta (BBA) - Biomembranes 986(1) (1989) 83-88.

[10] M. Calvani, L. Critelli, G. Gallo, F. Giorgi, G. Gramiccioli, M. Santaniello, N. Scafetta, M.O. Tinti, F. De Angelis, L-Carnitine Esters as "Soft", Broad-Spectrum Antimicrobial Amphiphiles, Journal of Medicinal Chemistry 41(13) (1998) 2227-2233.

[11] J. Wang, X. Guo, Y. Xu, L. Barron, F.C. Szoka, Synthesis and Characterization of Long Chain Alkyl Acyl Carnitine Esters. Potentially Biodegradable Cationic Lipids for Use in Gene Delivery, Journal of Medicinal Chemistry 41(13) (1998) 2207-2215.

[12] J. Nivet, M. Le Blanc, J. Riess, Synthesis and Preliminary Evaluation of Perfluoroalkylacyl Carnitines as Surfactants for Biomedical Use, European Journal of Medicinal Chemistry 26(9) (1991) 953-960.

[13] S.H. Yalkowsky, G. Zografi, Some Micellar Properties of Long-Chain Acylcarnitines, Journal of Colloid and Interface Science 34(4) (1970) 525-533.

[14] F.N. Padia, M. Yaseen, B. Gore, S. Rogers, G. Bell, J.R. Lu, Influence of Molecular Structure on the Size, Shape, and Nanostructure of Nonionic C N E M Surfactant Micelles, The Journal of Physical Chemistry B 118(1) (2014) 179-188.

[15] Z. Wang, P. Li, K. Ma, Y. Chen, J. Penfold, R.K. Thomas, D.W. Roberts, H. Xu, J.T. Petkov, Z. Yan, The Structure of Alkyl Ester Sulfonate Surfactant Micelles: The Impact of Different Valence Electrolytes and Surfactant Structure on Micelle Growth, Journal of Colloid and Interface Science 557 (2019) 124-134.

[16] E. Pambou, J. Crewe, M. Yaseen, F.N. Padia, S. Rogers, D. Wang, H. Xu, J.R. Lu, Structural Features of Micelles of Zwitterionic Dodecyl-Phosphocholine (C12pc) Surfactants Studied by Small-Angle Neutron Scattering, Langmuir 31(36) (2015) 9781-9789.

[17] X. Hu, H. Gong, Z. Li, S. Ruane, H. Liu, P. Hollowell, E. Pambou, C. Bawn, S. King, S. Rogers, How Does Solubilisation of Plant Waxes into Nonionic Surfactant Micelles Affect Pesticide Release?, Journal of Colloid and Interface Science 556 (2019) 650-657.

[18] X. Hu, H. Gong, Z. Li, S. Ruane, H. Liu, E. Pambou, C. Bawn, S. King, K. Ma, P. Li, What Happens When Pesticides Are Solubilized in Nonionic Surfactant Micelles, Journal of Colloid and Interface Science 541 (2019) 175-182.

[19] A.J. Prosser, E.I. Franses, Adsorption and Surface Tension of Ionic Surfactants at the Air–Water Interface: Review and Evaluation of Equilibrium Models, Colloids and Surfaces A: Physicochemical and Engineering Aspects 178(1) (2001) 1-40.

[20] M. Yaseen, J.R. Lu, J.R.P. Webster, J. Penfold, The Structure of Zwitterionic Phosphocholine Surfactant Monolayers, Langmuir 22(13) (2006) 5825-5832.

[21] D.L.M. Smida, TN), Process for the Production of a Fatty Acid/Carnitine Derivative, Lonza Ltd. (Visp, CH), United States, 2013.

[22] J.B. Hayter, J. Penfold, Determination of Micelle Structure and Charge by Neutron Small-Angle Scattering, Colloid and Polymer Science 261(12) (1983) 1022-1030.

[23] J.B. Hayter, J. Penfold, An Analytic Structure Factor for Macroion Solutions, Molecular Physics 42(1) (1981) 109-118.

[24] J.-P. Hansen, J.B. Hayter, A Rescaled Msa Structure Factor for Dilute Charged Colloidal Dispersions, Molecular Physics 46(3) (1982) 651-656.

[25] J.K. Percus, G.J. Yevick, Analysis of Classical Statistical Mechanics by Means of Collective Coordinates, Physical Review 110(1) (1958) 1.

[26] P.X. Li, Z.X. Li, H.H. Shen, R.K. Thomas, J. Penfold, J.R. Lu, Application of the Gibbs Equation to the Adsorption of Nonionic Surfactants and Polymers at the Air-Water Interface: Comparison with Surface Excesses Determined Directly Using Neutron Reflectivity, Langmuir 29(30) (2013) 9324-9334.

[27] K. Ma, P.X. Li, C.C. Dong, R.K. Thomas, J. Penfold, Unusual Adsorption at the Air-Water Interface of a Zwitterionic Carboxybetaine with a Large Charge Separation, Langmuir 32(14) (2016) 3340-3347.

[28] M. Yaseen, Y. Wang, T. Su, J. Lu, Surface Adsorption of Zwitterionic Surfactants: N-Alkyl Phosphocholines Characterised by Surface Tensiometry and Neutron Reflection, Journal of Colloid and Interface Science 288(2) (2005) 361-370.

[29] Z. Li, R. Li, C. Smith, F. Pan, M. Campana, J.R. Webster, C.F. van der Walle, S. Uddin, S.M. Bishop, R. Narwal, Neutron Reflection Study of Surface Adsorption of Fc, Fab, and the Whole Mab, ACS Applied Materials & Interfaces 9(27) (2017) 23202-23211.

[30] E. Pambou, J. Crewe, M. Yaseen, F.N. Padia, S. Rogers, D. Wang, H. Xu, J.R. Lu, Structural Features of Micelles of Zwitterionic Dodecyl-Phosphocholine (C(1)(2)Pc) Surfactants Studied by Small-Angle Neutron Scattering, Langmuir 31(36) (2015) 9781-9789.

[31] L. Shedlovsky, J. Ross, C.W. Jakob, The Effect of Certain Impurities on the Surface and Interfacial Tension of Aqueous Solutions of Sodium Dodecyl Sulfonate, Journal of Colloid Science 4(1) (1949) 25-33.

[32] J.R. Lu, I.P. Purcell, E.M. Lee, E.A. Simister, R.K. Thomas, A.R. Rennie, J. Penfold, The Composition and Structure of Sodium Dodecyl Sulfate-Dodecanol Mixtures Adsorbed at the Air-Water Interface: A Neutron Reflection Study, Journal of Colloid and Interface Science 174(2) (1995) 441-455.

[33] E. Tyrode, C.M. Johnson, M.W. Rutland, P.M. Claesson, Structure and Hydration of Poly (Ethylene Oxide) Surfactants at the Air/Liquid Interface. A

Vibrational Sum Frequency Spectroscopy Study, The Journal of Physical Chemistry C 111(31) (2007) 11642-11652.

[34] A. Espert, R.v. Klitzing, P. Poulin, A. Colin, R. Zana, D. Langevin, Behavior of Soap Films Stabilized by a Cationic Dimeric Surfactant, Langmuir 14(15) (1998) 4251-4260.

[35] J.R. Lu, A. Marrocco, T.J. Su, R.K. Thomas, J. Penfold, Adsorption of Dodecyl Sulfate Surfactants with Monovalent Metal Counterions at the Air-Water Interface Studied by Neutron Reflection and Surface Tension, Journal of Colloid and Interface Science 158(2) (1993) 303-316.

[36] L.D.A. Chumpitaz, L.F. Coutinho, A.J.A. Meirelles, Surface Tension of Fatty Acids and Triglycerides, Journal of the American Oil Chemists' Society 76(3) (1999) 379-382.

[37] E. Lucassen-Reynders, A Surface Equation of State for Mixed Surfactant Monolayers, Journal of Colloid and Interface Science 41(1) (1972) 156-167.

[38] T. Patra, S. Ghosh, J. Dey, Cationic Vesicles of a Carnitine-Derived Single-Tailed Surfactant: Physicochemical Characterization and Evaluation of in Vitro Gene Transfection Efficiency, Journal of Colloid and Interface Science 436 (2014) 138-145.

[39] C. Tanford, Micelle Shape and Size, The Journal of Physical Chemistry 76(21) (1972) 3020-3024.

[40] W. Zhang, G. Zhang, L. Du, C. Zhang, L. Li, J. Zhu, J. Pei, J. Wu, Synthesis of Hydroxyl-Terminated Polybutadiene Bearing Pendant Carboxyl Groups by Combination of Anionic Polymerization and Blue Light Photocatalytic Thiol-Ene Reaction and Its Ph-Triggered Self-Assemble Behavior, Reactive and Functional Polymers 127 (2018) 161-167.

[41] R. Tadmor, E. Hernández-Zapata, N. Chen, P. Pincus, J.N. Israelachvili, Debye Length and Double-Layer Forces in Polyelectrolyte Solutions, Macromolecules 35(6) (2002) 2380-2388.

[42] C.-H. Chu, I. Sarangadharan, A. Regmi, Y.-W. Chen, C.-P. Hsu, W.-H. Chang, G.-Y. Lee, J.-I. Chyi, C.-C. Chen, S.-C. Shiesh, Beyond the Debye Length in High Ionic Strength Solution: Direct Protein Detection with Field-Effect Transistors (Fets) in Human Serum, Scientific Reports 7(1) (2017) 1-15.

[43] R. Pashley, B. Ninham, Double-Layer Forces in Ionic Micellar Solutions, Journal of Physical Chemistry 91(11) (1987) 2902-2904.

[44] H. Xu, P.X. Li, K. Ma, R.K. Thomas, J. Penfold, J.R. Lu, Limitations in the Application of the Gibbs Equation to Anionic Surfactants at the Air/Water Surface: Sodium Dodecylsulfate and Sodium Dodecylmonooxyethylenesulfate above and Below the Cmc, Langmuir 29(30) (2013) 9335-9351.

[45] R. Hamed, A. Awadallah, S. Sunoqrot, O. Tarawneh, S. Nazzal, T. AlBaraghthi, J. Al Sayyad, A. Abbas, Ph-Dependent Solubility and Dissolution Behavior of Carvedilol—Case Example of a Weakly Basic Bcs Class Ii Drug, Aaps Pharmscitech 17(2) (2016) 418-426.

[46] M. Instruments, Zetasizer Nano Series User Manual, MAN0317 1 (2004) 2004.

[47] J. Stetefeld, S.A. McKenna, T.R. Patel, Dynamic Light Scattering: A Practical Guide and Applications in Biomedical Sciences, Biophysical Reviews 8(4) (2016) 409-427.

[48] A.J. Jackson, Introduction to Small-Angle Neutron Scattering and Neutron Reflectometry, NIST Center for Neutron Research (2008) 1-24.

Supporting information

Surface Adsorption and Solution Aggregation of a Novel Lauroyl-L-Carnitine Surfactant

Huayang Liu[1], Xuzhi Hu[1], Zongyi Li[1], Ke Fa[1], Haoning Gong[1], Kun Ma[2], Mingrui Liao[1], Peixun Li[2], John RP Webster[2], Jordan T. Petkov[3], Robert K. Thomas,[4] Jian Ren Lu[1,*]

[1] Biological Physics Laboratory, School of Physics and Astronomy, University of Manchester, Oxford Road, Manchester, M13 9PL, UK.

[2] ISIS Neutron Facility, Rutherford Appleton Laboratory, STFC, Chilton, Didcot, Oxon OX11 0QX, UK.

[3] Arch UK Biocides Ltd, Lonza, Hexagon Tower, Delaunays Road, Blackley, Manchester M9 8ZS, UK.

[4] Physical and Theoretical Chemistry, University of Oxford, South Parks, Oxford OX1 3QZ, UK

*Author to whom correspondence should be addressed. Email: j.lu@manchester.ac.uk

1.Experimental Techniques and Theoretical Background

1.1 Dynamic light scattering (DLS)

DLS measures Brownian motion by using a laser to illuminate the particles and it detects the intensity fluctuations of light scattered by the particles [46]. The Zetasizer Nano DLS instrument has a detector at 90° and backscatter detection at 173°[47]. The analysis of the data leads to the translational diffusion coefficient (m^2/s), D_τ, which is used to obtain the hydrodynamic radius, r_h, using the Stokes-Einstein equation:

$$D_\tau = \frac{k_B T}{6\pi\eta r_h} \qquad (3.\text{S1})$$

where k_B is the Boltzmann coefficient, T is the temperature in K, and η is the viscosity of the medium in N·s/m^2. The hydrodynamic radius is defined as the radius of a hypothetical sphere particle in the system, which offers a good estimate of the micellar size.

1.2 Data analysis for small angle neutron scattering (SANS)

The scattering intensity profile (I) obtained from a micellar sample can be described by [30]

$$I(q) = NP(q)S(q) + background \qquad (3.\text{S2})$$

where q represents the momentum transfer, $P(q)$ is the form factor representing scattering from different parts of the micelles and $S(q)$ is the structure factor representing scattering from inter-micellar effects. Following background subtraction

[30, 48] the data was analysed using the basic core-shell sphere model. For a sphere of radius r, the form factor $P_{sphere}(q)$ can be written as [30, 48]:

$$P_{sphere}(q) = \Delta\rho V^2 \left(\frac{3(sin(qr)-qrcos(qr))}{V(qr)^3}\right)^2 \qquad (3.S3)$$

where $\Delta\rho$ is the scattering length density difference of the sphere and the solvent and V is the volume of the sphere. The core-shell sphere model can be considered as a spherical core that is surrounded by a shell, with uniform scattering densities of ρ_{core} and ρ_{shell}. The core-shell sphere form factor $P_{core-shell}$ can be written as:

$$P_{core-shell}(q) = \left(V_{core}(\rho_{core} - \rho_{shell})\frac{3(sin(qr_{core})-qr_{core}cos(qr_{core}))}{V(qr_{core})^3} + \right.$$
$$\left. V_{total}(\rho_{shell} - \rho_{solvent})\frac{3(sin(qr_{total})-qr_{total}cos(qr_{total}))}{V(qr_{total})^3}\right)^2. \quad (3.S4)$$

In the present experiment, at pH 7 the $C_{12}LC$ micelles are zwitterionic and have no electrostatic interaction with other micelles. The sample solution is dilute, and the inter-micellar effects are negligible, and the structure factor $S(q) = 1$ [30, 48]. When the pH is lower (e.g. pH 5 and pH 2), the $C_{12}LC$ micelles will carry positive charges and interact with other cationic micelles. In this case, during SANS data fitting we used the Hayter-Penfold Rescaled Mean Spherical Approximation (RMSA) structure factor which was developed for a system of charged scatterers in a dielectric medium [23, 24].

2. SANS data fitting analysis on $C_{12}LC$ micellar structure

The basic core-shell model was used to analyse the measured SANS intensity profiles using the software SASVIEW (version 4.2.2). The physical constants for $C_{12}LC$ used in SANS data analysis are listed in **Table 3.S1**. The core consists of an hydrophobic acyl chain which is slightly different from the dodecyl chain in $C_{12}PC$ [30]. From the

SLD of the hydrated head group region covering the micelles, the percentage of water in the shell is given by the following relation:

$$\sigma_{head}\rho_{head} + \sigma_{solvent}\rho_{solvent} = \rho_{shell} \qquad (3.S5)$$

$$\sigma_{head} + \sigma_{solvent} = 100\% \qquad (3.S6)$$

where σ_{head} and $\sigma_{solvent}$ are the volume fractions of the head groups and solvent (D_2O or H_2O) in the shell. ρ_{head} and $\rho_{solvent}$ are the respective scattering length densities.

Table 3.S1. Physical constants for hydrogenated and chain deuterated C_{12}-L-carnitine used in the data analysis

Segments	Scattering Length/b ($\times 10^{-5}$ Å)	Volume/V (Å^3)	Scattering length density/ρ (Å$^{-2}\times 10^{-6}$)
Protonanted tail ($C_{11}H_{23}$)	-12.9	323	-0.40
Deuterated tail ($C_{11}D_{23}$, 98%D)	226.5	323	7.01
Head (hL-carnitine with -C=O)	33.4	255	1.31
H_2O	-1.7	30	-0.56
D_2O	19.1	30	6.35

3. Supplementary data collected in the work

3.1 Surface tension of lauric acid at different pHs.
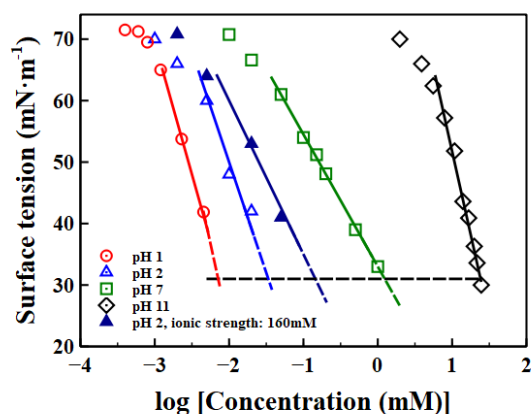
Figure 3.S1. Surface tension of lauric acid at pH 1 [37], pH 2, pH 7 and pH 11 [37]. The straight lines are drawn and extended by dashed lines to intercept the horzontal dashed line indicating solubility limit under each pH.

Figure 3.S1 shows the surface tension behavior of lauric acid at pH 1, pH 2, pH 7 and pH 11. The black dashed line gives a surface tension close to 30 mN/m where the concentration of lauric acid should be close to its solubility limit. From **Figure 3.S1**, the solubility limit of lauric acid is estimated to be about 0.01 mM at pH 1, 0.02 mM pH 2, 1mM at pH 7, and 25 mM at pH 11. The limit of lauric acid at pH 2 with 150 mM NaCl is increased to around 0.2 mM.

3.2 Hydrodynamic radius from DLS

Table 3.S2. Dynamic light scattering data for C_{12}-L-carnitine in different concentrations and temperatures at pH 7 with ionic strength (10mM).

Concentration (mM) and temperature (°C)	Hydrodynamic radius from DLS (Å)
20 mM, 10 °C	24±1 Å
20 mM, 15 °C	23±2 Å
20 mM, 20 °C	25±1 Å
20 mM, 25 °C	24±2 Å
20 mM, 30 °C	24±1 Å
20 mM, 35 °C	25±1 Å
20 mM, 40 °C	25±1 Å
5 mM, 25 °C	23±2 Å
80 mM, 25 °C	24±1 Å

3.3 SANS profiles and best-fit parameters in different concentrations and temperatures
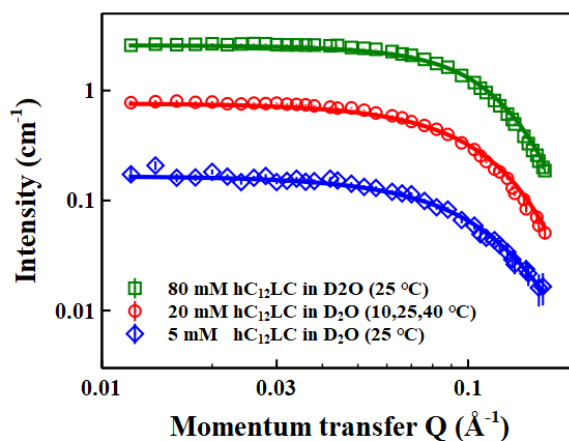
Figure 3.S2. SANS profiles for hC$_{12}$LC measured in D$_2$O with different concentrations (5 mM, 20 mM and 80 mM) at pH 7, ionic strength:10mM. Continuous lines are the best-fit lines for the measured SANS profiles.

Figure 3.S2 shows the SANS profiles and best-fit lines from different surfactant concentrations. The data indicate that high concentration leads to high SANS intensity. The best-fit structural parameters as shown in **Table 3.S3** reveal little difference between the different concentrations.

Table 3.S3. The best-fit structural parameters from the core-shell sphere model for the C$_{12}$LC micelles at pH 7 and ionic strength of 10 mM under different concentrations and temperatures.

Concentration and temperature	Core radius(Å)	ρ_{core} (Å^{-2}×10^{-6})	Shell Thickness (Å)	ρ_{shell} (Å^{-2}×10^{-6})	N$_{agg}$	Volume fraction	χ_R^2
80 mM (25 °C)	15.7±0.5	-0.4±0.1	10.5±0.5	4.4±0.3	50±3	0.056±0.004	2.02
20 mM (10,25,40 °C)	15.7±0.5	-0.4±0.1	10.6±0.5	4.5±0.3	50±2	0.013±0.001	0.98

5 mM (25 °C)		15.7±0.5	-0.4±0.1	10.6±0.5	4.5±0.3	50±3		0.003±0.001	1.09

In **Table 3.S3**, ρ_{core} and ρ_{shell} are the best fit scattering length density (SLD) of the core and shell of the micelles. N_{agg} is the aggregation number of each micelle. Volume fractions of the micelles could be expressed by following the equation:

$$Volume\ fraction = \frac{Volume\ of\ micelles}{Volume\ of\ solution}. \quad (3.S7)$$

And χ_R^2 is a parameter to show the 'goodness' of the fit. When it tends to 1, it means the fit is ideal.

3.4 The best-fit SANS parameters in pH 7 and 2 with ionic strengths of 10 mM and 160 mM from the three isotopic contrasts

Table 3.S4. The best-fit structure parameters from three contrasts using the core-shell charged model for the $C_{12}LC$ micelles at 20 mM and 25 °C under different pHs and ionic strengths.

pH/ Ionic strength	Contrasts	Core radius (Å)	ρ_{core} ($Å^{-2} \times 10^{-6}$)	Shell thickness (Å)	ρ_{shell} ($Å^{-2} \times 10^{-6}$)	N_{agg}	N_{charge}	Volume fraction	χ_R^2
pH 7 IS: 10 mM	$hC_{12}LC/D_2O$	15.7±0.5	-0.4±0.1	10.6±0.5	4.5±0.3	50±2	0	0.013±0.001	0.98
	$dC_{12}LC/H_2O$	16.2±0.5	6.9±0.1	10.4±0.4	0.3±0.1	54±3	0	0.013±0.001	1.30
	$dC_{12}LC/D_2O$	15.4±0.4	6.9±0.1	10.5±0.4	4.9±0.3	48±3	0	0.013±0.001	3.66
pH 7 IS: 160 mM	$hC_{12}LC/D_2O$	15.6±0.4	-0.4±0.1	10.5±0.4	4.6±0.2	49±3	0	0.013±0.001	0.93
	$dC_{12}LC/H_2O$	15.8±0.5	6.9±0.1	10.8±0.5	0.1±0.1	51±3	0	0.013±0.001	1.65
	$dC_{12}LC/D_2O$	15.8±0.5	6.9±0.1	10.1±0.3	5.0±0.3	51±3	0	0.013±0.001	4.85
pH 2 IS: 10 mM	$hC_{12}LC/D_2O$	15.5±0.4	-0.4±0.1	10.3±0.4	4.6±0.3	48±4	18±3	0.013±0.001	1.88
	$dC_{12}LC/H_2O$	15.7±0.5	6.9±0.1	10.6±0.5	0.2±0.1	50±3	15±4	0.013±0.001	1.13
	$dC_{12}LC/D_2O$	15.4±0.3	6.9±0.1	10.0±0.4	4.8±0.3	47±3	20±3	0.013±0.001	1.19
pH 2 IS: 160 mM	$hC_{12}LC/D_2O$	16.0±0.5	-0.4±0.1	10.5±0.4	4.5±0.3	53±4	18±3	0.013±0.001	1.25
	$dC_{12}LC/H_2O$	15.8±0.4	6.9±0.1	10.2±0.3	0.5±0.3	50±3	15±3	0.013±0.001	1.12
	$dC_{12}LC/D_2O$	15.4±0.3	6.9±0.1	10.2±0.3	4.7±0.3	47±3	20±3	0.013±0.001	1.12

In order to obtain structural parameters of the micelles of $C_{12}LC$, three contrasts (h-sample in D_2O, d-sample in H_2O and D_2O) were measured in pH 7 and 2 with

different ionic strengths. The model used was the core-shell sphere model, **Table 3.S4** shows the best fit parameters from simultaneous fitting to the three contrasts.

3.5 Neutron reflection profiles and best-fit parameters for different concentrations $dC_{12}LC$ in NRW at pH 7 and pH 2
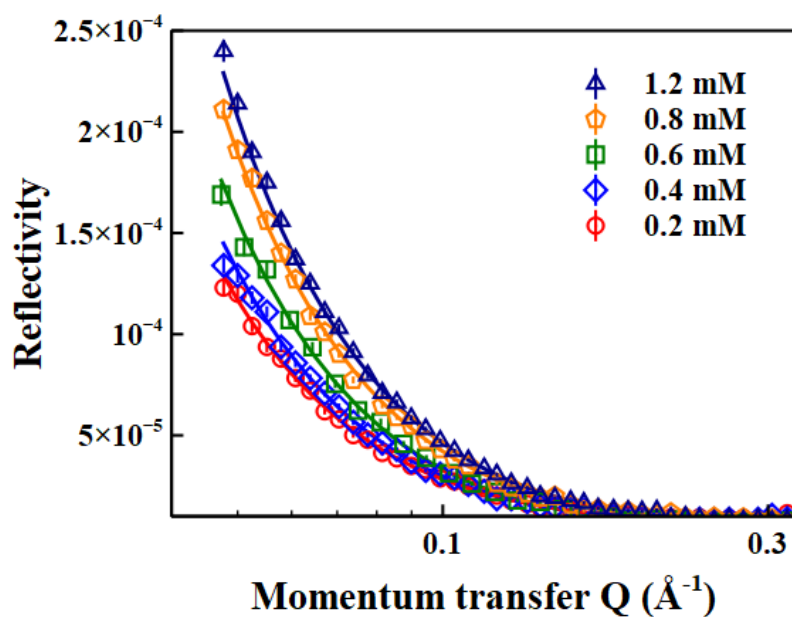
Figure 3.S3. Neutron reflectivity profiles of $dC_{12}LC$ measured in NRW at pH 7 (ionic strength:10 mM), with the data measured at the 5 concentrations below 1.2 mM as shown. Those measured at 2 mM, 2.5 mM, 3 mM, 4 mM and 10 mM are not shown because they overlap well with the data at 1.2 mM. The continuous lines are the best-fit lines for each profile.

Figure 3.S3 gives profiles of $dC_{12}LC$ in NRW with different concentrations at pH 7 with ionic strength 10 mM. It shows that the intensity increases with concentration until the CMC at 1.2 mM.
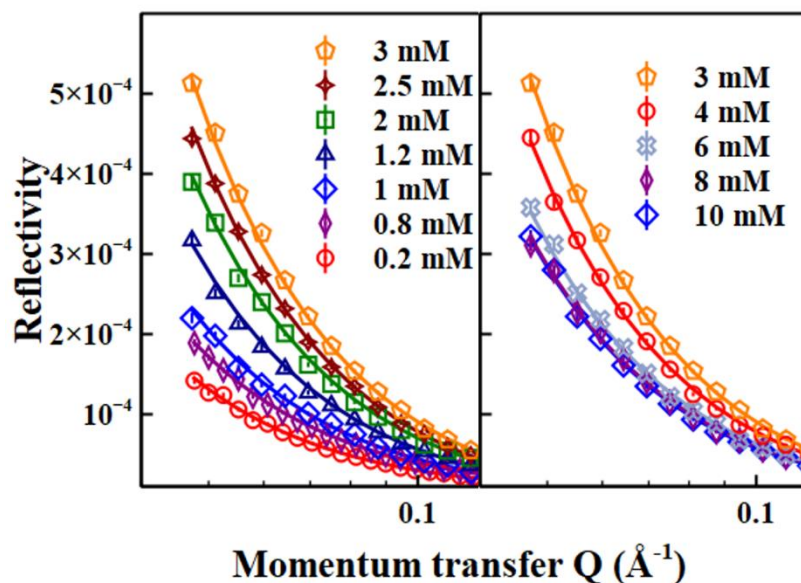
Figure 3.S4. Neutron reflectivity profiles of $dC_{12}LC$ in NRW at pH 2 (ionic strength:10 mM) with different concentrations as indicated. Continuous lines are the best-fit lines for each data.

Figure 3.S4 shows neutron reflectivity profiles of $dC_{12}LC$ in NRW at pH 2 (ionic strength: 10 mM) under different concentrations. It shows that the intensity increases with surfactant concentration below 3 mM. Over 3 mM, the intensity decreases as the surfactant concentration increases.

Table 3.S5. Best-fit parameters from the one-layer model in different concentrations from NRW runs. Surface excess and area per molecule are calculated from neutron reflection (NR) and the Gibbs equation.

pH	Concentration (mM)	Thickness ± 1 (Å)	Layer SLD ± 0.1 (Å^{-2}×10^{-6})	Γ_{NR} ± 0.2 (mol·m^{-2}×10^{-6})	A_{NR} ± 2 (Å^2)	A_{Gibbs} ± 2 (Å^2)
	0.2	18	2.3	2.7	63	62
7	0.4	19	2.4	2.9	57	54
	0.6	20	2.5	3.2	53	51

	0.8	21	2.8	3.5	48	48
	1.2	21	2.7	3.6	46	46
	2	22	2.7	3.7	45	
	2.5	22	2.6	3.7	46	
	3	22	2.7	3.6	46	
	4	22	2.6	3.6	47	
	10	22	2.6	3.6	46	
	0.2	19	2.3	2.8	60	
	0.8	21	2.6	3.3	50	
	1	22	2.7	3.7	45	
	1.2	22	3.1	4.3	39	
	2	22	3.5	4.9	34	
2	2.5	22	3.7	5.2	32	
	3	23	3.9	5.7	29	
	4	23	3.7	5.2	32	
	6	22	3.3	4.6	36	
	8	22	3.2	4.3	38	
	10	22	3.1	4.3	38	

Table 3.S5 lists the best-fit structural parameters from one-layer model fits to neutron reflectivity profiles measured from $dC_{12}LC$ adsorption in NRW at pH 7 and 2, together with surface excess and area per molecule calculated from the Gibbs equation.

3.5 Comparison of area per molecule from neutron reflection and surface tension.
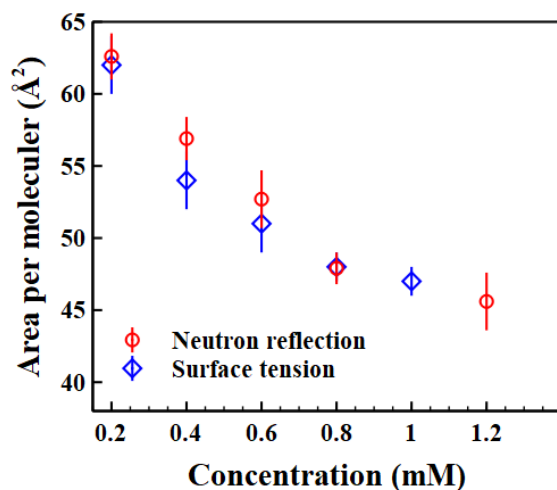
Figure 3.S5. Comparison of area per molecule plotted against concentration of $C_{12}LC$ from neutron reflection and surface tension at pH 7.

3.6 The best-fit structural parameters from the three contrasts at pH 7 and pH 2 with ionic strength of 10mM from $C_{12}LC$ layers adsorbed at the air/water interface by neutron reflection

Table 3.S6. Best-fit parameters for the two-layer model in three isotopic contrasts: $dC_{12}LC/D_2O$, $dC_{12}LC/NRW$ and $hC_{12}LC/D_2O$ in 2 mM at pH 7 and pH 2 with the ionic strength of 10 mM.

Contrasts	Layer	2 mM $C_{12}LC$ at pH 7		2 mM $C_{12}LC$ at pH 2	
		Thickness (Å)	Layer SLD ($Å^{-2} \times 10^{-6}$)	Thickness (Å)	Layer SLD ($Å^{-2} \times 10^{-6}$)
$dC_{12}LC/D_2O$	Layer in air	12.1±0.3	2.8±0.1	12.9±0.3	5.0±0.2
	Layer under water	8.8±0.2	3.7±0.3	10.0±0.7	4.7±0.2
$dC_{12}LC/NRW$	Layer in air	12.5±0.3	3.3±0.1	13.0±0.3	4.2±0.2
	Layer under water	9.0±0.3	2.0±0.2	9.7±0.3	1.9±0.2
$hC_{12}LC/D_2O$	Layer in air	12.0±0.3	-0.2±0.1	13.0±0.3	-0.2±0.1
	Layer under water	10.0±0.4	3.1±0.2	10.5±0.5	1.6±0.1
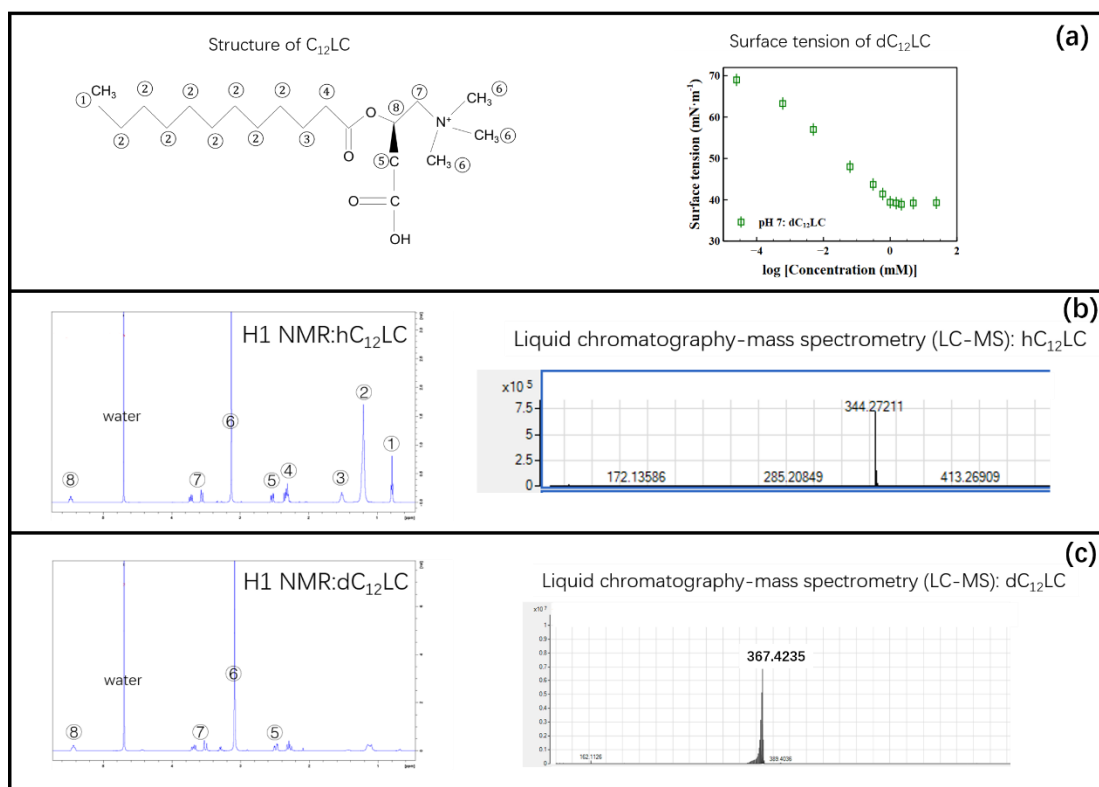
Figure 3.S6. Characterization of chain deuterated $C_{12}LC$ (a) Left: structure of $C_{12}LC$; Right: surface tension of $dC_{12}LC$. (b) Left: ^{1}H NMR of $hC_{12}LC$; Right: LC-MS of $hC_{12}LC$. (c) Left: ^{1}H NMR of $dC_{12}LC$; Right: LC-MS of $dC_{12}LC$.

4. Characterization of chain deuterated $C_{12}LC$

Figure 3.S6 shows the characterization of $dC_{12}LC$. The surface tension plot in **Figure 3.S6(a)** reveals the high purity of the purified $dC_{12}LC$. **Figure 3.S6(c)** shows the ^{1}H NMR and LC-MS of $dC_{12}LC$, in comparison with those of $hC_{12}LC$ in **Figure 3.S6(b)** the molecule weight is increased by 23 because of 23 hydrogen atoms in the lauroyl chain are deuterated. Besides, ^{1}H NMR shows the signals of hydrogen atoms in the lauroyl chain (①~④) almost vanish after deuteration.

References

[1] M. Instruments, Zetasizer Nano Series User Manual, MAN0317 1 (2004) 2004.

[2] J. Stetefeld, S.A. McKenna, T.R. Patel, Dynamic Light Scattering: A Practical Guide and Applications in Biomedical Sciences, Biophysical Reviews 8(4) (2016) 409-427.

[3] E. Pambou, J. Crewe, M. Yaseen, F.N. Padia, S. Rogers, D. Wang, H. Xu, J.R. Lu, Structural Features of Micelles of Zwitterionic Dodecyl-Phosphocholine (C(1)(2)Pc) Surfactants Studied by Small-Angle Neutron Scattering, Langmuir 31(36) (2015) 9781-9789.

[4] A.J. Jackson, Introduction to Small-Angle Neutron Scattering and Neutron Reflectometry, NIST Center for Neutron Research (2008) 1-24.

[5] J.B. Hayter, J. Penfold, An Analytic Structure Factor for Macroion Solutions, Molecular Physics 42(1) (1981) 109-118.

[6] J.-P. Hansen, J.B. Hayter, A Rescaled Msa Structure Factor for Dilute Charged Colloidal Dispersions, Molecular Physics 46(3) (1982) 651-656.

[7] E. Lucassen-Reynders, A Surface Equation of State for Mixed Surfactant Monolayers, Journal of Colloid and Interface Science 41(1) (1972) 156-167.

Chapter 4

How do acyl chain lengths of acyl-L-carnitines affect their surface adsorption and solution aggregation?

Huayang Liu[1], Ke Fa[1], Xuzhi Hu[1], Zongyi Li[1], Kun Ma[2], Mingrui Liao[1], Lin Zhang[1], Ralf Schweins[3], Armando Maestro[3], Peixun Li[2], John RP Webster[2], Jordan T. Petkov[4], Robert K. Thomas[5], Jian Ren Lu[1,*]

[1] Biological Physics Laboratory, School of Physics and Astronomy, University of Manchester, Oxford Road, Manchester, M13 9PL, UK.

[2] ISIS Neutron Facility, Rutherford Appleton Laboratory, STFC, Chilton, Didcot, Oxon OX11 0QX, UK.

[3] Institut Laue-Langevin, 71 Avenue des Martyrs, CS20156, 38042 Grenoble Cedex 9, France

[4] Arch UK Biocides Ltd, Lonza, Hexagon Tower, Delaunays Road, Blackley, Manchester M9 8ZS, UK.

[5] Physical and Theoretical Chemistry, University of Oxford, South Parks, Oxford OX1 3QZ, UK

*Author to whom correspondence should be addressed. Email: j.lu@manchester.ac.uk

Keywords: L-carnitine, Acyl chain length, carnitine surfactants, surface adsorption, solution aggregation, pH responsive

TOC

pH 7, ionic strength of 10 mM

surface adsorption
(monolayer)

$C_{12}LC$ 21.5 ± 2 Å

$C_{14}LC$ 22.6 ± 2 Å

$C_{16}LC$ 24.2 ± 2 Å

A : area per molecule

$A = 45.4 \pm 2$ Å^2 $A = 47.5 \pm 2$ Å^2 $A = 48.8 \pm 2$ Å^2

solution aggregation
(core-shell sphere)

25.9 ± 2 Å 29.5 ± 2 Å 32.8 ± 2 Å
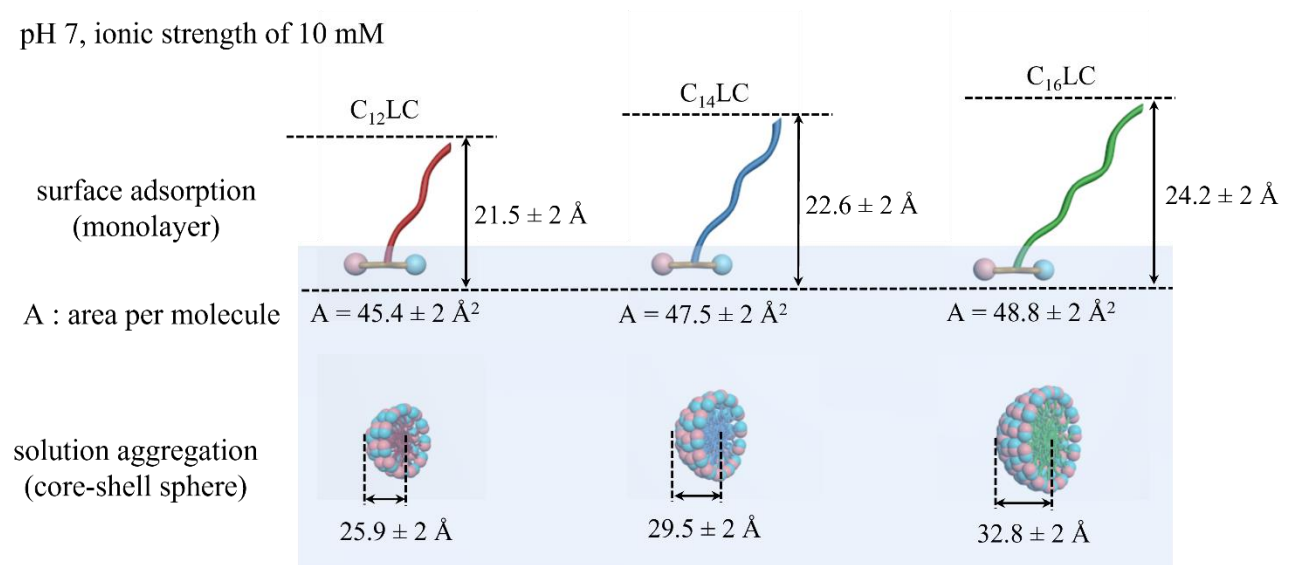
Abstract

Hypothesis: L-carnitines in our body systems can be readily converted into acyl-L-carnitines which have a prominent place in cellular energy generation by supporting the transport of long-chain fatty acids into mitochondria. Acyl-L-carnitines are biocompatible surfactants that could be explored for technological, personal care and healthcare applications. However, the lack of understanding of the effects of molecular structures on their physical properties has constrained their potential use.

Experiments: This work reports the study of the influence of the acyl chain lengths of acyl-L-carnitines (C_nLC) on solubility, surface adsorption and aggregation. Critical micellar concentrations (CMCs) of C_nLC were determined by surface tension measurements. Neutron reflection (NR) was used to further examine the structure and composition of the adsorbed C_nLC layer. The structural changes of the micellar aggregates under different concentrations of C_nLC, pH and ionic strength were determined by dynamic light scattering (DLS), and small angle neutron scattering (SANS).

Findings: $C_{12}LC$ is fully soluble over a wide temperature and concentration range. There is however a fast decline of solubility with increasing acyl chain length, with the adsorption and aggregation behavior of $C_{14}LC$ studied at 30 ^{o}C and $C_{16}LC$ at 45 ^{o}C. The solubility boundaries displayed distinct hysteresis behavior against temperature heating and cooling. The CMCs of $C_{12}LC$, $C_{14}LC$ and $C_{16}LC$ at pH 7 were 1.1 ± 0.1, 0.10 ± 0.02 and 0.010 ± 0.005 mM, respectively, with the limiting values of area per molecule at the CMC being 45.4 ± 2, 47.5 ± 2 and 48.8 ± 2 Å^2 and the thicknesses of the adsorbed C_nLC layers at air/water interface increasing from 21.5 ± 2, 22.6 ± 2 to 24.2 ± 2 Å, respectively. All three surfactants formed core-shell spherical micelles with comparable dimensional parameters apart from an increase in

core radius with acyl chain length. This study outlines the effects of acyl chain length on the physicochemical properties of C_nLCs under different environmental conditions, serving as a useful basis for developing their potential applications.

1. Introduction

Carnitine has two chiral stereoisomers, D-form and L-form, with L-carnitine being the dominant species in mammals. L-carnitine transports the fatty acids through the membrane of mitochondria in the form of acyl-L-carnitines formed via enzymatic catalysis, an essential part of the mitochondrial β-oxidation process [1-5]. This step thus is important in the generation of energy to intracellular organelles and tissues [1, 6]. L-carnitine also participates in other molecular processes including oxidation of branched chain α-keto acids, synthesis of erythropoietin on renal anemia, and amelioration of intradialytic symptoms [7-9]. Carnitine deficiency is related to many complications such as diabetes, cardiomyopathy, obesity, sepsis, and endocrine disorders [8]. In addition to endogenously synthesizing L-carnitine in liver and kidney, dietary ingestion of L-carnitine from meat products and nutrient supplies helps maintain the metabolic balance, particularly for individuals with insufficient L-carnitine synthesis. Recent studies have suggested potential roles of L-carnitine in obesity and weight control [10, 11], though other studies have also contradicted such claims [12]. However, there is a rising trend of treating L-carnitine as a heathy living supplement or as a weight-loss nutrient [13, 14].

Both alkyl and acyl-L-carnitine esters can be synthesized by connecting a hydrophobic chain with the hydroxy or carboxylic acid group of the carnitine [15]. These derivatives are natural surfactants with varied potential applications. Interesting antimicrobial effects from alkyl/acyl-L-carnitine esters against bacteria, yeasts and fungi have been reported by previous studies [15]. These surfactants have good biocompatibility, pH responses, and fluorocarbon-chain carnitines perform even better [16]. In addition, the alkyl/acyl carnitine esters with two hydrophobic chains have been reported as biocompatible cationic lipids, with potential benefits in gene delivery [17].

In spite of extensive studies reporting the biological functions of these derivatives, there is a lack of exploration of their physical properties under different molecular structures and environmental conditions. Such studies could help clarify our understanding of their behavior and support their further development into practical applications.

Acyl-L-carnitine is characterized by its L-carnitine head group (hydrophilic) and acyl chain tail (hydrophobic), both of which contribute to self-aggregation [18] and interfacial adsorption [16]. It has also been reported that the pK values and surface potentials of this series of surfactants change with the extent of ionization in the head group and electrolyte ions [18, 19]. However, there is a lack of information on the effects of environmental stimuli (e.g., pH, ionic strength) on their micellar structures and adsorbed layers at different interfaces. Following our previous study characterizing micellization and surface adsorption of lauroyl-L-carnitine (C_{12}LC) [20], this work aims to study how acyl chain length affects micellar size and shape and the layer structures adsorbed at the air/water interface using acyl-L-carnitines (C_nLC) with n = 12, 14 and 16. The self-assembled nanoaggregates and surface adsorption properties of the C_nLC series are affected by the interplay between environmental conditions and molecular structural features such as acyl chain length, which are important in their potential applications. In this work, the structures of the self-assembled nanoaggregates of C_nLC were examined by dynamic light scattering (DLS) and small angle neutron scattering (SANS) and surface properties adsorbed at the air/water interface were examined by means of surface tension and neutron reflection (NR) measurements.

2. Experimental methods

2.1. Materials

Lauroyl-L-carnitine ($C_{12}LC$, purity $\geq$ 99%), myristyl-L-carnitine ($C_{14}LC$, purity $\geq$ 99%) and palmityl-L-carnitine ($C_{16}LC$, purity $\geq$ 99%) were synthesized separately following a method provided by Lonza. Chain deuterated acyl-L-carnitines (dC_nLC, n = 12, 14, 16) with different chain length were synthesized by following a similar method to that used to synthesize the $C_{12}LC$ in our previous work [20]. Initially, TLC was used to monitor the pattern of the reaction of deuterated saturated fatty aid and excess thionyl chloride to give deuterated n-acyl chloride. With this information, the mixture of L-carnitine hydrochloride salt and trichloroacetic acid was then heated continuously for 30 min at 70 ^{o}C until it melted. This intermediate was then cooled down to 50 ^{o}C and mixed with deuterated n-acyl chloride by adding it dropwise. The solution was reheated to 70 ^{o}C under continuous stirring. After 16 hr, 1-propanol was added into the cooled system to precipitate the crude product. The intermediate crude product was filtered. Finally, the acyl-L-carnitine hydrochloride salt with deuterated chain was recrystallized from acetone.

The purification of fully protonated and chain deuterated $C_{12}LC$ has been described previously [20]. Long-chain acyl-L-carnitines ($C_{14}LC$ and $C_{16}LC$) have lower solubility in water in comparison with $C_{12}LC$. For these compounds, the acyl-L-carnitine hydrochloride salt solution was titrated with NaOH solution to neutral at 45 ^{o}C and then the water was removed by freeze-drying. The intermediate white powder was dissolved in excess ethanol (purity $\geq$ 99%). The cloudy solution was filtered to remove NaCl and then the rotary evaporator was used to remove residual ethanol to give crude neutral acyl-L-carnitines. The final samples were purified by three recrystallizations following the method for $C_{12}LC$ and characterized by LC-MS and

^{1}H NMR as shown in **Figure 4.S1** in the supporting information. The purity of C_nLC was characterized using surface tension measurements.

2.2. Dynamic light scattering (DLS)

Purified C_nLC powder was dissolved in water at different concentrations and the micellar hydrodynamic radii were determined by a Malvern Instruments Zetasizer Nano-ZS. A polystyrene cuvette ($10\times10\times45$ mm) [21] was used to hold 1 ml C_nLC solution and then measured at different temperatures after a 30 min equilibration.

DLS was also employed to detect the solubility of C_nLC in water in the temperature range of 5 - 50 ^{o}C. Solution samples were loaded in the cuvette with a cap to control solvent evaporation. During either heating or cooling, the DLS measurements were undertaken at different temperatures with step of 1 ^{o}C. At each temperature, the samples were measured every 10 min to obtain the time-resolved raw correlograms. The differences from the raw correlograms were used to monitor the transition from clear solution to 'cloudy' status or the reverse process without any further analysis.

2.3. Microscopic imaging

The appearance of insoluble material in aqueous surfactant solution was detected by a microscopic imaging (Nikon Eclipse TE2000-U Microscope, Nikon Instruments). 10 μL of sample solution was injected between two glass coverslips. The sample was fixed on the stage and cooled down to room temperature. The images of any insoluble material in the solution were captured by the software (NIS-Elements BR Microscope Imaging Software, Nikon Instruments) at different times during this process using a Nikon $10\times/0.25$ $\infty/-$ WD7.0 microscope with a 10x objective lens.

2.4. Small angle neutron scattering (SANS)

The SANS measurements were performed on the instrument LOQ at ISIS Pulsed Neutron Source and D11 at ILL. These instruments give data in the form of plots of scattering intensity of samples, I(Q), against momentum transfer, Q, where Q = $(4\pi/\lambda)\sin(\theta)$, λ is the neutron wavelength and 2θ is the scattering angle. LOQ is a time-of-flight instrument with a λ range of 2.2 - 10 Å, giving an approximate Q range from 0.01 to 0.34 Å^{-1} [22]. In D11, a neutron wavelength of 5.5 Å coupled with 2 distances between the sample and detector (1.4 and 8 m) were used to obtain a Q range of 0.01 - 0.5 Å^{-1}.

In the SANS study, the scattering length density (SLD) values of C_nLC were altered by H/D substitution in the acyl chain. Thus, three isotopic contrasts, including fully protonated acyl-L-carnitines (hC_nLC) in D_2O, chain deuterated acyl-L-carnitines (dC_nLC) in H_2O and D_2O, were measured to study the nature of the aggregation of C_nLC. Samples in D_2O buffer were loaded in quartz cells (path length: 2 mm, Type 120 Hellma GmbH) [23], and similar cells with a path length of 1 mm were used to load samples in H_2O. In this work, C_nLC samples at 20 mM were also measured at pH 7 and 2 with an ionic strength of 10 and 160 mM. These SANS runs were undertaken at 25 ℃ for $C_{12}LC$, 30 ℃ for $C_{14}LC$ and 45 ℃ for $C_{16}LC$ due to their different solubility in the aqueous solution and the temperature was controlled by a Julabo water bath. SANS data were fitted by SasView software version 4.1.2 [24] with a core-shell spherical model [25].

Hayter_msa, as a structure factor, was applied in the model to fit the interaction between charged micelles in acidic conditions [26, 27]. **Table 4.S1** lists the physical

constants and related parameters of C_nLCs. The analysis methods and relevant theories have been described fully in our previous work [20].

2.5. Surface tension measurements

The surface tension of C_nLC was measured on a tensiometer (Krüss K11) by the du Noüy ring method. The measurements were performed at 25 °C for $C_{12}LC$, 30 °C for $C_{14}LC$ and 45 °C for $C_{16}LC$. Equilibrium surface tensions were determined with at least 20 min equilibration time. A cover slip was used to prevent the evaporation of water during the measurements. The critical micelle concentrations (CMCs) were determined from the plot of surface tension against concentrations (expressed in natural logarithm). Below the CMC, amphiphilic surfactant molecules adsorb at the air/water interface, leading to a decreased surface tension with concentration. The surface tension reaches a plateau at and above the CMC, when the air/water interface is saturated with surfactant molecules. The CMC values can therefore be estimated by the break points in the surface tension plots.

2.6. Neutron reflection (NR)

NR measurements were undertaken on reflectometers FIGARO at ILL and at SURF in TS1 at the ISIS Neutron Faculty. FIGARO uses two incident angles of 0.62 and 3.8° providing a Q range of 0.0045 - 0.42 $Å^{-1}$ for the horizontal samples [28]. SURF uses the time-of-flight method, and measures each sample at incident angles of 0.35, 0.65 and 1.5°, giving the Q range of 0.01 - 0.4 $Å^{-1}$. The measurement from the surface of pure D_2O was carried out at the beginning of the experiment for calibration. The scattering length densities (SLDs) of the surfactants are also listed in **Table 4.S1**.

The surface adsorbed amounts or surface excesses of C_nLC at different concentrations were determined using the high contrast of dC_nLC in null reflecting water (NRW).

The characterization of structures of the adsorbed layers above the CMC were carried out with 3 contrasts: hC_nLC in D_2O and dC_nLC in both D_2O and NRW.

The NR profiles were fitted by the Motofit software [29, 30]. The uniform layer model was used to fit NRW measurements, and the 2-layer model consisting of the top layer in air (containing acyl chains) and the bottom layer in water (containing heads and water) was used to fit the data sets of 3 contrasts. The analysis method for the area per molecule (A) and surface excess (Γ) has been fully described in previous work [20].

3. Results and Discussion

3.1. Solubility of C_nLC in aqueous solution

Figure 4.1 shows the molecular structures of the three C_nLC surfactants (n = 12, 14 and 16). The solubility of C_nLCs in aqueous solution constitutes an important part of this part of study. When fully dissolved, the C_nLC surfactants must exist in the form of monomers over the low concentration range, but as the concentration increases micelles start to form. More elaborate nanostructures may also form via self-assembly upon further increase in concentration. However, any behavior such as aggregation or insolubility is affected by their acyl chain length and environmental conditions such as temperature (T). $C_{12}LC$ powder was found to be totally soluble over 5 - 50 °C up to 200 mM at pH 7, the highest concentration studied. In contrast, some insoluble material was observed in aqueous $C_{14}LC$ and $C_{16}LC$ systems at room temperature at concentrations well above their CMCs at pH 7 but disappeared above 45 °C. When the temperature dropped back to room temperature, the $C_{14}LC$ system remained clear whereas the insoluble substance reappeared in the $C_{16}LC$ system.
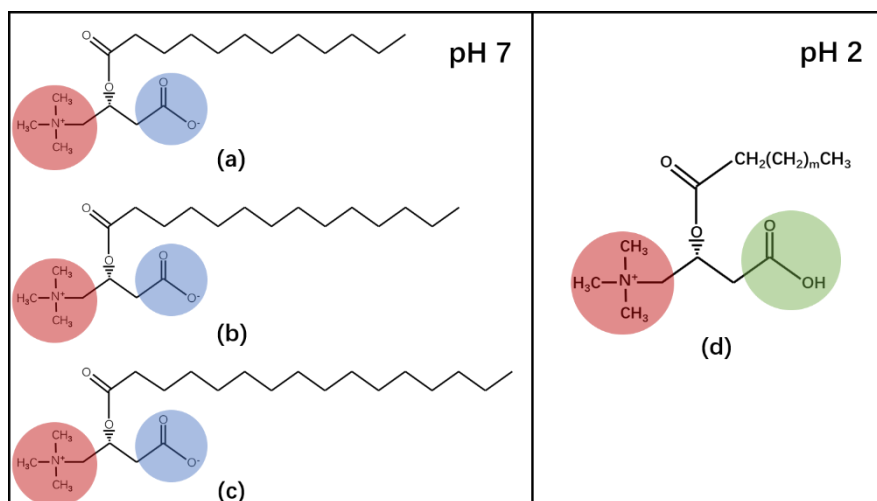
Figure 4.1. Molecular structures of zwitterionic (a) $C_{12}LC$, (b) $C_{14}LC$, (c) $C_{16}LC$ at pH 7 and cationic (d) C_nLC at pH 2 (m = 9 for $C_{12}LC$, m = 11 for $C_{14}LC$ and m = 13 for $C_{16}LC$). Red circles represent the cationic trimethyl ammonium group, blue circles represent the anionic carboxyl group and green circles represent the neutral protonated carboxyl group.

The appearance of the insoluble substance in the $C_{16}LC$ system at 200 mM upon cooling down from 48 °C to room temperature (23 - 24 °C) was further examined by optical microscopy with representative images taken at different times and shown in **Figure 4.2(a)**. No insoluble substance was observed from 48 to 40 °C. As the temperature decreased further, the insoluble substance appeared at 27 °C. Additionally, both the size and amount of the insoluble substance increased as the temperature was further lowered down. These observations point to temperature dependence of the solubility of $C_{16}LC$.

DLS was then employed to make more accurate detection of the temperature at which the insoluble substance appears/disappears. In the heating process, the temperature at which the insoluble substance disappears after 1 h equilibrium time is T_h. In the

cooling process, the temperature at which the insoluble substance appears after 1 h equilibrium time is T_c. **Figure 4.2(b)** shows the correlograms of the 200 mM $C_{16}LC$ sample with 1 h equilibrium at different temperatures upon cooling. The appearance of insoluble substance was detected at 37 °C (T_c). On the basis of the change of the correlation coefficient of the $C_{16}LC$ system, it initially took a short time to decay (**Figure 4.2(c)**) at 37 °C. After some 40 min equilibration, it took much longer time for the correlation coefficient to decay, indicating the appearance of large size particles (insoluble substance) [31]. **Figure 4.2(d)** shows that the disappearance of the insoluble substance was detected at 44 °C (T_h) in the heating process. As shown in **Figure 4.2(e)**, at 44 °C it took 50 and 60 min for the correlograms to become identical, indicating that the solution becomes clear after 50 min.
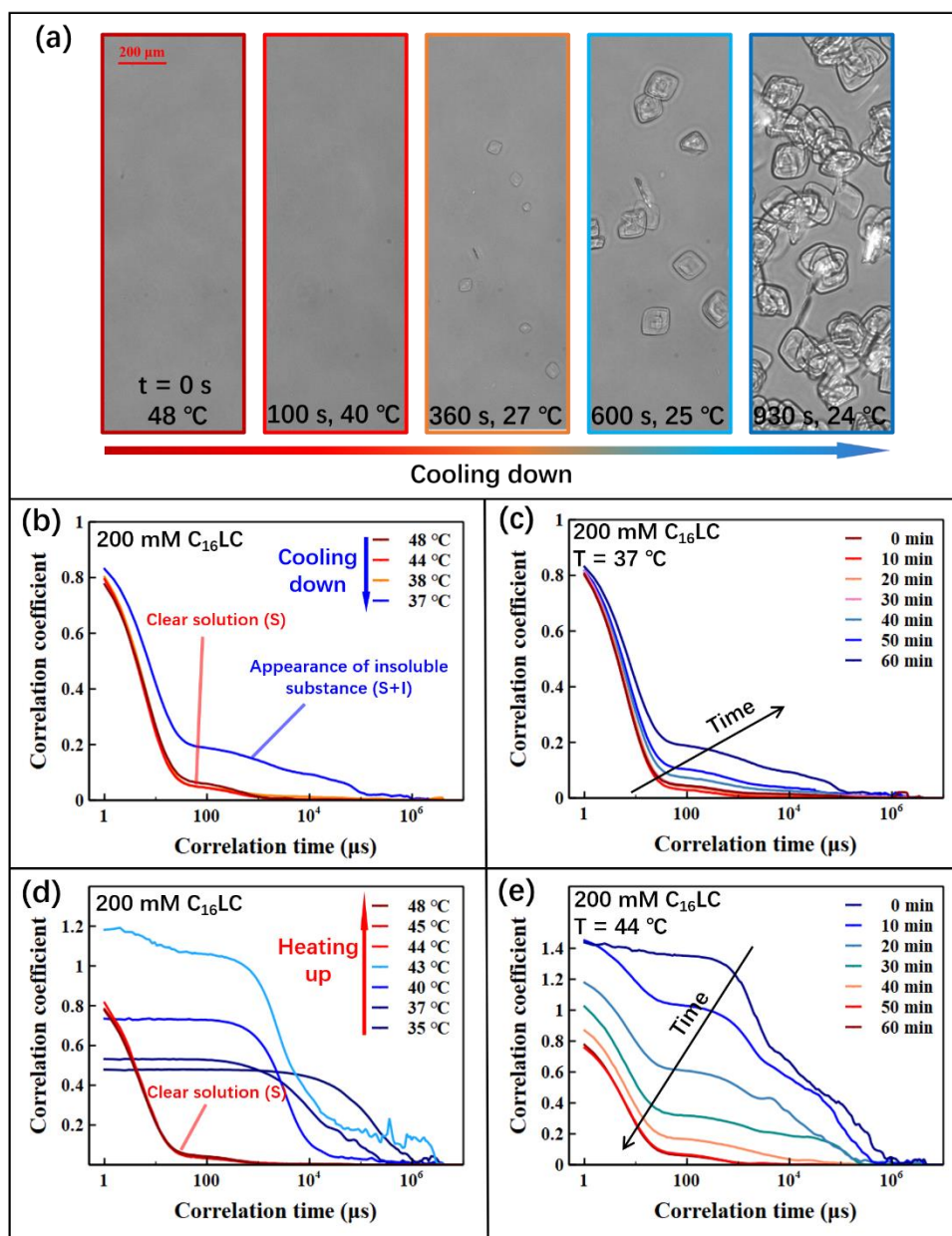
Figure 4.2. (a) The microscopic images of the aqueous $C_{16}LC$ system at 200 mM and pH 7 showing the transition from the clear aqueous system (48 ^{o}C) to the 'cloudy' system (room temperature). Time and temperature are recorded in this cooling down process. (b) The correlograms of 200 mM $C_{16}LC$ aqueous system at different temperatures with 1 h equilibrium time in the cooling process at pH 7. The insoluble substance appears at 37 ^{o}C. (c) The raw correlograms of 200 mM $C_{16}LC$ aqueous system at 37 ^{o}C and pH 7. The insoluble substance appears after 40 min. (d) The correlograms of 200 mM $C_{16}LC$ aqueous system at different temperatures with 1 h

equilibrium time in the heating process at pH 7. The insoluble substance disappears at 44 $^{\circ}$C. (e) The raw correlograms of 200 mM $C_{16}LC$ aqueous $C_{16}LC$ at 44 $^{\circ}$C and pH 7. The insoluble substance disappears after 50 min.

DLS measurements for $C_{16}LC$ at different concentrations were also undertaken following the same heating and cooling processes to determine the critical temperatures, T_h and T_c. **Figure 4.3(a)** shows that both T_h and T_c lines show a slight increase with surfactant concentration. There is a gap of 11 $^{\circ}$C at 1 mM but the gap narrows slightly with increasing surfactant concentration. This heating and cooling dependent gap represents an uncertain status of the system as marked by U in **Figure 4.3(a)**, indicating the hysteresis behavior of the surfactant system.

$C_{14}LC$ shows a similar dissolution behavior to $C_{16}LC$. **Figure 4.S2** shows the correlograms of 200 mM $C_{14}LC$ system in the heating and cooling process with T_h and T_c being 29 and 15 $^{\circ}$C, respectively. Against concentration change, $C_{14}LC$ has much lower T_h around 27 - 29 and T_c around 10 - 15 $^{\circ}$C as shown in **Figure 4.3(b)**. As indicated already, $C_{12}LC$ is fully soluble over the large T and concentration ranges, as further confirmed by DLS. Thus, the aqueous solubility of C_nLC surfactants, apart from concentration and temperature, is determined by the acyl chain length, with $C_{12}LC$ having the highest solubility followed by $C_{14}LC$ and $C_{16}LC$.

At pH 2, a $C_{12}LC$ sample remained soluble in the range of 5 to 50 $^{\circ}$C at 200 mM. However, the solubility behavior of $C_{16}LC$ and $C_{14}LC$ is more complicated. The solubilities are both significantly enhanced under acidic conditions. Thus, T_h and T_c of the 200 mM $C_{16}LC$ system decreased to 29 and 13 $^{\circ}$C respectively, whereas $C_{14}LC$ at 200 mM was totally soluble at 11 $^{\circ}$C but the insoluble substance did not reappear

when the temperature decreased to 5 °C. The change of pH from 7 to 2 protonates the carboxyl group (**Figure 4.1(d)**) leaving the head group with only the one positive charge. Protonation at pH 2 therefore enhances C_nLC dissolution more effectively than the zwitterionic head group with zero net charge at pH 7 [20].
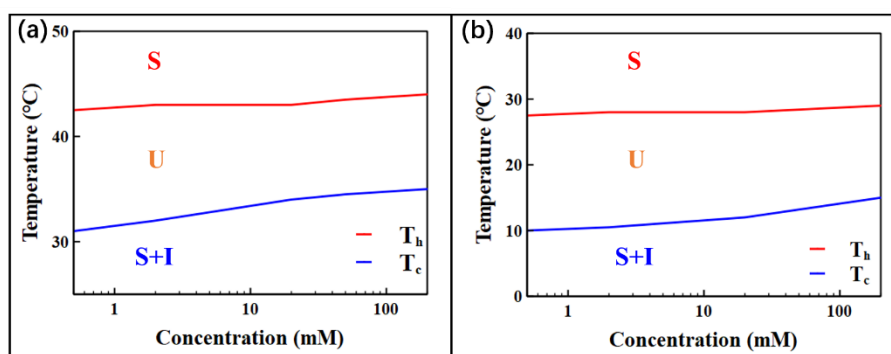
Figure 4.3. The status of $C_{16}LC$ (a) and $C_{14}LC$ (b) aqueous systems at pH 7 at different concentrations and temperatures. In the heating process from the 'cloudy' aqueous system, the samples are totally soluble (S) above T_h (red line). In the cooling process from the clear aqueous system, the insoluble substance (S + I) occurs at T_c (blue line). Between T_h and T_c the status of systems are uncertain (U), indicating hysteresis.

3.2. Effect of acyl chain length on surface tension and CMC

As shown in **Figure 4.1**, the carnitine head of the C_nLC contains a carboxyl group. At pH 7, the carboxyl group is dissociated. As the trimethyl ammonium group bears a positive charge, the L-carnitine head becomes zwitterionic. The surface tension data was measured under different concentrations for the C_nLC series (n = 12, 14 and 16) at pH 7 with the ionic strength fixed at 10 mM, as shown in **Figure 4.4**. The measurements were undertaken at 25 °C for $C_{12}LC$, 30 °C for $C_{14}LC$ and 45 °C for $C_{16}LC$ where C_nLCs are totally soluble in aqueous solution. The presence of surface

active impurity can cause a minimum around the CMC, as shown in the previous study of surface adsorption of sodium dodecyl sulphate ($C_{12}SO_4Na$), where a small amount of dodecanol was found to produce a significant minimum around its CMC [32]. The absence of such a minimum around the CMCs in **Figure 4.4** indicates that the purity of these surfactants is high. The surface tension value at the CMC (γ_{CMC}) is around 40 mN·m^{-1} for $C_{12}LC$, 39 mN·m^{-1} for $C_{14}LC$ and 40 mN·m^{-1} for $C_{16}LC$. These surface tension values above their CMCs are close to those from zwitterionic $C_{12}PC$ and $C_{14}PC$, but γ_{CMC} for $C_{16}PC$ is slightly lower, at about 38 mN/m [33]. On the other hand, those of SDS and $C_{12}TAB$ are also around 40 mN/m [34, 35], though those of the nonionic surfactants $C_{12}E_5$ and $C_{12}E_6$ are lower [36].
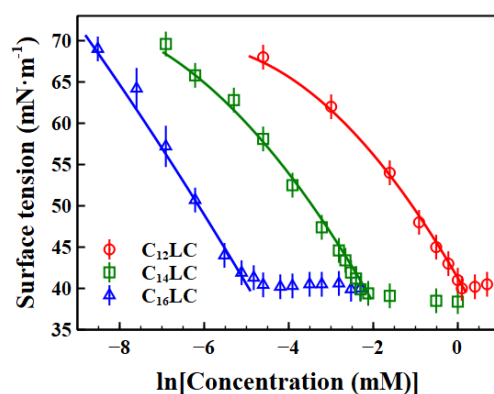
Figure 4.4. Surface tension data for $C_{12}LC$ (25 °C), $C_{14}LC$ (30 °C), and $C_{16}LC$ (45 °C) at pH 7 and an ionic strength fixed at 10 mM. Continuous lines represent the best fit with quadratic equations for the surface tension data below CMCs.

The trend of decreasing CMC with increasing alkyl or acyl chain length is expected for most surfactants. **Figure 4.4** also indicates that the CMC for $C_{12}LC$ is 1.1 ± 0.1 mM, 0.1 ± 0.02 mM for $C_{14}LC$ and 0.01 ± 0.005 mM for $C_{16}LC$, showing a sharp decrease of CMC with increasing length of acyl chain, consistent with the generally

observed pattern. **Figure 4.5** summarizes the changes of CMC for four types of surfactants, including cationic, anionic, zwitterionic and nonionic, with different chain length. The CMC values of the C_nLC series are close to the single chain phosphocholine surfactants (C_nPC) [33] but higher than C_nE_6 [37, 38] and lower than those of sodium alky sulphates (C_nSO_4Na) [39, 40] and C_nTAB [39, 41]. The logarithm of the CMC values has a linear relationship with the number of carbon atoms in the chain (n) as shown in **Figure 4.5** and described by the following equation:

$$Log\ CMC = an + b \qquad (4.1)$$

where n is the number of carbon atoms in the alkyl/acyl chain, a is the slope and b is the intercept, and the fit parameters of a and b are shown in **Table 4.S2**. **Figure 4.5** and **Table 4.S2** indicate that C_nPC and C_nLC have the same a of -0.5 which is less than -0.4 for C_nE_6 and even less than the values for C_nTAB and C_nSO_4Na (close to -0.3), showing the impact of head types. The CMCs of the charged surfactants decrease more slowly than neutral or zwitterionic surfactants as their chain length increases.
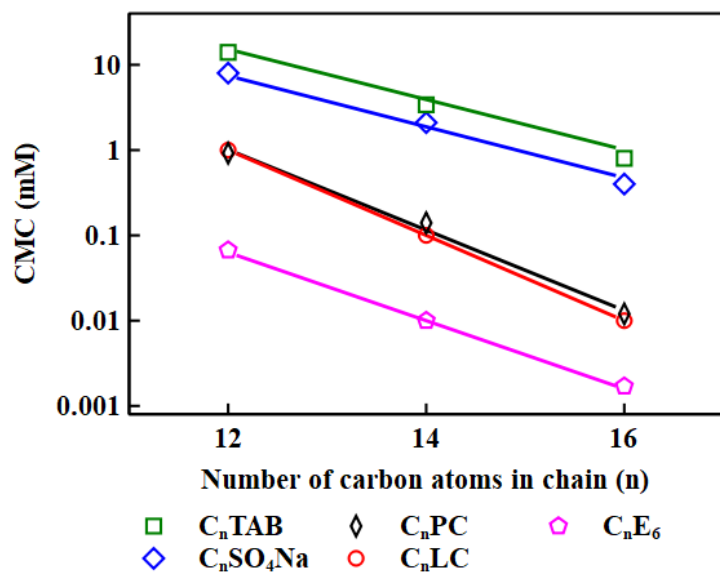
Figure 4.5. Dependence of CMCs on the number of carbon atoms in alkyl/acyl chain for cationic (C_nTAB), anionic (C_nSO_4Na), nonionic (C_nE_6) and zwitterionic surfactants (C_nLC and C_nPC).

The surface tension values below CMC are best fit as a quadratic function of ln[concentration], as shown by continuous lines in **Figure 4.4**. When combined with the Gibbs equation, which has been discussed in the previous work [20], the limiting areas at the CMC (A_{CMC}) are 46 ± 2 Å^2 for $C_{12}LC$, 48 ± 2 Å^2 for $C_{14}LC$ and 49 ± 2 Å^2 for $C_{16}LC$, respectively. **Table 4.1** summaries the A_{CMC} values of C_nLC, C_nTAB, C_nSO_4Na, C_nE_6 and C_nPC with different chain lengths in aqueous solution. Within 3 - 5 Å^2, these A_{CMC} values are consistent with the chain lengths and the different head types. A_{CMC} of C_nLCs slightly increases as the acyl chain length increases, but this change is well within the experimental error. The same trend is seen from other surfactants, especially for C_nPC except that their average A_{CMC} values are about 5 Å^2 greater. $C_{12}LC$ occupies a smaller area than $C_{12}TAB$, $C_{12}SO_4Na$ and $C_{12}PC$ but its A_{CMC} is close to $C_{12}E_5$ and $C_{12}E_6$, at about 45 Å^2 [42]. This trend becomes less obvious when comparing A_{CMC} of $C_{14}LC$ to those from other surfactants listed in

Table 4.1. In contrast, A_{CMC} for $C_{16}LC$ is slightly larger than $C_{16}TAB$, but smaller than $C_{16}PC$ and $C_{16}SO_4Na$, showing a larger range of variation. Thus, whilst A_{CMC} for $C_{12}LC$ is consistently smaller, A_{CMC} values for $C_{14}LC$ and $C_{16}LC$ are closer to other surfactants with the same chain length.

Table 4.1: A_{CMC} values of C_nLC, C_nTAB, C_nSO_4Na, C_nE_6 and C_nPC with C_{12}-, C_{14}- and C_{16}-chains.

Surfactants	$A_{CMC} \pm 2$ (Å^2)			Ref.
C_nLC	$C_{12}LC$	$C_{14}LC$	$C_{16}LC$	
	46	48	49	This work
C_nTAB	$C_{12}TAB$	$C_{14}TAB$	$C_{16}TAB$	
	50	48	45	[43-45]
C_nSO_4Na	$C_{12}SO_4Na$	$C_{14}SO_4Na$	$C_{16}SO_4Na$	
	48	51	56	[35, 46, 47]
C_nPC	$C_{12}PC$	$C_{14}PC$	$C_{16}PC$	
	53	50	54	[33]

3.3. Effect of pH and ionic strength on surface tension and CMC

Surface tension measurements were also undertaken at pH 7 and 2 with ionic strengths of 10 and 160 mM which is close to that of physiological fluids such as human blood, as shown in **Figure 4.S3**. The results show that at pH 7 the surface tensions and CMCs of C_nLC are little affected by ionic strength, consistent with the zwitterionic nature of all C_nLC surfactants as shown in **Figure 4.1**. This feature is the same as the behavior of zwitterionic C_nPC and nonionic $C_{12}E_6$.

At pH 2, the carboxyl groups of C_nLC are almost fully protonated as indicated in **Figure 4.1(d)**, and the surfactants become net cationic. As the pH is reduced to acid, however, the surfactants may be slowly hydrolysed to the original organic acids and L-carnitine. As demonstrated in our previous work, at pH 2, the hydrolysis of $C_{12}LC$ appears to lead to a pronounced surface tension minimum around the CMC (**Figure**

4.S3(a)), which is a result of competitive adsorption of traces of lauric acid generated by such hydrolysis. It is then interesting that we observe no surface tension minima from $C_{14}LC$ and $C_{16}LC$ at pH 2, although some hydrolysis might be expected. In principle, the shifts in CMC of the carnitines, the shift in solubility of the corresponding acid, and the shifts in surface tension should approximately scale with each other, so that the hydrolysis effects observed at pH 2 for $C_{12}LC$ should also occur for the two longer chain carnitines. The one important difference is that the concentration range is reaching the point where depletion effects may become significant. For materials such as the fatty acids and alcohols the measurement of the true surface tension becomes very difficult at low solubilities. This is because material is lost to other surfaces, and by evaporation, to an extent that the equilibrium surface tension cannot easily be measured [48]. There seems to be no reason why the rates of hydrolysis to the larger chain carnitines should be different from $C_{12}LC$ but if the absolute rates of loss of their acids to other surfaces are unchanged, the fractional loss would then be significantly higher and might prevent the adsorption of the fatty acid reaching its true equilibrium.

At pH 2, increased ionic strength to 160 mM further screens the repulsive interaction between cationic C_nLC molecules, leading to two effects. First, the surface tension is increased compared with that at pH 2 at an ionic strength of 10 mM. Second, the CMCs of $C_{14}LC$ and $C_{16}LC$ drop further to 0.08 and 0.009 mM. These effects from salt addition are in accordance with similar impact on ionic surfactants such as $C_{12}SO_4Na$ and DTAB [49], making ionic surfactants effectively more surface active in their competitive adsorption against their respective long chain organic acids.

Table 4.2: CMC and γ_{CMC} values of C_nLC at pH 7 and 2 with the ionic strengths of 10 and 160 mM.

	pH 7			
Ionic strength	10 mM		160 mM	
Surfactant	CMC (mM)	γ_{CMC} ± 1 (mN·m^{-1})	CMC (mM)	γ_{CMC} ± 1 (mN·m^{-1})
$C_{12}LC$	1.1 ± 0.1	40	1.1 ± 0.1	40
$C_{14}LC$	0.10 ± 0.02	39	0.10 ± 0.02	40
$C_{16}LC$	0.010 ± 0.005	40	0.010 ± 0.005	40
	pH 2			
Ionic strength	10 mM		160 mM	
Surfactant	CMC (mM)	γ_{CMC} ± 1 (mN·m^{-1})	CMC (mM)	γ_{CMC} ± 1 (mN·m^{-1})
$C_{12}LC$	-	-	-	-
$C_{14}LC$	0.30 ± 0.05	37	0.08 ± 0.02	38
$C_{16}LC$	0.040 ± 0.010	37	0.009 ± 0.005	38

3.4. Solution aggregation at different concentrations and temperatures.

The hydrodynamic radii of micelles of C_nLCs with different acyl chains were examined by DLS. **Table S3** lists the measurements of hydrodynamic radii of C_nLC aggregates at pH 7 with an ionic strength of 10 mM at different temperatures and C_nLC concentrations. $C_{12}LC$ was measured at 10 ºC (20 mM), 25 ºC (5, 20 and 80 mM) and 40 ºC (20 mM) and the data at 25 ºC and 20 mM are consistent with our previous work [20]. As $C_{14}LC$ and $C_{16}LC$ have lower solubility than $C_{12}LC$, $C_{14}LC$ was measured at 30 ºC (5, 10 and 20 mM) and 40 ºC (20 mM) and $C_{16}LC$ was measured at 45 ºC (1, 5, 10 and 20 mM) and 55 ºC (20 mM). The radius of $C_{12}LC$ aggregates is 25 ± 2 Å, that of $C_{14}LC$ is 28 ± 2 Å and that of $C_{16}LC$ is 32 ± 2 Å. It is evident that longer acyl chain produces larger size C_nLC aggregates. However, changes in C_nLC concentration and temperature have little effect on the size of C_nLC aggregates. DLS can only describe the size of C_nLC aggregates by assuming a spherical aggregate. However, the DLS data is a useful preliminary for SANS measurements.

SANS measurements were undertaken at the same conditions as in the DLS studies. The resulting scattering intensity profiles give more precise information about the shape and inner structures of the micellar aggregates. For each selected solution condition, the SANS measurements were made under three contrasts, hC_nLC in D_2O, dC_nLC in H_2O and D_2O. The data in **Figure 4.6(a)** provide a direct comparison between the three C_nLC micellar structures in D_2O at 20 mM and pH 7. The micelles of the longer-acyl-chain C_nLC produce stronger neutron intensity and have larger sizes. Three sets of the three contrasts for $C_{12}LC$, $C_{14}LC$ and $C_{16}LC$ at 20 mM, pH 7 and the ionic strength of 10 mM are exemplified in **Figure 4.6(b)(c)(d)**. These SANS profiles are best fit by the core-shell spherical model, shown by continuous lines in **Figure 4.6**, with best-fit parameters summarized in **Table 4.3**. The good fit to the measured data indicates that all micelles from the three C_nLC are close to the core-shell sphere model and that the core radius increases as the acyl chain becomes longer. The core radii of the micelles are 15.6 Å for $C_{12}LC$, 18.1 Å for $C_{14}LC$ and 20.5 Å for $C_{16}LC$. The thicknesses of the shells increase slightly with acyl chain length, with the value of 10.3 Å for $C_{12}LC$, 11.4 Å for $C_{14}LC$ and 12.3 Å for $C_{16}LC$. These values together with the micellar radii give the total radius of micelles of 25.9 ± 2 Å for $C_{12}LC$, 29.5 ± 2 Å for $C_{14}LC$ and 32.8 ± 2 Å for $C_{16}LC$, consistent with the DLS data within experimental error.

The aggregation number per micelle could be calculated from the volumes of the core-shell micelles, surfactant tail and head based on **equations (4.S1)-(4.S5)**. **Table 4.S1** lists the scattering length, volume and SLD for the tails and head of the C_nLC molecules. The aggregation number of the C_nLC micelles was found to be 50 for $C_{12}LC$, 66 for $C_{14}LC$ and 83 for $C_{16}LC$, showing a steady increase in the micellar size with acyl chain length but no change at the different pH and ionic strengths studied.
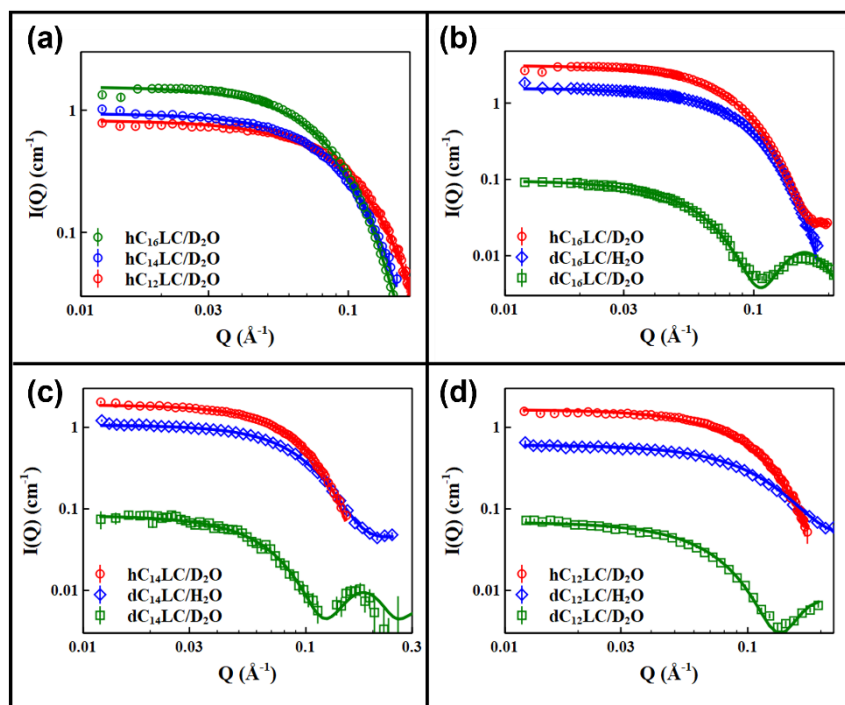
Figure 4.6. (a) The SANS profiles measured from hC$_n$LC in D$_2$O at pH 7 and 20 mM with ionic strength, IS (10 mM). Intensity is shown as a function of momentum transfer (Q). The SANS profiles of 20 mM C$_n$LC with three contrasts (hC$_n$LC in D$_2$O, dC$_n$LC in H$_2$O and D$_2$O) of (b) C$_{16}$LC (c) C$_{14}$LC (d) C$_{12}$LC (hC$_n$LC/D$_2$O has been shifted vertically by the multiplying factor 2 for better visualization)

Table 4.3: The best-fit parameters for 20 mM C$_n$LC micelles at pH 7 and pH 2 with an ionic strength of 10 mM determined from the core-shell spherical model, with further details from fits of the three isotopic contrasts of hC$_n$LC in D$_2$O, dC$_n$LC in H$_2$O and D$_2$O listed in **Table 4.S4**.

Surfactant	pH	Ionic strength (mM)	Core radius ± 2 (Å)	Shell thickness ± 2 (Å)	Aggregation number	Micelle charge ± 5
C$_{12}$LC	7	10	16	10	50 ± 3	0
	2	10	16	11	50 ± 3	18
C$_{14}$LC	7	10	18	11	66 ± 4	0
	2	10	18	11	69 ± 4	18
C$_{16}$LC	7	10	21	12	83 ± 5	0
	2	10	21	12	85 ± 5	24

3.5. Solution aggregation under different pH and ionic strength.

Following the measurements at pH 7 at an ionic strength of 10 mM, further SANS runs were made at pH 7 at ionic strengths of 160 mM for the three C_nLCs to explore the effect of ionic strength on the micellar structure. SANS measurements at pH 2 were also made at the two ionic strengths. As explained previously, three isotopic contrasts involving hC_nLC in D_2O, dC_nLC in H_2O and D_2O were used for each surfactant and the whole sets of scattering profiles are shown in **Figure 4.S4**. These SANS data show that the positively charged micelles retain the core-shell spherical structures at pH 2 but have strong repulsive interaction at low ionic strength. At this pH the head group will carry a positive charge caused by the protonation of the carboxyl group as shown in **Figure 4.1(d)**. **Table 4.3** lists the main structural parameters, indicating the transition of the zwitterionic C_nLC core-shell spherical micelles (zero surface charge) at pH 7 to cationic micelles in the acidic environment due to the protonation of the carboxyl group on the L-carnitine head. When the pH decreases to 2, the size of the micelles does not change and the total radius of the core-shell spherical micelles becomes 26.4 ± 2 Å for $C_{12}LC$, 29.4 ± 2 Å for $C_{14}LC$ and 32.5 ± 2 Å for $C_{16}LC$, consistent with the structural parameters observed at pH 7 when the micelles are in the zwitterionic form. The micellar charge number of C_nLC increases to 18 for $C_{12}LC$, 18 for $C_{14}LC$ and 24 for $C_{16}LC$, leading to strong electrostatic repulsion between positively charged micelles at this pH and at the low ionic strength of 10 mM. **Figure 4.7** shows the aggregation number and charge number of the C_nLC micelles at pH 2, showing a clear increase of both parameters with acyl chain length. Interestingly, the fractional charge per $C_{12}LC$ in the micelle is about 0.36 whilst that for the $C_{14}LC$ and $C_{16}LC$ micelles is about 0.28. The difference might arise from the packing of the L-carnitine head groups which affects the condensation of counterions.
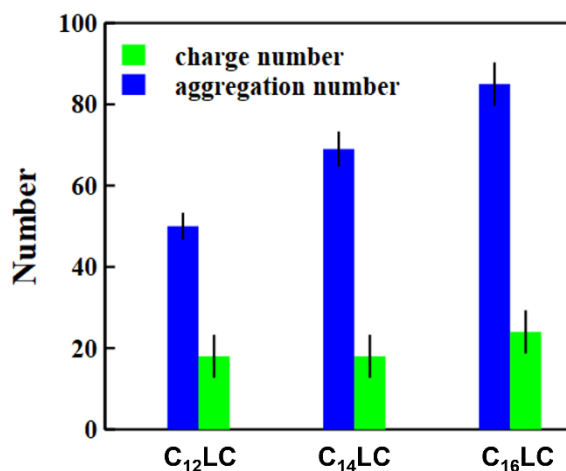
Figure 4.7. The aggregation and charge number per micelle of $C_{12}LC$, $C_{14}LC$ and $C_{16}LC$, giving the fraction of charge per aggregated surfactant at 0.36, 0.26 and 0.28, respectively.

SANS data at pH 7 and pH 2 in the presence of 160 mM ionic strength are shown in **Figure 4.S4** with the best-fit parameters listed in **Table 4.S4**, indicating that increase of ionic strength to 160 mM has little effect on the size and charge number of the micelles at pH 7 and 2. The difference between SANS profiles at pH 2 in the presence of ionic strengths of 10 or 160 mM indicates a different interaction between cationic micelles. A high ionic strength at low pH results in weaker interaction because of electrostatic screening. The Debye length was reduced by the presence of Na^+ and Cl^- close to the C_nLC micellar surfaces, as discussed previously [20]. Thus, the repulsive interaction between the C_nLC micelles at pH 2 can be reduced by electrostatic shielding as the ionic strength increases.

3.6. Surface adsorption studied by NR

Neutron reflection measurements were carried out for the three C_nLC surfactants to study the impact of concentration and acyl chain length on surface adsorption. The NR measurements of the chain deuterated C_nLCs were undertaken in NRW covering $0.2 \times$, $0.6 \times$ and $2 \times$ CMC at pH 7 with an ionic strength of 10 mM, as shown in **Figure 4.8(a)**. The neutron reflectivity in NRW arises entirely from the adsorbed layer and its level increases as the surfactant concentration increases. Additionally, the reflectivity from the C_nLC layers increases with the acyl chain length, indicating an overall increase in the amount in the adsorbed layer.

NR profiles in **Figure 4.8(a)** were fitted with a uniform layer model, with the best-fit parameters listed in **Table 4.4**. The thickness of the adsorbed layer of a specific C_nLC increases as its concentration rises. Furthermore, the thickness values are higher with longer acyl chain at the same concentration level. Notably, at $2 \times$ CMC, the thickness values of the adsorbed layer are 21.5 Å, 22.6 Å and 24.2 Å for C12LC, C14LC and C16LC, respectively. As described in our previous work [20], the A and Γ can be calculated from the following equations:

$$A = \frac{v_s \rho_s}{\tau \rho_l} \tag{4.2}$$

$$\Gamma = \frac{1}{A N_a} \tag{4.3}$$

where v_s is the volume of the surfactant molecule, ρ_s and ρ_l denote the SLD of the surfactant and adsorbed layer, τ represents the thickness of the adsorbed layer in NRW and N_a represents the Avogadro number. The calculated results are listed in **Table 4.4**, **Figure 4.8(b)** shows changes in Γ and A for the three C_nLCs at $2 \times$ CMC where the adsorption reaches a plateau. The surface excess in $\mu mol/m^2$ decreases slightly with acyl chain length increasing, whereas the area per molecule shows a small increase, with calculated *As* of 45.4 $Å^2$, 47.5 $Å^2$ and 48.8 $Å^2$ for $C_{12}LC$, $C_{14}LC$

and $C_{16}LC$, respectively. Compared with the limiting area determined from surface tension by the Gibbs equation shown in **Table 4.1**, the results from the two independent measurements are consistent. These data show that when the surface excesses are converted from $\mu mol \cdot m^{-2}$ to $mg \cdot m^{-2}$, the surface adsorbed amount increases slightly with the acyl chain length increase as shown in the inset in **Figure 4.7(b)**. This observation also indicates that the reflected signal is higher from C_nLC layer with longer acyl chain at their $2 \times$ CMCs as shown in **Figure 4.7(a)**.

The structures of the saturated layers of C_nLC at $2 \times$ CMC with three contrasts (hC_nLC in D_2O, dC_nLC in D_2O and NRW) were examined by neutron reflection. The neutron reflectivity profiles measured under different contrasts are shown in **Figure 4.S5**. These data were fitted with the best two-layer model, with the top layer containing the acyl chain in air and the bottom layer containing the entire head groups immersed in water, as schematically illustrated in **Figure 4.8(c)**. The best-fit parameters are listed in **Table 4.S5**. The thicknesses of the acyl chain layer (τ_1) and headgroup layer (τ_2) rise slightly as the acyl chain length increases. The τ_1 values are 12.2 ± 2 Å, 13.2 ± 2 Å and 13.8 ± 2 Å for $C_{12}LC$, $C_{14}LC$ and $C_{16}LC$, respectively. Notably, **Figure 4.8(c)** shows that the acyl chains tilt from the surface normal direction, and the angle of tilt (θ) from the vertical direction can be obtained by using the following equation:

$$\cos(\theta) = \frac{\tau_1}{\tau_e} \tag{4.4}$$

where τ_e is the extended full length of the acyl chain listed in **Table 4.S1**. At $2 \times$ CMC, θ was found to be $38°$ from the vertical direction for lauroyl chain, $43°$ for myristoyl chain and $48°$ for palmitoyl chain as shown in **Figure 4.8(c)**, indicating that the longer acyl chain becomes less vertical. The tilt angles are smaller than those for zwitterionic phosphocholine surfactants, which are $40°$ for $C_{12}PC$, $48°$ for $C_{14}PC$ and $53°$ for $C_{16}PC$ [50]. Additionally, they are much smaller than C_{12}betaine with $60°$ and

C_{12}TAB with 54° [51]. The thicknesses of the headgroup (τ_2) are 9.0 ± 2 Å, 9.5 ± 2 Å and 10.1 ± 2 Å for C_{12}LC, C_{14}LC and C_{16}LC, respectively. The numbers of water molecules (n_w) associated with the L-carnitine head group for the three C_nLC surfactants were calculated to be around 6 ± 2 (C_{12}LC), 8 ± 2 (C_{14}LC) and 10 ± 2 (C_{16}LC) by using the volumes of the water molecule and head group listed in **Table 4.S1**. These values are lower than those of C_{12}PC (n_w = 15) and $C_{12}E_5$ (n_w = 10).

The neutron reflectivity profiles for the three dC_nLC in NRW were also measured over the same concentration range at pH 2 and the resultant reflectivity data shown in **Figure 4.S6**. The best-fit parameters from the uniform layer model are summarized in **Table 4.S6**. Notably, as shown in **Table 4.S6**, at the same concentrations the thicknesses of the C_nLC layers show little difference to those obtained at pH 7. However, the surface excesses of the adsorbed C_nLC layers at pH 2 increase to 4.93 ± 0.30 μmol·m^{-2} for C_{12}LC at 2 mM, 3.78 ± 0.30 μmol·m^{-2} for C_{14}LC at 0.2 mM and 3.43 ± 0.30 μmol·m^{-2} for C_{16}LC at 0.02 mM with concurrent decreases in area per molecule to 33.6 ± 2, 43.8 ± 2 and 48.3 ± 2 Å^2, respectively. As illustrated in **Figure 4.1(d)**, once the zwitterionic C_nLC molecules become cationic they have a strong repulsion due to electrostatic interaction at pH 2. Thus, the arrangement of the C_nLC molecules is different from the horizontal alignment of the head group at pH 7. The strong repulsive interaction between the head groups leads to a zig-zag arrangement to satisfy the maximal distance between the cationic head groups, resulting in an effectively lower area occupied by each cationic C_nLC molecule.

Table 4.4: The best-fit parameters from the uniform layer model for chain deuterated $C_{12}LC$, $C_{14}LC$ and $C_{16}LC$ adsorbed at the air/water interface in NRW at pH 7 with the ionic strength of 10 mM and concentrations of 0.2 ×, 0.6 × and 2 × CMC. Γ and A were calculated from equations (4.2) and (4.3).

Surfactant	Conc n (mM)	Thickness ± 2 (Å)	Layer SLD ± 0.2 ($Å^{-2} \times 10^{-6}$)	Γ ± 0.30 ($\mu mol \cdot m^{-2}$)	Γ ± 0.10 ($mg \cdot m^{-2}$)	A ± 2 ($Å^2$)
$C_{12}LC$	0.2	18	2.3	2.60	0.89	64
	0.6	20	2.5	3.10	1.06	54
	2	22	2.7	3.62	1.24	46
$C_{14}LC$	0.02	19	2.5	2.56	0.95	65
	0.06	20	2.8	3.10	1.15	54
	0.2	23	2.8	3.50	1.30	48
$C_{16}LC$	0.002	19	2.7	2.50	1.00	66
	0.006	20	2.8	2.84	1.13	58
	0.02	24	2.9	3.33	1.33	49
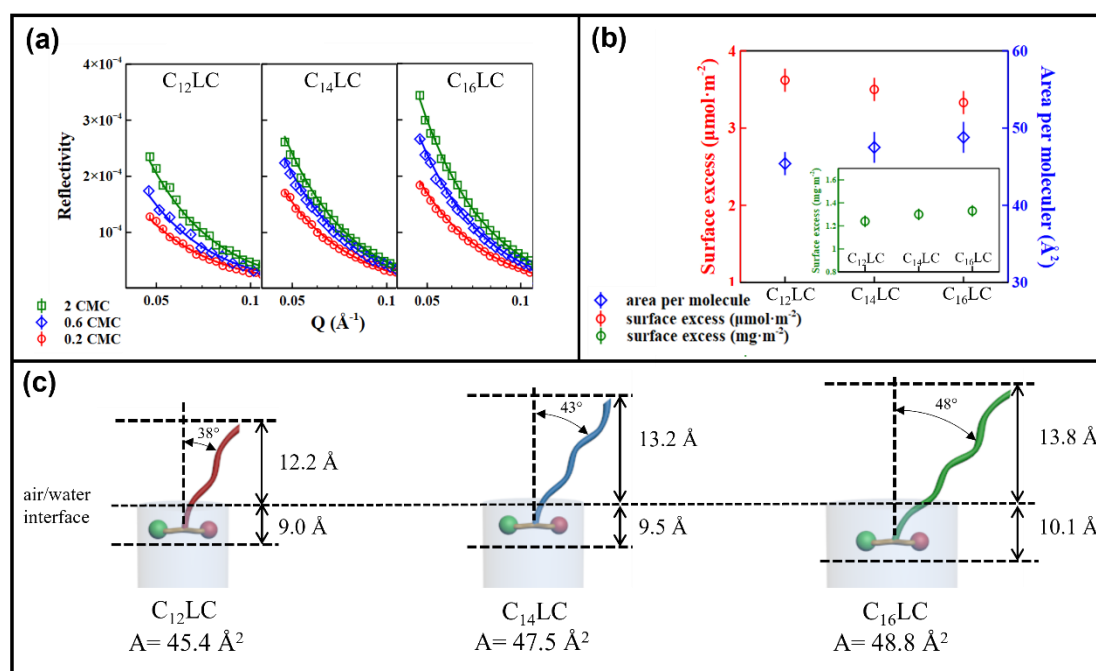
Figure 4.8. (a) Neutron reflectivity profiles of chain deuterated $C_{12}LC$, $C_{14}LC$ and $C_{16}LC$ molecules adsorbed at the air/water interface in NRW with concentrations of 0.2 ×, 0.6 × and 2 × CMC at pH 7. Reflectivity is plotted as a function of

perpendicular momentum transfer. (b) Surface excess ($\mu mol \cdot m^{-2}$) and area per molecule for $C_{12}LC$, $C_{14}LC$ and $C_{16}LC$ at $2 \times CMC$ and pH 7. The inset shows the corresponding surface adsorbed amount expressed in $mg \cdot m^{-2}$. (c) Schematic illustrations of average molecular conformation of $C_{12}LC$, $C_{14}LC$ and $C_{16}LC$ adsorbed on the surface of water at $2 \times CMC$ at pH 7 as indicated from the measured structural parameters.

4. Conclusion

Following our previous work on $C_{12}LC$ where we found a pH-dependent hydrolysis and a large surface tension minimum at acidic pH [20], the current study shows that the two longer chain acyl-carnitines follow a much more normal pattern to surface tension behavior. With the increase of the acyl chain length, however, these surfactants interact with each other more strongly and even become insoluble. Thus, while the aqueous $C_{12}LC$ system remains fully soluble, $C_{14}LC$ and $C_{16}LC$ are only soluble at elevated T ranges, marked by T_h of 27 - 29 °C and 42 - 44 °C during heating and T_c of 10 - 15 °C and 31 - 35 °C during cooling, respectively, with some minor increase of T_h and T_c with C_nLC (n = 14, 16) concentration. The gaps between T_h and T_c indicate uncertain solution status complicated by hysteresis associated with the appearance/disappearance of the insoluble phase. However, their solubility is significantly improved in an acidic environment.

The CMCs of C_nLCs were determined from surface tension to be 1.1 ± 0.1, 0.10 ± 0.02, and 0.010 ± 0.005 mM for $C_{12}LC$, $C_{14}LC$ and $C_{16}LC$ at pH 7, respectively. These values are close to zwitterionic C_nPC, lower than those of ionic surfactants such as C_nTAB and C_nSO_4Na, but higher than those of the nonionic surfactants such as C_nE_6. At pH 2, all C_nLC surfactants become cationic and their CMCs increase.

However, their CMCs decrease back to those at pH 7 with the addition of salt in acidic environments.

Both surface tension measurements and NR have shown the area per molecule above CMC to be between 46 and 49 $Å^2$ for the C_nLC series, which is about 5 - 6 $Å^2$ smaller than the values for C_nPC (n=12, 14, 16) [50]. Furthermore, these adsorbed layers are 21 - 24 Å thick, suggesting that the acyl chains become more tilted away from the surface normal, with the average tilt angle increasing from 38 to 48°. Decrease in pH from 7 to 2 does not alter layer thickness but leads to different head group packing as a result of the adjustment in packing caused by the net positive charge of the head group, consistent with increased surface adsorbed amount.

SANS intensity profiles measured under different isotopic contrasts showed that all C_nLC micelles could be modelled into core-shell spheres, with shell thicknesses about 11 ± 2 Å and core radii of 15 ± 2 Å for $C_{12}LC$, 18 ± 2 Å for $C_{14}LC$ and 21 ± 2 Å for $C_{16}LC$, showing a clear trend of core radius increase with acyl chain length, consistent with their aggregation numbers of 50 ± 3, 66 ± 4 and 83 ± 5. Surface charge number increased with decreasing pH but was less affected by acyl chain length; at pH 2 the fraction of charge per aggregated surface is about 0.36 for $C_{12}LC$ and 0.26 - 0.28 for $C_{14}LC$ and $C_{16}LC$. The electrostatic repulsion could be screened by adding salt, but salt addition did not affect micellar size and shape. Future work will examine how the different structural features from this series of biosurfactants affect their antimicrobial actions and cytotoxicity under physiological conditions.

Acknowledgments

Supporting Information

Further data in characterization of $h/dC_{14}LC$ and $h/dC_{16}LC$, correlograms of $C_{14}LC$, surface tension plots of C_nLC under pH 7 and 2 with two different ionic strength, DLS data for C_nLC micelles, SANS profiles and fitted parameters for C_nLC under pH 7 (IS: 160 mM) and pH 2 (IS: 10 and 160 mM), NR profiles and fitted parameters for C_nLC at pH 7 and 2. Supporting data are available on request from the corresponding author.

References

[1] A.M. Evans, G. Fornasini, Pharmacokinetics of L-Carnitine, Clinical Pharmacokinetics 42(11) (2003) 941-967.

[2] F. Celik, M. Kose, M. Yilmazer, G.N. Köken, D.T. Arioz, M. Kanat Pektas, Plasma L-Carnitine Levels of Obese and Non-Obese Polycystic Ovary Syndrome Patients, Journal of Obstetrics and Gynaecology 37(4) (2017) 476-479.

[3] K. Salic, E. Gart, F. Seidel, L. Verschuren, M. Caspers, W. van Duyvenvoorde, K.E. Wong, J. Keijer, I. Bobeldijk-Pastorova, P.Y. Wielinga, Combined Treatment with L-Carnitine and Nicotinamide Riboside Improves Hepatic Metabolism and Attenuates Obesity and Liver Steatosis, International Journal of Molecular Sciences 20(18) (2019) 4359.

[4] Y.-S. Cha, Effects of L-Carnitine on Obesity, Diabetes, and as an Ergogenic Aid, Asia Pacific Journal of Clinical Nutrition 17 (2008) 306-308.

[5] M. Pooyandjoo, M. Nouhi, S. Shab-Bidar, K. Djafarian, A. Olyaeemanesh, The Effect of (L-) Carnitine on Weight Loss in Adults: A Systematic Review and Meta-Analysis of Randomized Controlled Trials, Obesity Reviews 17(10) (2016) 970-976.

[6] S. Center, J. Harte, D. Watrous, A. Reynolds, T. Watson, P. Markwell, D. Millington, P. Wood, A. Yeager, H. Erb, The Clinical and Metabolic Effects of Rapid

Weight Loss in Obese Pet Cats and the Influence of Supplemental Oral L-Carnitine, Journal of Veterinary Internal Medicine 14(6) (2000) 598-608.

[7] A.G. Engel, C. Rebouche, Carnitine Metabolism and Inborn Errors, Journal of Inherited Metabolic Disease 7(1) (1984) 38-43.

[8] J.L. Flanagan, P.A. Simmons, J. Vehige, M.D. Willcox, Q. Garrett, Role of Carnitine in Disease, Nutrition & metabolism 7(1) (2010) 1-14.

[9] G. Guarnieri, Carnitine in Maintenance Hemodialysis Patients, Journal of Renal Nutrition 25(2) (2015) 169-175.

[10] A. Jeukendrup, R. Randell, Fat Burners: Nutrition Supplements That Increase Fat Metabolism, Obesity Reviews 12(10) (2011) 841-851.

[11] B.T. Wall, F.B. Stephens, D. Constantin-Teodosiu, K. Marimuthu, I.A. Macdonald, P.L. Greenhaff, Chronic Oral Ingestion of L-Carnitine and Carbohydrate Increases Muscle Carnitine Content and Alters Muscle Fuel Metabolism During Exercise in Humans, The Journal of Physiology 589(4) (2011) 963-973.

[12] R.G. Villani, J. Gannon, M. Self, P.A. Rich, L-Carnitine Supplementation Combined with Aerobic Training Does Not Promote Weight Loss in Moderately Obese Women, International Journal Of Sport Nutrition And Exercise Metabolism 10(2) (2000) 199-207.

[13] D. Rucker, R. Padwal, S.K. Li, C. Curioni, D.C. Lau, Long Term Pharmacotherapy for Obesity and Overweight: Updated Meta-Analysis, Bmj 335(7631) (2007) 1194-1199.

[14] R. Padwal, S. Li, D. Lau, Long-Term Pharmacotherapy for Overweight and Obesity: A Systematic Review and Meta-Analysis of Randomized Controlled Trials, International Journal of Obesity 27(12) (2003) 1437-1446.

[15] M. Calvani, L. Critelli, G. Gallo, F. Giorgi, G. Gramiccioli, M. Santaniello, N. Scafetta, M.O. Tinti, F. De Angelis, L-Carnitine Esters as "Soft", Broad-Spectrum Antimicrobial Amphiphiles, Journal of Medicinal Chemistry 41(13) (1998) 2227-2233.

[16] J. Nivet, M. Le Blanc, J. Riess, Synthesis and Preliminary Evaluation of Perfluoroalkylacyl Carnitines as Surfactants for Biomedical Use, European Journal of Medicinal Chemistry 26(9) (1991) 953-960.

[17] J. Wang, X. Guo, Y. Xu, L. Barron, F.C. Szoka, Synthesis and Characterization of Long Chain Alkyl Acyl Carnitine Esters. Potentially Biodegradable Cationic Lipids for Use in Gene Delivery, Journal of Medicinal Chemistry 41(13) (1998) 2207-2215.

[18] S.H. Yalkowsky, G. Zografi, Some Micellar Properties of Long-Chain Acylcarnitines, Journal of Colloid and Interface Science 34(4) (1970) 525-533.

[19] S.H. Yalkowsky, G. Zografi, Potentiometric Titration of Monomeric and Micellar Acylcarnitines, Journal of Pharmaceutical Sciences 59(6) (1970) 798-802.

[20] H. Liu, X. Hu, Z. Li, K. Fa, H. Gong, K. Ma, M. Liao, P. Li, J.R. Webster, J.T. Petkov, R.K. Thomas, J.R. Lu, Surface Adsorption and Solution Aggregation of a

Novel Lauroyl-L-Carnitine Surfactant, Journal of Colloid and Interface Science 591 (2021) 106-114.

[21] X. Hu, H. Gong, Z. Li, S. Ruane, H. Liu, E. Pambou, C. Bawn, S. King, K. Ma, P. Li, What Happens When Pesticides Are Solubilized in Nonionic Surfactant Micelles, Journal of Colloid and Interface Science 541 (2019) 175-182.

[22] R. Heenan, J. Penfold, S. King, Sans at Pulsed Neutron Sources: Present and Future Prospects, Journal of Applied Crystallography 30(6) (1997) 1140-1147.

[23] X. Hu, H. Gong, Z. Li, S. Ruane, H. Liu, P. Hollowell, E. Pambou, C. Bawn, S. King, S. Rogers, How Does Solubilisation of Plant Waxes into Nonionic Surfactant Micelles Affect Pesticide Release?, Journal of Colloid and Interface Science 556 (2019) 650-657.

[24] X. Hu, H. Gong, P. Hollowell, M. Liao, Z. Li, S. Ruane, H. Liu, E. Pambou, N. Mahmoudi, R.M. Dalgliesh, J.R. Lu, What Happens When Pesticides Are Solubilised in Binary Ionic/Zwitterionic-Nonionic Mixed Micelles?, Journal of Colloid and Interface Science 586 (2021) 190-199.

[25] J.B. Hayter, J. Penfold, Determination of Micelle Structure and Charge by Neutron Small-Angle Scattering, Colloid and Polymer Science 261(12) (1983) 1022-1030.

[26] J.B. Hayter, J. Penfold, An Analytic Structure Factor for Macroion Solutions, Molecular Physics 42(1) (1981) 109-118.

[27] J.-P. Hansen, J.B. Hayter, A Rescaled Msa Structure Factor for Dilute Charged Colloidal Dispersions, Molecular Physics 46(3) (1982) 651-656.

[28] R. Campbell, H. Wacklin, I. Sutton, R. Cubitt, G. Fragneto, Figaro: The New Horizontal Neutron Reflectometer at the Ill, The European Physical Journal Plus 126(11) (2011) 1-22.

[29] A. Nelson, Co-Refinement of Multiple-Contrast Neutron/X-Ray Reflectivity Data Using Motofit, Journal of Applied Crystallography 39(2) (2006) 273-276.

[30] X. Hu, E. Pambou, H. Gong, M. Liao, P. Hollowell, H. Liu, W. Wang, C. Bawn, J. Cooper, M. Campana, K. Ma, P. Li, J.R.P. Webster, F. Padia, G. Bell, J.R. Lu, How Does Substrate Hydrophobicity Affect the Morphological Features of Reconstituted Wax Films and Their Interactions with Nonionic Surfactant and Pesticide?, Journal of Colloid and Interface Science 575 (2020) 245-253.

[31] S. Falke, C. Betzel, Dynamic Light Scattering (Dls), Radiation in Bioanalysis, Springer (2019) 173-193.

[32] J.R. Lu, I.P. Purcell, E.M. Lee, E.A. Simister, R.K. Thomas, A.R. Rennie, J. Penfold, The Composition and Structure of Sodium Dodecyl Sulfate-Dodecanol Mixtures Adsorbed at the Air-Water Interface: A Neutron Reflection Study, Journal of Colloid and Interface Science 174(2) (1995) 441-455.

[33] M. Yaseen, J. Lu, J. Webster, J. Penfold, Adsorption of Single Chain Zwitterionic Phosphocholine Surfactants: Effects of Length of Alkyl Chain and Head Group Linker, Biophysical Chemistry 117(3) (2005) 263-273.

[34] A. Espert, R.v. Klitzing, P. Poulin, A. Colin, R. Zana, D. Langevin, Behavior of Soap Films Stabilized by a Cationic Dimeric Surfactant, Langmuir 14(15) (1998) 4251-4260.

[35] J.R. Lu, A. Marrocco, T.J. Su, R.K. Thomas, J. Penfold, Adsorption of Dodecyl Sulfate Surfactants with Monovalent Metal Counterions at the Air-Water Interface Studied by Neutron Reflection and Surface Tension, Journal of Colloid and Interface Science 158(2) (1993) 303-316.

[36] J. Lu, Z. Li, R. Thomas, B. Binks, D. Crichton, P. Fletcher, J. McNab, J. Penfold, The Structure of Monododecyl Pentaethylene Glycol Monolayers with and without Added Dodecane at the Air/Solution Interface: A Neutron Reflection Study, The Journal of Physical Chemistry B 102(30) (1998) 5785-5793.

[37] F. Portet, P. Desbene, C. Treiner, Adsorption Isotherms at a Silica/Water Interface of the Oligomers of Polydispersed Nonionic Surfactants of the Alkylpolyoxyethylated Series, Journal of Colloid and Interface Science 194(2) (1997) 379-391.

[38] F.N. Padia, M. Yaseen, B. Gore, S. Rogers, G. Bell, J.R. Lu, Influence of Molecular Structure on the Size, Shape, and Nanostructure of Nonionic C N E M Surfactant Micelles, The Journal of Physical Chemistry B 118(1) (2014) 179-188.

[39] I.J. Lin, L. Marszall, Cmc, Hlb, and Effective Chain Length of Surface-Active Anionic and Cationic Substances Containing Oxyethylene Groups, Journal of Colloid and Interface Science 57(1) (1976) 85-93.

[40] A. Trawińska, E. Hallmann, K. Mędrzycka, The Effect of Alkyl Chain Length on Synergistic Effects in Micellization and Surface Tension Reduction in Nonionic Gemini (S-10) and Anionic Surfactants Mixtures, Colloids and Surfaces A: Physicochemical and Engineering Aspects 506 (2016) 114-126.

[41] S.P. Moulik, M.E. Haque, P.K. Jana, A.R. Das, Micellar Properties of Cationic Surfactants in Pure and Mixed States, The Journal of Physical Chemistry 100(2) (1996) 701-708.

[42] C. Smith, J.R. Lu, I.M. Tucker, D. Grainger, P. Li, J.R. Webster, R.K. Thomas, Temperature Resistant Binary Sles/Nonionic Surfactant Mixtures at the Air/Water Interface, Langmuir 34(32) (2018) 9442-9452.

[43] J. Lu, E. Simister, R. Thomas, J. Penfold, Adsorption of Alkyltrimethyl Ammonium Bromide at the Air-Water Interface, Trends in Colloid and Interface Science VII (1993) 92-97.

[44] J.R. Lu, Z.X. Li, J. Smallwood, R.K. Thomas, J. Penfold, Detailed Structure of the Hydrocarbon Chain in a Surfactant Monolayer at the Air/Water Interface: Neutron Reflection from Hexadecyltrimethylammonium Bromide, The Journal of Physical Chemistry 99(20) (1995) 8233-8243.

[45] J.R. Lu, Z.X. Li, R.K. Thomas, J. Penfold, Structure of Hydrocarbon Chains in Surfactant Monolayers at the Air/Water Interface: Neutron Reflection from Dodecyl Trimethylammonium Bromide, Journal of the Chemical Society, Faraday Transactions 92(3) (1996) 403-408.

[46] M. Koshinuma, T. Sasaki, Activity Measurement and Colloid Chemical Studies of Aqueous Sodium Tetradecyl Sulfate Solutions, Bulletin of the Chemical Society of Japan 48(10) (1975) 2755-2759.

[47] A. Zdziennicka, K. Szymczyk, J. Krawczyk, B. Jańczuk, Activity and Thermodynamic Parameters of Some Surfactants Adsorption at the Water–Air Interface, Fluid Phase Equilibria 318 (2012) 25-33.

[48] S.H. Myrick, E.I. Franses, Effect of Chain Length on Equilibrium and Dynamic Surface Tension of Spread Monolayers of Aqueous Alcohols, Colloids and Surfaces A: Physicochemical and Engineering Aspects 143(2-3) (1998) 503-515.

[49] F. Pan, Z. Li, H. Gong, J.T. Petkov, J.R. Lu, Membrane-Lytic Actions of Sulphonated Methyl Ester Surfactants and Implications to Bactericidal Effect and Cytotoxicity, Journal of Colloid and Interface Science 531 (2018) 18-27.

[50] M. Yaseen, J.R. Lu, J.R.P. Webster, J. Penfold, The Structure of Zwitterionic Phosphocholine Surfactant Monolayers, Langmuir 22(13) (2006) 5825-5832.

[51] D.J. Lyttle, J.R. Lu, T.J. Su, R.K. Thomas, J. Penfold, Structure of a Dodecyltrimethylammonium Bromide Layer at the Air/Water Interface Determined by Neutron Reflection: Comparison of the Monolayer Structure of Cationic Surfactants with Different Chain Lengths, Langmuir 11(3) (1995) 1001-1008.

Supporting information

How do acyl chain lengths of acyl-L-carnitines affect their surface adsorption and solution aggregation?

Huayang Liu[1], Ke Fa[1], Xuzhi Hu[1], Zongyi Li[1], Kun Ma[2], Mingrui Liao[1], Lin Zhang[1], Ralf Schweins[2], Armando Maestro[2], Peixun Li[3], John RP Webster[3], Jordan T. Petkov[4], Robert K. Thomas[5], Jian Ren Lu[1,*]

[1] Biological Physics Laboratory, School of Physics and Astronomy, University of Manchester, Oxford Road, Manchester, M13 9PL, UK.

[2] Institut Laue-Langevin, 71 Avenue des Martyrs, CS20156, 38042 Grenoble Cedex 9, France

[3] ISIS Neutron Facility, Rutherford Appleton Laboratory, STFC, Chilton, Didcot, Oxon OX11 0QX, UK.

[4] Arch UK Biocides Ltd, Lonza, Hexagon Tower, Delaunays Road, Blackley, Manchester M9 8ZS, UK.

[5] Physical and Theoretical Chemistry, University of Oxford, South Parks, Oxford OX1 3QZ, UK

*Author to whom correspondence should be addressed. Email: j.lu@manchester.ac.uk

Section A: Characterizations of h/d $C_{14}LC$ and $C_{16}LC$ from LC-MS and ^1H NMR and correlograms of $C_{16}LC$ aqueous solution and solubility of $C_{14}LC$ in aqueous solution.
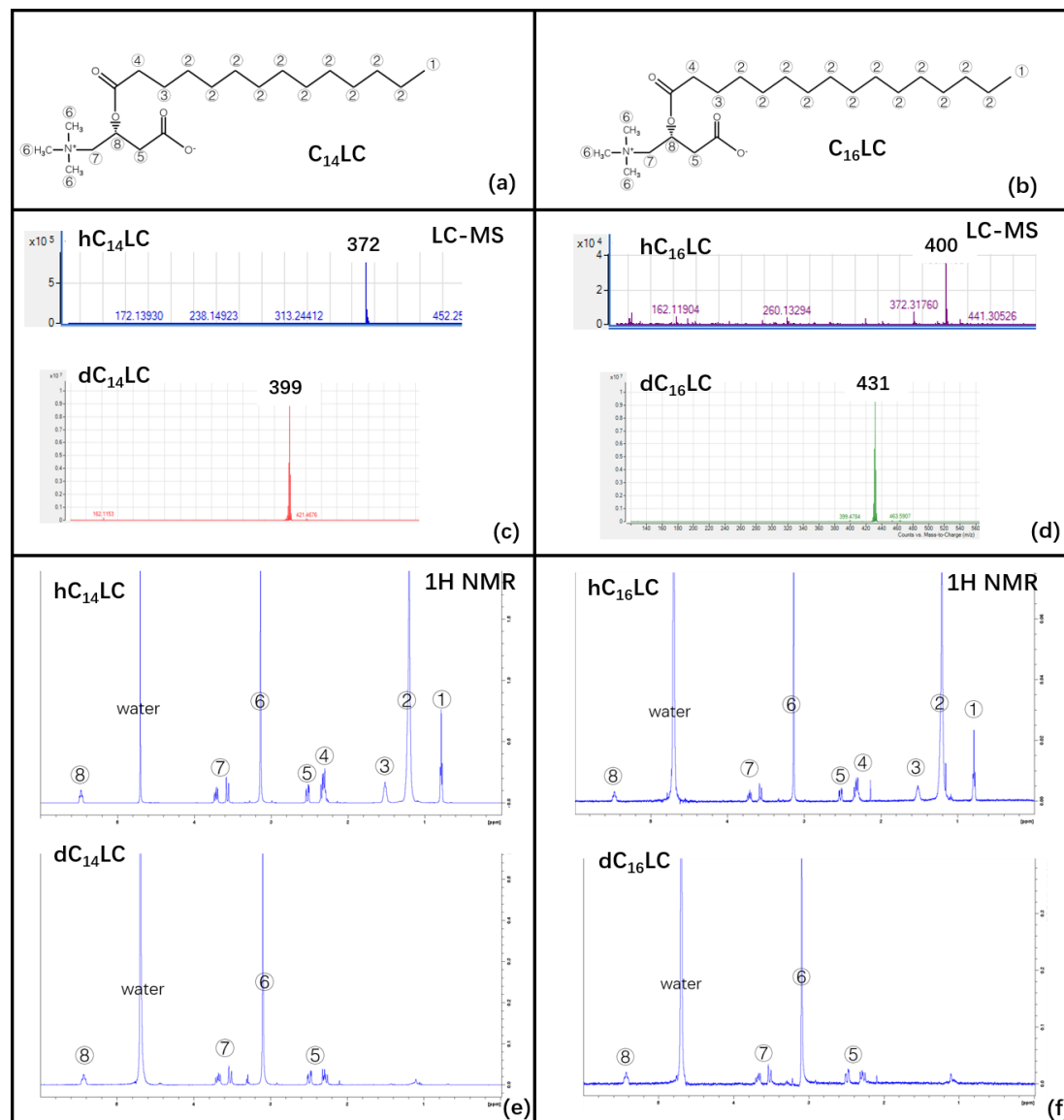
Figure 4.S1. Characterizations of $hC_{14}LC$, $dC_{14}LC$, $hC_{16}LC$ and $dC_{16}LC$. Chemical structures of $C_{14}LC$ (a) and $C_{16}LC$ (b). LC-MS of $hC_{14}LC$ and $dC_{14}LC$ (c), LC-MS of $hC_{16}LC$ and $dC_{16}LC$ (d), ^1H NMR of $hC_{14}LC$ and $dC_{14}LC$ (e) and ^1H NMR of $hC_{16}LC$ and $dC_{16}LC$ (f).
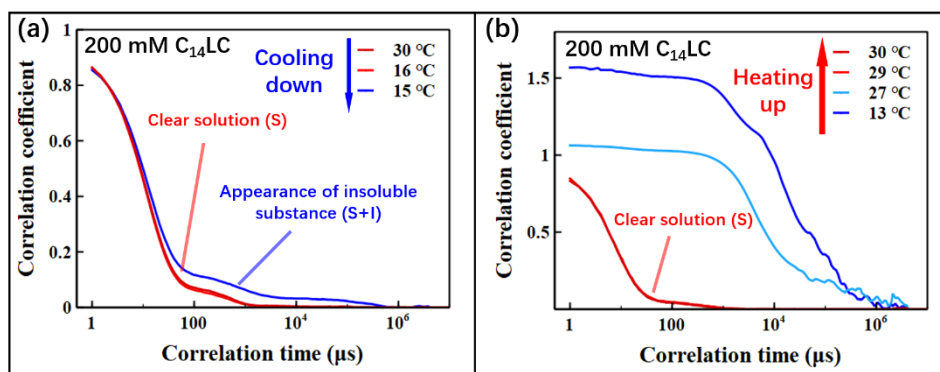
Figure 4.S2. (a) The intensity correlation function of 200 mM aqueous $C_{14}LC$ system at different temperatures with 1 h equilibrium time in the cooling process at pH 7. The insoluble substance appeared at 15 °C. (b) The intensity correlation function of 200 mM aqueous $C_{14}LC$ system at different temperatures with 1h equilibrium time in the heating process at pH 7. The insoluble substance disappeared at 29 °C.

Section B: Parameters of C_nLC molecules and calculations for the volumes of tail, head, core, and shell of C_nLC micelles.

Table 4.S1. The parameters of acyl-L-carnitines used in data analysis for neutron experiments (SANS and NR).

Segments	Extended length, τ_e (Å)	Scattering Length, b (Å×10⁻⁵)	Volume, V (Å³)	Scattering length density, ρ (Å⁻² ×10⁻⁶)
Protonanted tail ($C_{11}H_{23}$)	15.4	-12.9	323	-0.40
Deuterated tail ($C_{11}D_{23}$, 98%D)	15.4	226.5	323	7.01
Protonanted tail ($C_{13}H_{27}$)	18.0	-14.6	377	-0.38
Deuterated tail ($C_{13}D_{27}$, 98%D)	18.0	266.5	377	7.06
Protonanted tail ($C_{15}H_{31}$)	20.5	-16.3	430	-0.38
Deuterated tail ($C_{15}D_{31}$, 98%D)	20.5	306.5	430	7.13
Head(hL-carnitine with -C=O)		33.4	255	1.31
H_2O		-1.7	30	-0.56

D_2O		19.1	30	6.35

$$V_{tail} = 27.4 + 26.9 n_c \qquad (4.S1)$$

$$V_{head} = V_{C_{12}LC} - V_{tail} \qquad (4.S2)$$

$$V_{micelle} = \frac{4}{3}\pi r_{total}^3 \qquad (4.S3)$$

$$V_{core} = \frac{4}{3}\pi r_{core}^3 \qquad (4.S4)$$

$$V_{shell} = V_{micelle} - V_{core} \qquad (4.S5)$$

The volume of tail is determined by a function of the number of carbon as shown in equation (4.S1) expressed by Tanford [1].

Section C: Fitted parameters of equation (4.1) for surfactants in **Figure 4.3** and surface tension plots for C_nLC at pH 7 and 2 with different ionic strength (10 and 160 mM).

Table 4.S2. The fitted parameters of equation (4.1) for 5 types of surfactants.

	C_nLC	C_nPC	C_nE_6	C_nTAB	Sodium alky sulfates
a	-0.5	-0.5	-0.4	-0.3	-0.3
b	6.0	5.7	3.6	4.7	4.5
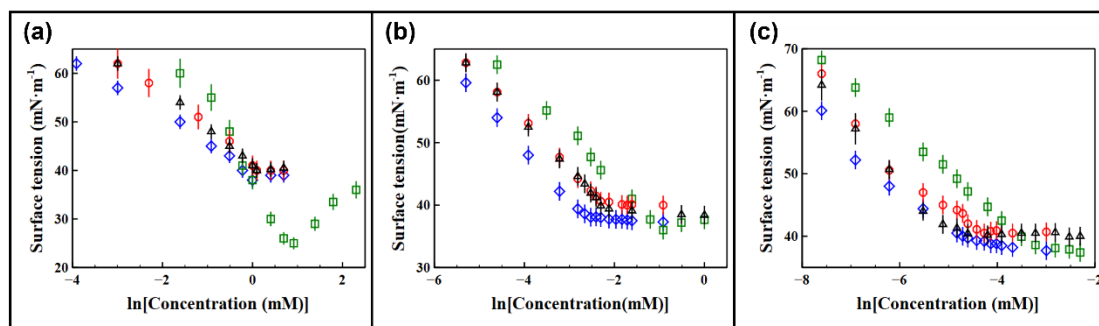
Figure 4.S3. Surface tension measured at different concentrations, pH and ionic strength: pH 7 with ionic strength (IS) : 10 mM (black triangles), pH 7 with IS : 160 mM (red circles), pH 2 with IS : 10 mM (green squares) and pH 2 with IS : 160 mM (blue diamonds) for (a) $C_{12}LC$ at 25 °C, consistent with previous work [2], (b) $C_{14}LC$ at 30 °C and (c) $C_{16}LC$ at 45 °C. The surface tension data is plotted against ln[concentration (mM)]

Section D: DLS, SANS profiles and SANS best fit parameters for C_nLC micelles.

Table 4.S3. Dynamic light scattering for C_nLC ($C_{12}LC$, $C_{14}LC$ and $C_{16}LC$) in different concentrations and temperatures at pH 7 with ionic strength (10 mM)

Surfactant,Concentration and Temperature	Hydrodynamic Radius from DLS
$C_{12}LC$, 5 mM, 25 ºC	24±2 Å
$C_{12}LC$, 20 mM, 25 ºC	25±2 Å
$C_{12}LC$, 80 mM, 25 ºC	25±2 Å
$C_{12}LC$, 20 mM, 10 ºC	24±2 Å
$C_{12}LC$, 20 mM, 40 ºC	25±2 Å
$C_{14}LC$, 5 mM, 30 ºC	27±2 Å
$C_{14}LC$, 10 mM, 30 ºC	27±2 Å
$C_{14}LC$, 20 mM, 30 ºC	28±2 Å
$C_{14}LC$, 20 mM, 40 ºC	28±2 Å
$C_{16}LC$, 1 mM, 45 ºC	29±2 Å
$C_{16}LC$, 5 mM, 45 ºC	31±2 Å
$C_{16}LC$, 10 mM, 45 ºC	32±2 Å
$C_{16}LC$, 20 mM, 45 ºC	32±2 Å
$C_{16}LC$, 20 mM, 55 ºC	32±2 Å

Table 4.S4. The best-fit structural parameters from three contrasts using the core-shell charged model for the $C_{12}LC$, $C_{14}LC$ and $C_{16}LC$ micelles at 20 mM under different pH and ionic strength. $C_{12}LC$ is measured at 25 ºC, $C_{14}LC$ is measured at 30 ºC and $C_{16}LC$ is measured at 45 ºC. The error is calculated from the fitting software SasView.

pH/ Ionic strength	Contrasts	Core radius ± 2 (Å)	ρ_{core} ± 0.1 (Å^{-2} ×10^{-6})	Shell thickness ± 2 (Å)	ρ_{shell} ± 0.3 (Å^{-2} ×10^{-6})	N_{agg}	N_{charge}	Volume fraction	χ_R^2
pH7 IS:10m M	h$C_{12}LC$/D_2O	16	-0.4	10	4.3	49±2	0	0.013±0.001	1.28
	d$C_{12}LC$/H_2O	16	7.0	10	0.3	53±3	0	0.013±0.001	1.59
	d$C_{12}LC$/D_2O	15	7.0	11	5.0	46±3	0	0.013±0.001	3.66
pH 7 IS:160m M	h$C_{12}LC$/D_2O	15	-0.4	11	4.5	48±3	0	0.013±0.001	1.62
	d$C_{12}LC$/H_2O	16	7.0	11	0.1	49±3	0	0.013±0.001	2.33
	d$C_{12}LC$/D_2O	16	6.9	10	4.9	52±3	0	0.013±0.001	4.02
pH 2 IS:10m	h$C_{12}LC$/D_2O	16	-0.4	11	4.5	52±3	19±5	0.013±0.001	2.16
	d$C_{12}LC$/H_2O	16	7.0	11	0.3	51±3	16±5	0.013±0.001	2.47

M	$dC_{12}LC/D_2O$	16	7.0	11	5.0	49±3	18±5	0.013±0.001	1.77
pH 2	$hC_{12}LC/D_2O$	16	-0.4	10	4.3	50±4	19±5	0.013±0.001	1.79
IS:160m	$dC_{12}LC/H_2O$	16	7.0	11	0.5	49±3	16±5	0.013±0.001	1.92
M	$dC_{12}LC/D_2O$	15	6.9	10	4.8	44±3	18±5	0.013±0.001	2.81
pH7	$hC_{14}LC/D_2O$	18	-0.4	12	4.7	69±4	0	0.014±0.003	1.23
IS:10m	$dC_{14}LC/H_2O$	18	7.0	12	0.8	65±4	0	0.014±0.003	1.52
M	$dC_{14}LC/D_2O$	18	7.0	11	4.9	65±4	0	0.013±0.003	0.83
pH 7	$hC_{14}LC/D_2O$	18	-0.4	12	4.4	69±4	0	0.016±0.003	0.95
IS:160m	$dC_{14}LC/H_2O$	18	7.0	11	0.9	64±4	0	0.013±0.003	1.76
M	$dC_{14}LC/D_2O$	18	7.0	11	4.9	67±4	0	0.013±0.003	3.30
pH 2	$hC_{14}LC/D_2O$	19	-0.4	12	4.5	73±4	16±5	0.015±0.003	3.13
IS:10m	$dC_{14}LC/H_2O$	18	7.0	11	0.6	69±4	16±5	0.015±0.003	1.12
M	$dC_{14}LC/D_2O$	18	7.0	10	4.8	65±4	20±5	0.015±0.003	1.84
pH 2	$hC_{14}LC/D_2O$	19	-0.4	12	4.3	73±4	16±5	0.015±0.003	1.32
IS:160m	$dC_{14}LC/H_2O$	18	7.0	11	0.7	69±4	16±5	0.015±0.003	0.97
M	$dC_{14}LC/D_2O$	18	7.0	11	4.8	69±4	20±5	0.015±0.003	1.24
pH7	$hC_{16}LC/D_2O$	21	-0.4	12	4.4	88±5	0	0.016±0.003	2.85
IS:10m	$dC_{16}LC/H_2O$	21	7.0	13	0.5	82±5	0	0.017±0.003	2.80
M	$dC_{16}LC/D_2O$	20	7.0	12	4.9	78±5	0	0.015±0.004	3.16
pH 7	$hC_{16}LC/D_2O$	21	-0.4	13	4.6	83±5	0	0.015±0.005	3.56
IS:160m	$dC_{16}LC/H_2O$	20	7.0	12	0.7	83±5	0	0.015±0.005	2.15
M	$dC_{16}LC/D_2O$	20	7.0	12	4.8	83±5	0	0.015±0.005	4.03
pH 2	$hC_{16}LC/D_2O$	21	-0.4	12	4.5	89±5	25±5	0.016±0.004	2.31
IS:10m	$dC_{16}LC/H_2O$	21	7.0	12	0.5	89±5	18±5	0.015±0.005	2.11
M	$dC_{16}LC/D_2O$	20	7.0	11	4.8	79±4	29±5	0.015±0.005	2.09
pH 2	$hC_{16}LC/D_2O$	21	-0.4	13	4.3	88±4	25±5	0.016±0.004	3.23
IS:160m	$dC_{16}LC/H_2O$	21	7.0	13	0.8	83±5	18±5	0.016±0.004	2.02
M	$dC_{16}LC/D_2O$	20	7.0	13	4.9	75±5	29±5	0.014±0.004	3.12
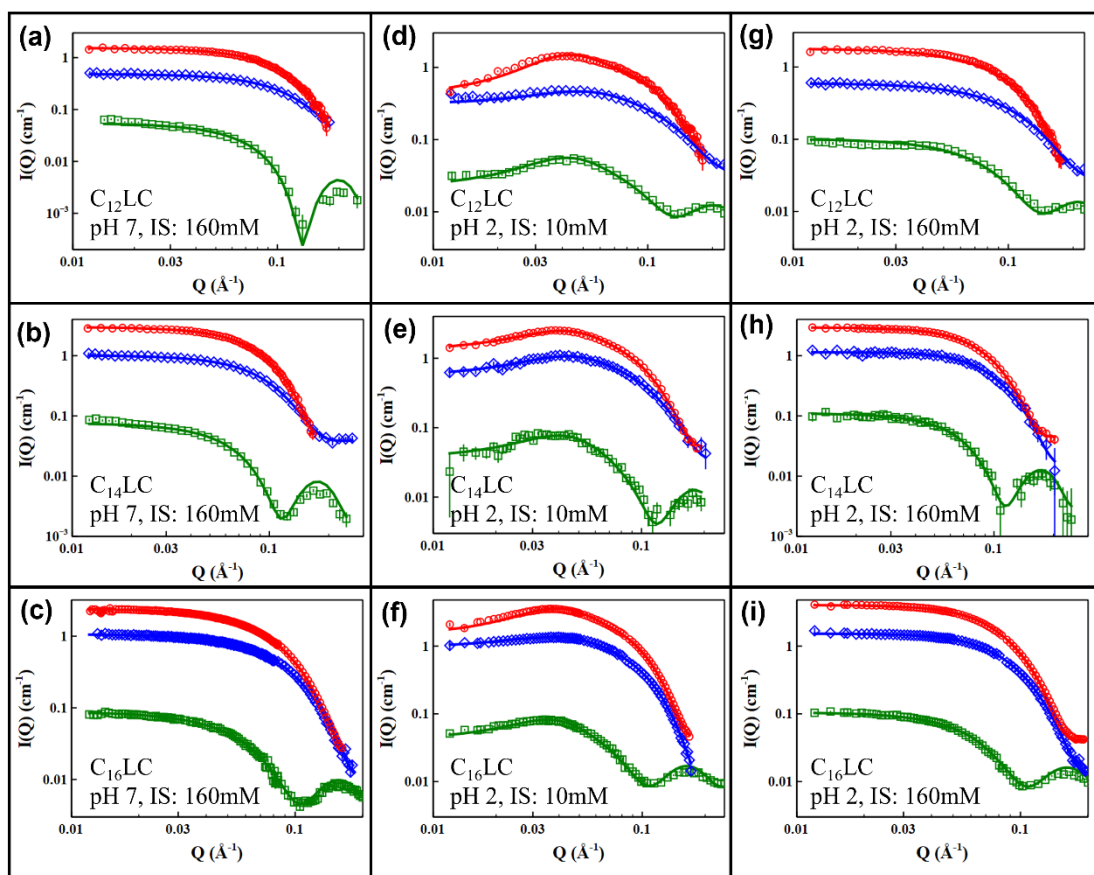
Figure 4.S4. SANS profiles measured from three contrasts of hC$_n$LC in D$_2$O (red circles), dC$_n$LC in H$_2$O (blue diamonds) and D$_2$O (green squares) at pH 7 with ionic strength (IS) of 160 mM (a,b,c);at pH 2 with IS of 10 mM (d,e,f);at pH 2 with IS of 160 mM (g,h,i). For clear visualization, all hC$_n$LC/D$_2$O data profiles have been shifted vertically by the multiplying factor 2.

Section E: NR profiles and best fit parameters for adsorbed C_nLC layers at the air/water interface at pH 7 and 2.
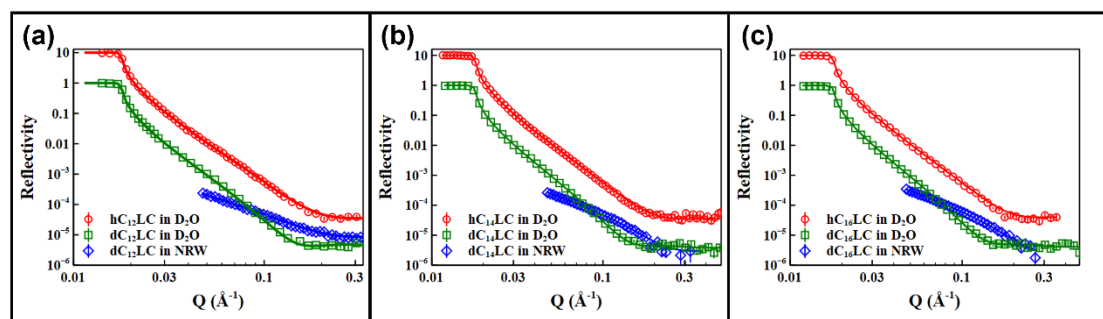
Figure 4.S5. Neutron reflection profiles measured at 3 contrasts: hC_nLC (2 CMC) in D_2O (red circles), shifted by multiplying 10 times to give a clear view, dC_nLC in NRW(blue diamonds) and D_2O (green squares) in pH 7 at an ionic strength of 10 mM: (a) $C_{12}LC$, (b) $C_{14}LC$ and (c) $C_{16}LC$

Table 4.S5. Best-fit parameters for the two-layer model fits for $C_{12}LC$, $C_{14}LC$ and $C_{16}LC$ under 3 contrasts: dC_nLC/D_2O, dC_nLC/NRW and hC_nLC/D_2O in 2 CMC at pH 7.

Contrast	Concn (mM)	τ_1 ± 2 (Å)	ρ_1 ± 0.2 (Å^{-2} ×10^{-6})	τ_2 ± 2 (Å)	ρ_2 ± 0.2 (Å^{-2} ×10^{-6})	$n_w \pm 2$
$C_{12}LC$						
$hC_{12}LC/D_2O$	2	12.1	-0.2	9.0	3.0	6
$dC_{12}LC/D_2O$	2	12.3	3.4	8.9	3.5	6
$dC_{12}LC/NRW$	2	12.2	3.4	9.0	2.2	6
$C_{14}LC$						
$hC_{14}LC/D_2O$	0.2	13.0	-0.2	9.6	2.9	8
$dC_{14}LC/D_2O$	0.2	13.2	3.7	9.3	4.8	8
$dC_{14}LC/NRW$	0.2	13.4	3.6	9.7	1.6	8
$C_{16}LC$						
$hC_{16}LC/D_2O$	0.02	14.0	-0.2	10.6	3.1	10
$dC_{16}LC/D_2O$	0.02	13.8	3.8	10.3	4.9	10
$dC_{16}LC/NRW$	0.02	13.6	4.1	9.8	1.5	10
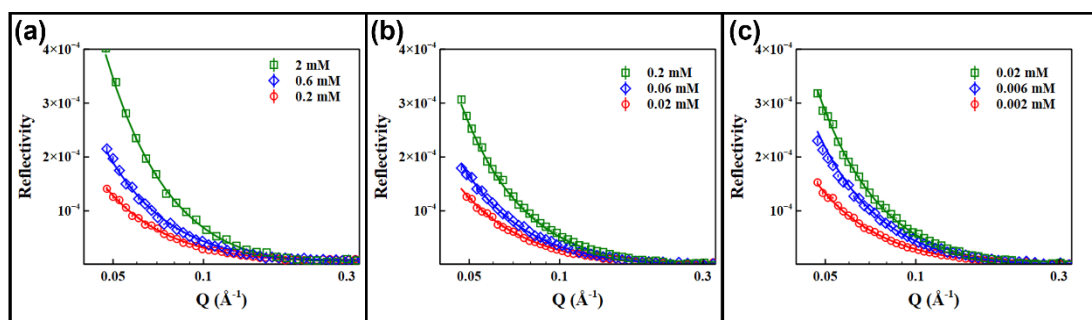
Figure 4.S6. Neutron reflectivity profiles of chain deuterated C_nLC in NRW at different concentrations at pH 2 with ionic strength (10 mM) for (a) $C_{12}LC$, (b) $C_{14}LC$ and (c) $C_{16}LC$.

Table 4.S6. The best-fit parameters from one-layer model for chain deuterated $C_{12}LC$, $C_{14}LC$ and $C_{16}LC$ in NRW at different concentrations at pH2. The surface excess (Γ) and area per molecule (A) are obtained by equations (4.2) and (4.3).

Surfactant	Concn (mM)	Thickness ± 2 (Å)	Layer SLD ± 0.2 (Å^{-2} ×10^{-6})	Γ ± 0.30 (µmol·m^{-2})	Γ ± 0.10 (mg·m^{-2})	A ± 2 (Å^2)
$C_{12}LC$	0.2	19.4	2.3	2.82	0.97	58.8
	0.6	20.3	2.6	3.33	1.14	49.9
	2	22.0	3.5	4.93	1.68	33.6
$C_{14}LC$	0.02	17.3	2.6	2.51	0.93	66.1
	0.06	19.6	2.7	2.93	1.09	56.7
	0.2	22.1	3.1	3.78	1.40	43.8
$C_{16}LC$	0.002	17.6	2.7	2.30	0.92	72.2
	0.006	20.2	2.9	2.91	1.16	57.0
	0.02	23.4	3.0	3.43	1.36	48.3

References

[1] C. Tanford, Micelle Shape and Size, The Journal of Physical Chemistry 76(21) (1972) 3020-3024.

[2] H. Liu, X. Hu, Z. Li, K. Fa, H. Gong, K. Ma, M. Liao, P. Li, J.R. Webster, J.T. Petkov, Surface Adsorption and Solution Aggregation of a Novel Lauroyl-L-Carnitine Surfactant, Journal of Colloid and Interface Science 591 (2021) 106-114.

Chapter 5

Structural features of interfacially adsorbed acyl-L-carnitines

Huayang Liu[1], Ke Fa[1], Xuzhi Hu[1], Zongyi Li[1], Lin Zhang[1], Kun Ma[2], Armando Maestro[3], Peixun Li[2], John RP Webster[2], Jordan T. Petkov[4], Robert K. Thomas[5], Jian Ren Lu[1,*]

[1] Biological Physics Laboratory, School of Physics and Astronomy, University of Manchester, Oxford Road, Manchester, M13 9PL, UK.

[2] ISIS Neutron Facility, Rutherford Appleton Laboratory, STFC, Chilton, Didcot, Oxon OX11 0QX, UK.

[3] Institut Laue-Langevin, 71 Avenue des Martyrs, CS20156, 38042 Grenoble Cedex 9, France

[4] Arch UK Biocides Ltd, Lonza, Hexagon Tower, Delaunays Road, Blackley, Manchester M9 8ZS, UK.

[5] Physical and Theoretical Chemistry, University of Oxford, South Parks, Oxford OX1 3QZ, UK

*Author to whom correspondence should be addressed. Email: j.lu@manchester.ac.uk

TOC:

pH 7, ionic strength: 1 mM
defective bilayer

7 Å

19 - 22 Å

7 Å

silica layer   14 Å

silicon substrate

pH 3, ionic strength: 1 mM
micelles adsorption

7 Å

15 - 18 Å

7 Å

silica layer

silicon substrate

Abstract

Hypothesis: Acyl-L-carnitines (C_nLCs) are potentially important as biosurfactants in drug delivery and tissue engineering due to their good biocompatibility. However, little is currently known about their basic interfacial behavior underlying their technological applications. Following our previous characterisations on their solution aggregation and adsorption at the air/water interface this work examines how they adsorb at the hydrophilic solid/water interface.

Experiments: As the SiO_2 surface has served as the model substrate for many interfacial adsorption studies, it has been used in this work as the solid substrate to facilitate dynamic adsorption by spectroscopic ellipsometry (SE) and structural determination of the adsorbed layers by neutron reflection (NR) under different conditions at the SiO_2/water interface from a group of C_nLC (n = 12, 14 and 16).

Findings: C_nLC surfactants are zwitterionic at neutral pH. They reach saturated adsorption above their critical micellar concentrations (CMCs) and formed a sandwiched bilayer with the head-tail-head structure at the hydrophilic SiO_2/water interface. The total thicknesses of the adsorbed layers at CMC were found to be 33 ± 2, 35 ± 2 and 37 ± 2 Å for $C_{12}LC$, $C_{14}LC$ and $C_{16}LC$, respectively, with their inner and outer head layers remaining similar but the thickness of the interdigitated middle layer increases with acyl chain length. As the solution becomes acidic, the carboxyl groups become protonated and the L-carnitine heads are net positively charged, resulting in increased repulsion between the head groups. In this situation, the C_nLC surfactants are adsorbed as distant aggregates to reduce repulsive interaction, resulting in reduced surfactant volume fraction and layer thickness. However, high ionic

strength could screen the repulsive interaction and enhance adsorbed amount, effectively diminishing the pH impact. This work provides a useful basis for exploring the technological applications of C_nLCs involving a solid substrate.

1. Introduction

Carnitine has the full name of 3-hydroxy-4-N-trimethyl-amino-butyric acid. It exists in two chiral enantiomers, L- and D-form. L-carnitine (LC) is widely present in our body systems, whereas D-carnitine is toxic [1, 2]. LCs are readily transformed into acylcarnitines (ACs) by enzymatic catalysis and the process plays a pivotal role in transferring fatty acids into the mitochondria during energy generation [3]. LCs can act as an antioxidant to protect the membrane of sperms from oxidant damage [4]. They can be synthesized in kidney and liver by healthy individuals, but some of us cannot synthesize enough due to genetic deficiency [5]. LC deficiency is often associated with diseases including diabetes, metabolic disorders, sepsis, and chronic hemodialysis [5-7]. Consequently, LCs are also used as nutrition supplements to prevent these diseases.

Extensive studies have indicated the importance of the chain length in ACs associated with human physiological processes and diseases. It has been reported that short-chain ACs, such as C_3 and C_5 ACs, are correlated with insulin resistance [8-10]. ACs with medium-chain length are related to gestational diabete mellitus, especially the onset of type 2 diabetes [11]. It appears that only long-chain ACs facilitate the transport of the long-chain fatty acids into mitochondria for β-oxidation associated with energy generation supporting physiological activities [12]. Thus, studies of physiochemical properties of ACs help understand the different physiological impact of these ACs. More importantly, these basic studies provide a useful basis for exploring their applications in drug delivery and biomaterials development. Additionally, alkyl/acyl LC esters show antimicrobial activity against a wide variety of bacteria, yeasts and fungi [13] and have high biocompatibility with both alkyl and acyl chains [14]. They are also of great potential in gene delivery [15].

147

In our previous studies, we have examined the solution aggregation behavior of a series of acyl-L-carnitines (C_nLCs), with different acyl tails (C_{12}-, C_{14}- and C_{16}-) [16]. Their basic adsorption behavior at the air/water interface has also been assessed. This work extends our continuous effort to further their characterisations by examining their adsorption at the solid/water interface. As SiO_2 surface has been widely used for outlining the adsorption features of surfactants, the silicon block has been used as the solid substrate to facilitate spectroscopic ellipsometry (SE) for examining their dynamic adsorption and neutron reflection (NR) to rationalize their adsorbed layer structures under different pH and ionic strength. Whereas SE is highly effective in following their dynamic adsorption, NR is highly sensitive to the depth inhomogeneity in the vertical direction at the interface. NR measurements under different isotopic contrasts help highlight different composition in adsorbed layers, leading to enhanced structural resolution. Adsorption at solid/liquid interfaces is an important characteristic that can be utilized to assess the adsorption behavior of a new series of surfactants, serving as a basis for guiding the development of practical applications, such as corrosion inhibition [17, 18], detergency [19], mineral flotation [20, 21]. However, many conditions need to be concerned to achieve these practical objectives, such as concentrations, solution environments.

2. Experimental Section

2.1. Materials

Lauroyl-L-carnitine ($C_{12}LC$, purity $\geq$ 99%), myristy-L-carnitine ($C_{14}LC$, purity $\geq$ 99%) and palmityl-L-carnitine ($C_{16}LC$, purity $\geq$ 99%) were synthesized following the method provided by Lonza [22]. Chain deuterated samples were synthesized by the same method as described in our previous work by the ISIS Deuteration Laboratory.

C_nLCs were purified by the method described in our previous work [16]. The starting C_nLC sample was first dissolved in water and the solution was titrated to neutral pH 7 by dilute NaOH solution. The solution was heated to keep the C_nLC sample totally soluble during titration. Then, water was removed by the freeze-dryer and the powder was dissolved in excess absolute ethanol. The insoluble NaCl was removed by filtration and the ethanol was dried off by rotary evaporation and freeze drying. The sample was dissolved in absolute acetone at 50 °C with enough absolute ethanol added just to dissolve the entire surfactant sample fully. As the solution cooled down crystals started to form. The solution was left for a few hours before filtering. The crystallization process was repeated 3 times to ensure good purity as indicated by the lack of surface tension minimum around critical micellar concentrations (CMC) as shown in **Figure 5.S1**.

2.2. Preparation of the SiO$_2$ surface

Silicon wafers <111> in 4 inch diameter with one of the large faces polished were bought from PI-KEM and cut in a size of $12{\times}12{\times}1$ mm^3 to fit the SE solid/liquid cell. Silicon blocks <111> in the dimensions of $80{\times}50{\times}9$ mm^3 were cut to fit the NR solid/liquid cell, with one of the large faces polished by PI-KEM. All silicon blocks have a native SiO$_2$ layer. Before use, the SiO$_2$ surfaces were prepared by exposing them to freshly prepared piranha solution [23]. The silicon wafers and blocks were immersed in the piranha solution (the mixture of 95% H_2SO_4 and $30 \pm 5\%$ H_2O_2 with the volume ratio of 9:1) at 90 °C for 1 - 3 min (1 min for the wafers and 3 min for the blocks). Then, the wafers and blocks were rinsed by plenty of ultrapure water (UHQ) and dried with nitrogen gas. The thicknesses of the native SiO$_2$ layers were found to be 14 ± 4 Å by SE and NR, with the error denoting range of variation between different surfaces. The wafers and blocks were kept in UHQ water before the experiments.

2.3. Spectroscopic ellipsometry (SE)

Surfactant adsorption at the solid/liquid interface was determined by a Woollam spectroscopic ellipsometer (J.A. Woollam Co. Inc) over the wavelength range of 200 - 600 nm [24]. SE measurements were performed in a purposely built solid/liquid cell with a pair of fused quartz window and incident angle of 70° for the light beam. The prepared silicon wafer ($12\times12\times1$ mm^3) was fixed on the central bottom of the solid/liquid cell. The sample solution was filled into the cell, and the reflected light beam from the solid/liquid interface was directed to the detector. After each measurement, the silicon wafers and cell were cleaned by 5% Decon 90 solution, UHQ water and dried by nitrogen gas. The calculation method of the adsorbed amount (Γ) of surfactant from the measured SE data is described in **Supporting information**.

2.4. Neutron reflection (NR)

NR measurements were performed on two reflectometers, SURF at the ISIS Neutron Faculty (Didcot, UK) and FIGARO at Institute Laue-Langevin (Grenoble, France). The reflectometers give the reflectivity, R, within a range of momentum transfer, $Q = (4\pi/\lambda)\sin\theta$ where λ is the neutron wavelength and θ is the incident angle. SURF sets 3 incident angles of 0.35°, 0.7° and 1.5° giving a Q range from 0.012 to 0.4 Å^{-1} [23]. FIGARO measures at two angles of 0.62° and 3.8° providing a Q range of 0.0045 to 0.42 Å^{-1}. The neutron beam size on the sample surface from the two different reflectometers were both around 4 cm^2 as determined by the slit settings.

The amount and structure of the adsorbed layer were determined by NR under different concentrations, pH and ionic strength with 3 isotopic contrasts: hC$_n$LC in D$_2$O, dC$_n$LC in D$_2$O and CM1.31 (contrast matching to the head group with the

150

scattering length density (SLD) of 1.31×10^{-6} Å^{-2}). Between each NR measurement, ethanol and 5% Decon 90 were injected into the solid/liquid cell to remove the adsorbed surfactant on the SiO_2 surface and inside the feeding system. Then the cell was rinsed by plenty of UHQ water before the next injection of the sample.

The NR data were fitted using the Motofit software. A uniform layer model was first used to provide a basic assessment of the overall adsorbed amount and layer thickness under different solution conditions. In some cases, the uniform layer model did not provide the best representation to the measured reflectivity profiles. A 3-layer model was then adopted by assuming that the adsorbed layer adopted a sandwiched packing with the head groups pointing outside and the acyl tails packing inside. The volumes, scattering lengths and SLDs of all samples involved are listed in **Table 5.S1**.

3. Results and Discussion

3.1. Interfacial adsorption kinetics

The molecular structures of C_nLC (n = 12, 14 and 16) are shown in **Figure 5.1**. Whilst $C_{12}LC$ is fully soluble in aqueous phase, $C_{14}LC$ has limited solubility over the temperature range of 20 – 25 °C and $C_{16}LC$ had low solubility displaying a sensitive concentration dependence above its critical micellar concentration (CMC). The surface tensions of C_nLCs were measured at the room temperature of 23 – 25 °C in the concentration range studied in this work and the results are shown in **Figure 5.S1**. Under these conditions $C_{14}LC$ and $C_{16}LC$ were found to be fully soluble. The CMCs of C_nLCs were found to be 1, 0.1 and 0.01 mM for $C_{12}LC$, $C_{14}LC$ and $C_{16}LC$, respectively. Changes of surface tension versus ln[concentration] below CMCs were fitted with quadratic equations which can be fed to the Gibbs equation to obtain surface adsorbed amount and area per molecule. The values of area per molecule at

CMC (A_{CMC}) were found to be 46, 48 and 49 $\mathring{A}^2$, consistent with the values reported previously [16]. The surface tension above CMCs changed little, and the overall adsorption features normal soluble surfactants, confirming that these surfactants remained soluble over the entire concentration range studied.
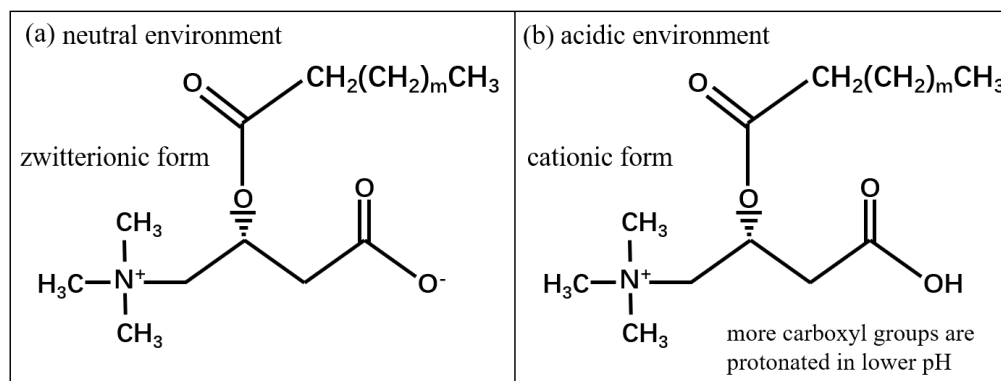
Figure 5.1. The chemical structures of C_nLC (n = m + 3) in (a) neutral environment and (b) acidic environment. The carboxyl group is negatively charged in neutral environment, and more carboxyl groups are protonated in lower pH. The trimethyl ammonium group is cationic in the range of pH.

The dynamic adsorption processes of C_nLC at the SiO_2/water interface were firstly measured by SE. **Figure 5.2(a)** shows an exemplar set of changes in the adsorbed amount of $C_{14}LC$ against time at the interface at pH 7 and ionic strength of 1 mM under different concentrations. The SE measurements started at time 0 against the buffer solution. Surfactant solutions were then injected at the 3rd min and the adsorbed amount (Γ) showed rapid increase upon sample injection. The initial rate of adsorption increases faster with concentration. At the lowest concentration of 0.05 mM, it took around 25 min to reach equilibrium. This is in contrast to about 8 min around its CMC (0.1 mM). Thus, it took a shorter time to reach equilibration as the surfactant concentration went up. This is consistent with the observed slowdown of

the rate of the adsorption as Γ tends to the equilibrium value at the low concentrations. At 0.2 mM (2× CMC), the adsorption rate showed a further increase, with Γ reaching the plateau within 2 min after injection.

$C_{12}LC$ and $C_{16}LC$ display similar dynamic adsorption processes as shown in **Figure 5.S2**, i.e., increased initial adsorption rates with rising bulk concentrations. They also reach the maximal adsorbed amount around their CMCs. The adsorbed amount at 2× CMC is similar between $C_{12}LC$ and $C_{14}LC$, at the values around 6.7 $\mu M/m^2$ but slightly higher for $C_{16}LC$, at about 7.4 $\mu M/m^2$ as shown in **Figure 5.2(b)**. For comparison, changes in Γ in mg/m^2 are shown in **Figure 5.S3**, displaying a clear trend of increase in adsorption with n above CMC.
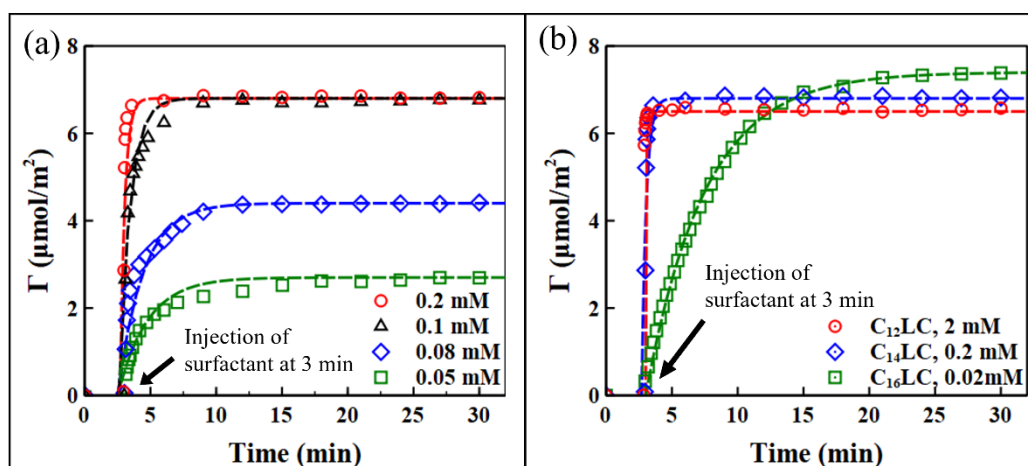
Figure 5.2. Time-dependent adsorption at the SiO$_2$/water interface from C_nLC surfactants by SE at pH 7 and the room temperature (23 - 25 °C) with the ionic strength of 1 mM (a) Adsorbed amount (Γ) of $C_{14}LC$ against time at the concentrations of 0.05, 0.08, 0.1 (CMC) and 0.2 mM. SE runs started at time 0 with buffer and then $C_{14}LC$ samples were injected at the 3rd min. The dashed lines represent the best fits from equation (5.1). (b) Adsorbed amount of C_nLC versus time

at 2× CMC. The dashed lines represent the best fits from equation (1). Γ expressed in mg/m^2 is shown in **Figure 5.S3** for comparison.

Figure 5.2(b) shows the dynamic adsorption processes of C$_n$LC (n=12, 14 and 16) fixed at 2× CMC with other solution conditions kept the same. C$_{16}$LC had an obviously lower initial adsorption rate than C$_{12}$LC and C$_{14}$LC before reaching the plateau adsorption. As the CMC of C$_{16}$LC is the lowest, the adsorption measurements were undertaken over the lowest concentration range. The rates of adsorption highly depended on the surfactant concentrations above CMC as well, as shown in **Figure 5.S2(b)**. As the concentration of C$_{16}$LC increased from 0.02, 0.05 to 0.1 mM, it took less time for the adsorption process to reach equilibrium. At 0.1 mM (10× CMC for C$_{16}$LC), the adsorption showed the fast initial rate similar to those observed from C$_{12}$LC and C$_{14}$LC. This phenomenon is also consistent with the behavior of nonionic surfactants C$_n$E$_6$ adsorbed at the SiO$_2$/water interface [25]. Whilst changes in the adsorbed amount of the three C$_n$LC surfactants are displayed in μM/m^2 in **Figure 5.2(b)** they can also be expressed in mg/m^2 as shown in **Figure 5.S3**. Both display similar trend.

The dashed lines as shown in **Figure 5.2(a)** and **(b)** represent the best fits to the dynamic adsorption using the model developed by Buijs et al [26]

$$\Gamma(t) = A^{-1}(1 - e^{-BA(t-t_0)}) \tag{5.1}$$

where A is the inverse of the equilibrium adsorbed amount, t $(t \geq t_0)$ is the time after t_0, the sample injection time which was marked as the injection at 3rd min (t_0) in this work, and B is the initial adsorption rate expressed as

$$B = \left(\frac{d\Gamma}{dt}\right)_{t \to t_0} = J_0 e^{(-G/RT)} \tag{5.2}$$

where J_0 is the surfactant flux being proportional to the surfactant concentration in solution, G is the Gibbs energy related to surfactant adsorption onto the SiO_2/water interface, R is the gas constant and T is the temperature [27]. **Table 5.1** shows the best fit parameters to the data shown in **Figure 5.2** using equation (5.1). The inverse of A is equal to the plateau adsorbed amount at a given concentration and B increases with concentration. Below CMC, B is almost proportional to the concentration, indicating that the adsorption energy is not constant as shown from $C_{14}LC$ below CMC. When the concentration is equal to or above CMC, B has a significant increase as the monomers form micelles in the bulk solution leading to difference in adsorption energy. Similarly, $C_{12}LC$ and $C_{16}LC$ have the same trend as shown in **Figure 5.S2** and **Table 5.S2**.

For the three C_nLCs at 2× CMC, B decreases significantly as the acyl chain length increases, indicating the initial adsorption rate is mainly affected by the hydrophobicity of C_nLC. The parameters show an almost linear relationship between the logarithm of B and the acyl chain length. This is consistent with the relationship between their CMC values and the acyl chain length as previously discussed.

There are limitations to the use of equation (5.1) in fitting the whole adsorption process. B is clearly not a constant during the whole adsorption process. When the adsorbed amount increases close to the plateau value, less empty surface makes it harder for the newly arriving surfactant molecules to adjust and adsorb onto the SiO_2 surface, leading to the difference in the Gibbs energy and reduction in the adsorption rate. In this work, however, equation (5.1) is adequate to assess the adsorption kinetics of C_nLC with different chain lengths under different concentration ranges because they are structurally simple and the mean field assumption can be adopted to tolerate these changes.

Table 5.1: The best fit parameters to the measured dynamic adsorption as shown in **Figure 5.2** using equation (5.1). A represents the inverse of the equilibrium adsorbed amount and B represents the initial adsorption rate. Conc is short for the concentration expressed in mM.

	Conc (mM)	A^{-1} ($\mu mol \cdot m^{-2}$)	B ($\mu mol \cdot m^{-2} \cdot min^{-1}$)
$C_{14}LC$	0.2	6.85	20.50
	0.1	6.84	8.20
	0.08	4.45	2.30
	0.05	2.70	1.20
$C_{12}LC$	2	6.54	126.75
$C_{16}LC$	0.02	7.42	1.64

3.2. Equilibrium adsorbed amount and layer structure

Figure 5.3(a) shows the adsorption isotherms of C_nLC at the SiO_2/water interface at different concentrations and pH 7 with ionic strength fixed at 1 mM. The concentration-dependent structural changes were monitored against the respective CMCs of C_nLC. In the low concentrations well below CMCs, very few C_nLC monomers adsorbed, driven by weak hydrophilic association or electrostatic interaction with the SiO_2 surface as C_nLC molecules are zwitterionic, a feature broadly similar to nonionic surfactants [28]. The adsorbed amount remained low until the concentrations reached 0.3 - 0.5× CMCs. The C_nLC molecules then began to form surface aggregates, leading to the obvious increase in the adsorbed amount. This concentration range is often called the critical surface aggregation concentrations (CSACs), The CSACs of C_nLC are lower than those of C_nE_6, which are typically 0.6 – 0.9× CMCs [29]. Above CSACs, the adsorption underwent a sharp rise and tended to plateau at CMC for $C_{12}LC$ and $C_{14}LC$, but at 2× CMC for $C_{16}LC$.
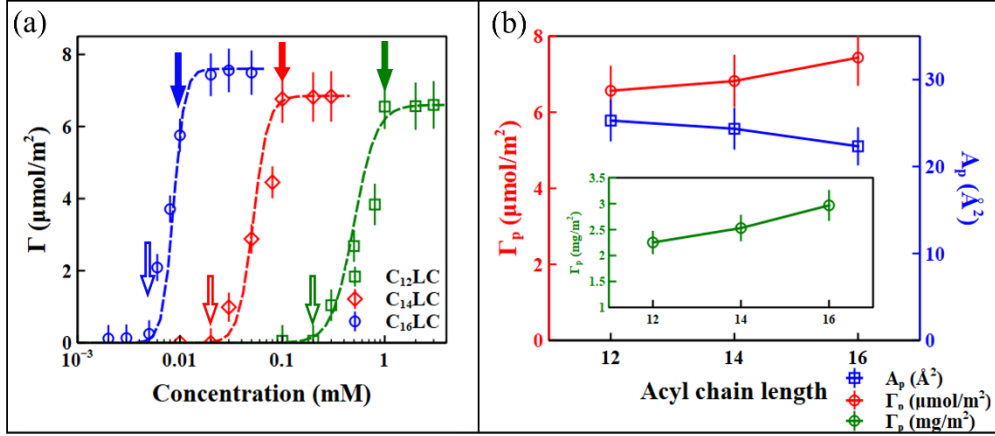
Figure 5.3. Changes of equilibrium adsorbed amount with bulk concentration from SE at pH 7 and room temperature under the ionic strength of 1 mM. (a) Adsorption isotherms for $C_{12}LC$ (green squares), $C_{14}LC$ (red diamonds), and $C_{16}LC$ (blue circles). The onsets of CSACs of C_nLC are indicated by open arrows and the CMCs are indicated by filled arrows. The alternative plots of the adsorbed amount expressed in mg/m^2 are shown in **Figure 5.S4**. The dashed lines represent the best fits from equation (3). (b) The adsorbed amount (Γ_p) and area per molecule (A_p) at $2\times$ CMC as a function of the acyl chain length (n). The inset in (b) shows Γ_p expressed in mg/m^2. The solid lines are drawn to help read the data.

For this C_nLC/water/SiO_2 system, the adsorption isotherms of C_nLC have two regions. In the first region with the concentration much lower than their CMCs, few monomers adsorb onto the SiO_2 surface leading to little adsorption amount. In the second region where the concentration is equal to or above CSACs, the adsorption isotherm increases rapidly and reaches the plateau values around CMC. For this situation, Zhu et al. developed the following equation for the S-type adsorption isotherm [30-32]:

$$\Gamma = \frac{\Gamma_{max} K c^n}{1 + K c^n} \qquad (5.3)$$

where Γ_{max} is the maximal adsorbed amount, c is the concentration and n is the average aggregation number of the surface aggregates. K is the equilibrium constant

for the process of n monomers aggregating on the surface (S) expressed by following equation

$$S + n\,monomers \rightleftharpoons surface\,aggregate\,.$$ (5.4)
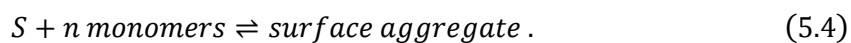
Table 5.2 shows the best fit parameters for the adsorption isotherms in **Figure 5.3(a)** using equation (5.3). The values of n are much lower than the aggregation number of their micelles in bulk solution as determined previously. K and n values both depend on the hydrophobicity of C_nLC molecules, showing an increment with acyl chain length. This indicates that $C_{16}LC$ molecules have a stronger trend to aggregate onto the SiO_2 surface than $C_{12}LC$ and $C_{14}LC$.

Table 5.2: The best fit parameters from fitting the measured adsorption isotherms shown in **Figure 5.3(a)** using equation (5.3). K is the equilibrium constant for the process described by equation (5.4) and n is the aggregation number of a surfactant aggregate adsorbed on the surface.

	K	n
$C_{12}LC$	$10^{1.2}$	4
$C_{14}LC$	$10^{7.7}$	6
$C_{16}LC$	$10^{16.5}$	8

The plateau adsorbed amount (Γ_p) of C_nLC at the SiO_2/water interface increased with the acyl chain length as shown in **Figure 5.3(b)**. When the data is shown in mg/m^2, the same trend holds for the maximal adsorption as shown in the inset plot. These features are similar to the performance of nonionic surfactant C_nE_6 (n = 12, 14, 16) at the SiO_2/water interface [25], indicating that the maximal Γ_p increases as the length of hydrocarbon chain increases. The plateau area per molecule (A_p) decreases from 25, 24 to 22 $Å^2$ as the acyl chain length increases. Similar trends have been reported from C_nE_6, but their A_p values are 40, 32, and 30 $Å^2$ for $C_{12}E_6$, $C_{14}E_6$, and $C_{16}E_6$, respectively [29] indicating that C_nLC has a closer packing.

Although SE is effective at measuring dynamic and equilibrium adsorbed amount, it is incapable of unravelling the thickness change due to the coupling of the thickness and composition for these surfactant nanofilms. NR is however well established for revealing the adsorbed layer structure at different interfaces [23, 33]. In this work, all NR measurements were carried out with polished silicon blocks as substrate. The piranha cleaned SiO_2 surfaces were first measured in D_2O (**Figure 5.4(a)** (blue diamonds)). Data analysis revealed the native SiO_2 layers to be 14 ± 4 Å thick, consistent with SE measurements. No roughness or cavities were used in the fitting model and the good fit to the measured data is indicative of the smooth SiO_2 surface.
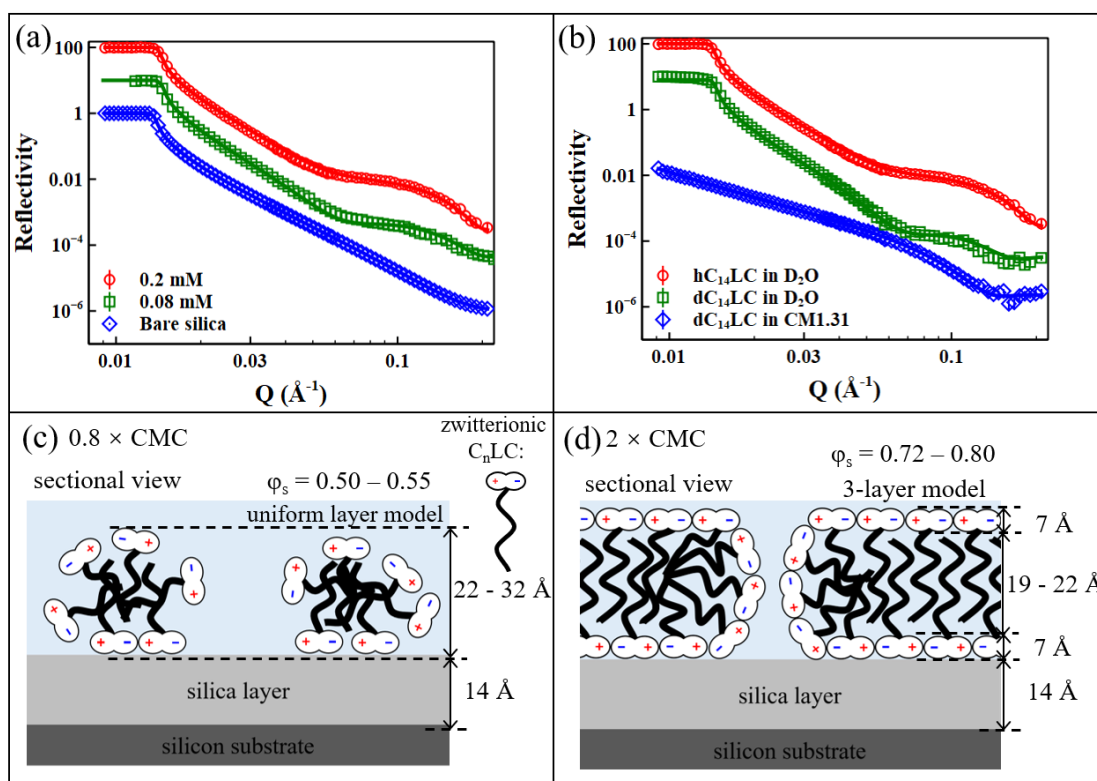
Figure 5.4. Structural determination by NR of $C_{14}LC$ layers adsorbed at the SiO_2/water interface under pH 7, ambient temperature, and ionic strength of 1 mM. (a) NR profiles of $hC_{14}LC$ adsorbed under concentrations at 0, 0.08, and 0.2 mM.

Continuous lines represent the best fits to the measured data. (b) NR profiles of 0.2 mM $C_{14}LC$ measured from three contrasts of $hC_{14}LC$ in D_2O (red circles), $dC_{14}LC$ in D_2O (green squares) and $dC_{14}LC$ in CM1.31 (blue diamonds). Continuous lines represent the best fits to the measured data. The data of green squares and red circles have been shifted vertically by the multiplying factor of 10 and 100 for better visualization. Schematic depictions of the structure of the C_nLC layer at (c) 0.8 × CMC and (d) 2 × CMC under pH 7 and ionic strength of 1 mM.

The effect of concentration on the adsorbed layer structure of $C_{14}LC$ at the SiO_2/water interface was examined by NR under pH 7 and ionic strength of 1 mM. The NR profiles of the protonated chain $C_{14}LC$ ($hC_{14}LC$) adsorbed from D_2O containing 0.08 and 0.2 mM are shown in **Figure 5.4(a)**. Their differences from the profile measured at the bare SiO_2/D_2O interface indicate the adsorption of $C_{14}LC$ below and above CMC, resulting in different adsorbed amount and layer thickness. The NR data was first fitted with a uniform layer model using the physical constants given in **Table 5.S1** and the best fit parameters are summarized in **Table 5.3**, with the underlying SiO_2 layer fixed at 14 ± 4Å. At 0.08 mM (just below CMC), the adsorbed layer had a thickness (τ) of 27 Å with the adsorbed amount (Γ_{NR}) of 3.88 $\mu mol \cdot m^{-2}$ and SLD (ρ) of 3.2×10^{-6} Å^{-2}. The surfactant volume fraction (φ_s) was found to be 0.55 with the area per molecule (A_{NR}) of 42.6 Å^2, calculated from **equation 5.S3 – S7**.

NR measurements were also made for $C_{12}LC$ and $C_{16}LC$ in similar solution conditions as shown in **Figure 5.S5 (a)** and **(b)** and their best fit parameters are listed in **Table 5.3** for comparison. The three C_nLC layers have similar φ_s around 0.50 – 0.55, but their τ values increase from 22, 27 to 32 Å. The τ values are between one and two extended C_nLC molecules as listed in **Table 5.S1** and about half of the adsorbed layer is water. As 0.8× CMC is above the CSAC, the C_nLC molecules must have

aggregated at the interface. But these aggregates could not reach the saturated amount at such low concentrations. As a result, most molecules would prefer to bind at the interface by weak interactions to form small discrete aggregates as depicted in **Figure 5.4(c)**. The high water volume fraction plus a lack of chain-head segregation leads to the good approximation of the uniform layer model to the adsorbed layer formed under these conditions.

The space between these aggregates could be occupied with more molecules as the concentrations increased further. At $2\times$ CMC, the adsorption reached the plateau as demonstrated from the SE measurements, resulting in increased τ and Γ_{NR}. Both of them increase significantly with acyl chain length, with τ increasing from 33, 35 to 37 Å. These changes were accompanied by increased φ_s of 0.72, 0.75, and 0.80 for $C_{12}LC$, $C_{14}LC$, and $C_{16}LC$, respectively. Γ_{NR} values were found to be 6.85, 6.89, and 7.02 $\mu mol \cdot m^{-2}$. The values of A_{NR} were determined to be 24.2, 24.1, and 23.3 $Å^2$ showing a slight decrease with acyl chain length. Γ_{NR} and A_{NR} values are highly consistent with those calculated from SE within errors.

As evident from **Table 5.3**, the τ values are between the length of one and two extended C_nLC molecules and the A_{NR} values are around half of those in the monolayer at the air/water interface. These changes indicate that the C_nLC molecules form a bilayer at the SiO_2/water interface with interweaving tails above their CMCs as depicted in **Figure 5.4(d)**. The headgroups of C_nLC molecules are either adsorbed at the SiO_2/water interface via self-assembly due to different interactions or projected outside into bulk water. As the plateau approaches above CMCs, the packing density increases and water is expelled out of the bilayer, but the thickness of the C_nLC bilayer at the SiO_2/water interface does not change much. Thus, increased insertion of surfactant molecules results in the expansion of the size of the surface confined

aggregates and expulsion of water. Changes in area per molecule support the bilayer packing in reference to the progression of the monolayer at the air/water interface. The thickness and SLD of the head and tail layers are highly different due to their different physical properties and water association. As the bilayer is further structured, however, the uniform layer model becomes limited in describing the better-organized structuring of the head and tail layers.

Table 5.3: The best-fit parameters from uniform layer model for hC_nLC in D_2O at different concentrations (0.8× and 2× CMC) under pH 7, room temperature and ionic strength of 1 mM. τ and ρ denote the thickness and SLD of the adsorbed layer. Γ_{NR} and A_{NR} denote the adsorbed amount and area per molecule calculated from best fits to NR profiles.

	Conc (mM)	$\tau \pm 2$ (Å)	$\rho \pm 0.2$ ($\text{Å}^{-2} \times 10^{-6}$)	$\Gamma_{NR} \pm 0.3$ ($\mu mol \cdot m^{-2}$)	$\Gamma_{NR} \pm 0.1$ ($mg \cdot m^{-2}$)	$A_{NR} \pm 2$ (Å^2)
$C_{12}LC$	0.8	22	3.0	3.67	1.26	45.7
	2	33	2.0	6.85	2.35	24.2
$C_{14}LC$	0.08	27	3.2	3.88	1.44	42.6
	0.2	35	1.8	6.89	2.55	24.1
$C_{16}LC$	0.008	32	3.6	3.68	1.47	45.1
	0.02	37	1.5	7.02	2.80	23.3

Chain deuterated C_nLCs (dC_nLC) were used to obtain further information about the adsorbed layer structure above CMCs when the adsorbed layers tend to plateau. NR measurements with 3 isotropic contrasts, hC_nLC in D_2O, dC_nLC in D_2O and CM1.31 (contrast matched to the head group, $\rho = 1.31 \times 10^{-6}$ Å^{-2}), were undertaken for each surfactant. As an example, **Figure 5.4(b)** shows the NR profiles of $C_{14}LC$ at 0.2 mM and pH 7 with the low ionic strength of 1 mM. The adsorbed layer was best fit by a 3-layer model, including inner, central and outer layers with summarized structural parameters in **Table 5.4**. The thickness of the inner layer (τ_1) containing the surfactant

head groups and water is 7 Å. The outer layer (τ_3), also containing the heads and water shows consistent thickness and composition, suggesting a symmetrical bilayer. The central layer, comprised of the interdigitated acyl chains, has a high thickness (τ_2) of 20 Å. The best fits using the same 3-layer model to the $C_{12}LC$ and $C_{16}LC$ NR profiles measured under similar conditions are shown in **Figure 5.S5(c)** and **(d)** with structural parameters listed in **Table 5.4**. All three C_nLC surfactants have same inner and outer head layers, but the thicknesses of the central layers increase from 19, 20 to 22 Å for $C_{12}LC$, $C_{14}LC$, and $C_{16}LC$, respectively, with more detailed structural parameters obtained from the best fits given in **Table 5.S4**. The values of Γ_{NR} and A_{NR} calculated from the 3-layer model are consistent with the uniform layer model within errors.

These model analyses indicate that whilst the uniform layer model is simple and incorporates the least number of variables, the 3-layer model is physically more appropriate to fit the surfactant bilayer with the head-tail-head structure as depicted by **Figure 5.4(d)**. However, the bilayer structure is not perfect as there must still be some water 'holes' in it, leading to φ_s of 0.72 - 0.80 as depicted in **Figure 5.4(d)**, even at the bulk concentrations around 2× CMC. As the bulk surfactant goes down below CMC, the surfactant packing density decreases and water volume fraction rises, leading to the smaller surface confined surfactant aggregates and less well-packed bilayer. Thus, all C_nLC surfactants could form the head-tail-head bilayer structure at the SiO_2/water interface, characterized by the thick inner layer and thick outer layers but the exact thickness of the central layer increases with acyl chain length, consistent with their increased hydrophobicity.

Table 5.4: C_nLC structural parameters summarized from the 3-layer model measured at 2× CMC, pH 7 and the ionic strength of 1 mM. τ_1, τ_2 and τ_3 denote the thickness of

inner, central and outer layers. Γ_{NR} and A_{NR} denote the adsorbed amount and area per molecule calculated from the best fits to the NR profiles.

	Conc (mM)	$\tau_1 \pm 2$ (Å)	$\tau_2 \pm 2$ (Å)	$\tau_3 \pm 2$ (Å)	$\Gamma_{NR} \pm 0.1$ ($\mu mol \cdot m^{-2}$)	$\Gamma_{NR} \pm 0.1$ ($mg \cdot m^{-2}$)	$A_{NR} \pm 2$ (Å^2)
C$_{12}$LC	2	7	19	7	6.85	2.35	24.1
C$_{14}$LC	0.2	7	20	7	6.87	2.55	24.1
C$_{16}$LC	0.02	7	22	7	7.22	2.88	23.0

3.3. Influences of pH changes on adsorbed layers

Further SE measurements were carried out to examine how pH changes affect the adsorption behavior of C$_n$LC at the SiO$_2$/water interface. **Figure 5.5(a)** shows the effect of pH on the adsorbed amount and area per molecule of C$_{14}$LC at 0.2 mM. The measurements were undertaken from pH 3 to 7 with fixed ionic strength of 1 mM. It can be seen that the adsorbed amount of C$_{14}$LC almost remained unchanged until the pH was below 4. When the pH was decreased to 3, the adsorbed amount decreased rapidly to 4.2 $\mu mol/m^2$, about 60% of that at pH 7. Meanwhile, the area per molecule had tripled compared to that at pH 7, from 24 to 39 Å^2. The SE data for C$_{12}$LC at 2 mM and C$_{16}$LC at 0.02 mM, shown in **Figure 5.S6(a)** and **(b)**, manifest the same trend as C$_{14}$LC. But C$_{16}$LC has a much lower adsorbed amount at pH 3, at 2.9 $\mu mol/m^2$, 40% of that at pH 7. This level is much lower than the values from C$_{12}$LC and C$_{14}$LC. The area per molecule of C$_{16}$LC at pH 3 is 56 Å^2, about 2.5 times of that at pH 7. This value is much higher than 35 Å^2 for C$_{12}$LC and 39 Å^2 for C$_{14}$LC at pH 3.

The pKa of the carboxyl group on the L-carnitine head of C$_n$LC is around 3.5 in aqueous solution in the absence of excess electrolyte, and measurable changes to its protonation start when pH is below 5 [34, 35]. As C$_n$LC molecules exist in zwitterionic form around pH 7, the adsorbed amount is virtually unaffected by pH

changes from 5 to 7. In this pH range, the SiO_2 surface exhibits negative charges in aqueous solution [36, 37], but C_nLC molecules have no net charge, resulting in weak electrostatic attraction between C_nLC and SiO_2 surface. Whilst such weak charged related binding between surfactant molecules and the SiO_2 surface drives their adsorption in the pH range of 5 to 7, the adsorbed amount is controlled by the relatively more hydrophobic nature of the surfactant molecules in the zwitterionic form.

At pH 3 - 4, the SiO_2 surface carries even less weak negative charges [36-38], but C_nLC molecules transform from zwitterionic with no net charge to cationic with a net positive charge, leading to the stronger electrostatic attraction between the cationic adsorbed layer and weak anionic SiO_2 surface. However, lateral repulsion within the adsorbed bilayer also increases. This repulsive interaction together with the increased hydrophilicity of the positively charged surfactant molecules becomes in lower pH environment, resulting in decreased adsorption. It is worth mentioning that the CMCs of C_nLC increase significantly at pH 3 where some molecules have become cationic leading to relatively higher CSACs at the SiO_2/water interface and lower adsorption amount. As shown in **Figure 5.S7(a)**, the CMCs of $C_{12}LC$, $C_{14}LC$ and $C_{16}LC$ are 1.7 ± 0.5, 0.20 ± 0.05 and 0.02 ± 0.05 mM, respectively. These CMCs imply increased CSACs as well, when compared to the relative changes at pH 7, leading to a significant reduction in adsorption at pH 3.
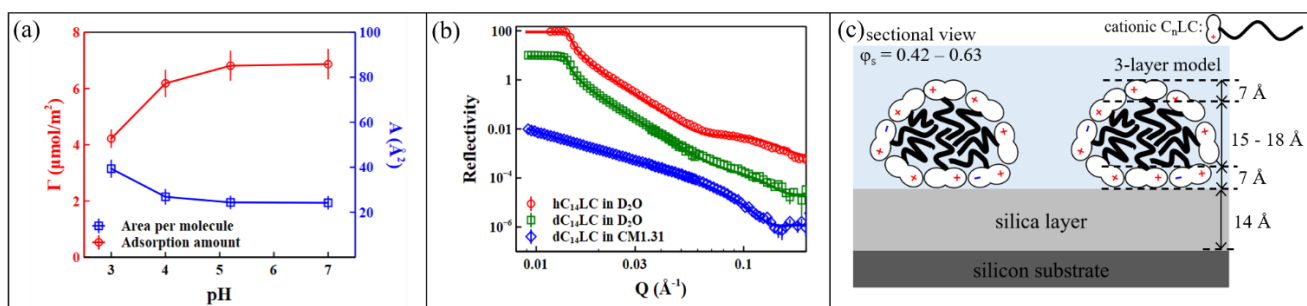
Figure 5.5. Effects of pH on interfacial adsorption from 0.2 mM $C_{14}LC$ at the SiO$_2$/water interface. (a) Changes of the adsorbed amount (Γ) and area per molecule (A) at different pH with ionic strength of 1 mM. (b) NR profiles (from 0.2 mM $C_{14}LC$ under pH 3 and ionic strength of 1 mM measured from three contrasts of $hC_{14}LC$ in D$_2$O (red circles), $dC_{14}LC$ in D$_2$O (green squares), and $dC_{14}LC$ in CM1.31 (blue diamonds). Continuous lines represent the best fit for the NR data. The data of green squares and red circles have been shifted vertically by the multiplying factor of 10 and 100 for better visualization. (c) Schematic depictions of the structure of the adsorbed $C_{14}LC$ bilayer.

The NR data profiles for C_nLC were measured from 3 contrasts at pH 3 with the ionic strength of 1 mM, where the adsorbed amount already had a significant decrease at the SiO$_2$/water interface. **Figure 5.5(b)** shows the NR profiles of $C_{14}LC$ at 0.2 mM and the best-fit parameters from the 3-layer model are summarized in **Table 5.5**. Comparing with its layer structure at pH 7, τ_2 and Γ_{NR} decreased to 17 Å and 4.47 μmol·m^{-2} (1.66 mg·m^{-2}) and A_{NR} increased to 37.1 Å^2. However, τ_1 and τ_3 remained the same in the neutral and acidic environments. The best fit NR data for $C_{12}LC$ and $C_{16}LC$ are shown in **Figure 5.S6(c)** and **(d)** with structural parameters given in **Table 5.5**, indicating a similar trend as $C_{14}LC$ under the neutral and acidic environments. The total thickness of the adsorbed layer are 29, 31 and 32 Å with A_{NR} of 35.3, 37.1 and 55.2 Å^2 for $C_{12}LC$, $C_{14}LC$ and $C_{16}LC$, respectively, consistent with the SE data

within errors. The φ_s values were calculated from **Table 5.S3**, being 0.63, 0.61 and 0.42, respectively, which are still significant but much lower than those at pH 7.

The neutron results show that the SiO_2 surface is not completely covered by C_nLC which is consistent with surface micellar adsorption. Around pH 3, a lot of carboxyl groups are protonated, resulting in cationic C_nLC micelles in solution and at the SiO_2/water interface. Apart from the repulsive force between surfactant molecules within surface confined micelles, the electrostatic repulsion between micelles leads to some distance between these aggregates at the interface, resulting in reduced micellar adsorption and a high volume fraction of water as depicted in **Figure 5.5(c)**. The total thickness of the layer is between one and two times the extended length of C_nLC molecules. So the tails are interdigitated or tilted, resulting in flattened micelles adsorbed at the interface, similar to the bilayer structure of $C_{16}TAB$ formed at the flat SiO_2water interface [33]. The micellar adsorption as revealed from NR is also consistent with the observations of the nanostructures formed by $C_{14}TAB$ and $C_{16}TAB$ on the same SiO_2 surface by atomic force microscopy (AFM) [39-41].

Table 5.5: Main structural parameters of C_nLC layers obtained from the best fit 3-layer model at pH 3 with different ionic strength (IS). The detailed fit parameters for each contrast are listed in **Table 5.S4**.

	Conc (mM)	IS (mM)	$\tau_1 \pm 2$ (Å)	$\tau_2 \pm 2$ (Å)	$\tau_3 \pm 2$ (Å)	$\Gamma_{NR} \pm 0.1$ ($\mu mol \cdot m^{-2}$)	$\Gamma_{NR} \pm 0.1$ ($mg \cdot m^{-2}$)	$A_{NR} \pm 2$ ($Å^2$)
$C_{12}LC$	2	1	7	15	7	4.72	1.62	35.3
		151	7	18	7	6.50	2.23	25.6
$C_{14}LC$	0.2	1	7	17	7	4.47	1.66	37.1
		151	7	19	7	6.44	2.39	25.8
$C_{16}LC$	0.02	1	7	18	7	3.00	1.20	55.2
		151	7	21	7	6.52	2.60	25.5

3.4. Influences of ionic strength on adsorbed layers

SE measurements were also undertaken to examine the effect of ionic strength on the adsorption of C_nLC at the SiO_2/water interface at pH 3, but with the ionic strength being kept at 1 and 151 mM (by adding NaCl). The high ionic strength is close to that of the physiological fluids. At pH 7, the ionic strength has little effect on the adsorption of C_nLC due to their zwitterionic form. **Figure 5.6(a)** shows the adsorption behavior of $C_{14}LC$ at pH 3 with low and high ionic strength. Under the low ionic strength of 1 mM, the adsorbed amount was much lower than that at pH 7 and it increased more slowly with surfactant concentration. When the ionic strength increased, it had two effects: screening of the electrostatic repulsion and reduction of the CMC and CSAC of $C_{14}LC$ to the level at pH 7. As shown in **Figure 5.6(a)**, the adsorption behavior of $C_{14}LC$ behaves similarly to what was observed pH 7 under the screening effect from the high ionic strength at pH 3. Furthermore, $C_{12}LC$ and $C_{16}LC$ show similar behavior as shown in **Figure 5.S8(a)** and **(b)**.
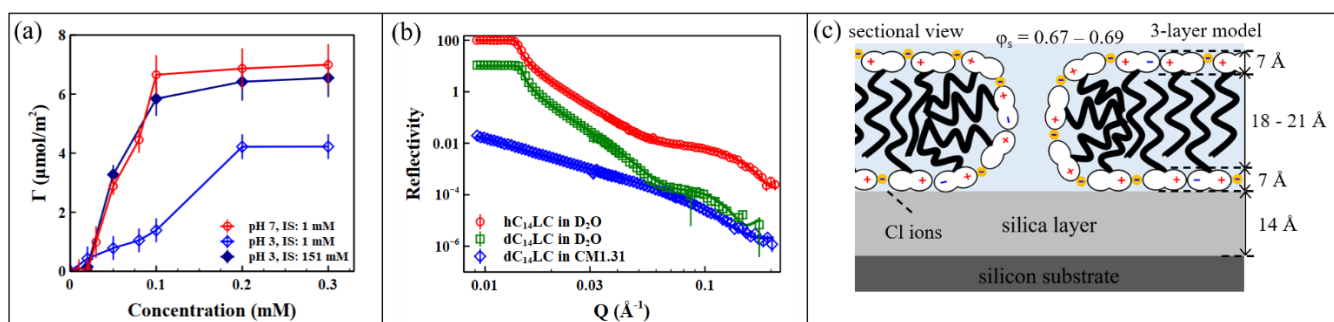
Figure 5.6. Effects of ionic strength on interfacial adsorption of 0.2 mM $C_{14}LC$ at pH 3 and room temperature. (a) Adsorption isotherms obtained from the ionic strength of 1 (open diamonds) and 151 mM (filled diamonds), with the data at pH 7 also plotted for comparison. The solid lines are drawn to help read the data. (b) NR profiles measured under the ionic strength of 151 mM from three contrasts of $hC_{14}LC$ in D_2O

(red circles), $dC_{14}LC$ in D_2O (green squares) and $dC_{14}LC$ in CM1.31 (blue diamonds). Continuous lines represent the best fits to the NR data. The data of green squares and red circles have been shifted vertically by the multiplying factor of 10 and 100 for better visualization. (c) Schematic depictions of the structure of the adsorbed $C_{14}LC$ layer under pH 3 and the ionic strength of 151 mM.

NR measurements of $C_{14}LC$ were then carried out to examine the structure of the adsorbed layer at pH 3 with ionic strength of 151 mM, shown in **Figure 5.6(b)** with structural parameters listed in **Table 5.5**. Under high ionic strength, τ_1 and τ_3 do not change, but the τ_2 became thicker than that measured in low extra electrolyte. Γ_{NR} increased to 6.44 $\mu mol \cdot m^{-2}$, but is slightly lower than that at pH 7. The data of $C_{12}LC$ and $C_{16}LC$ followed a similar trend as shown in **Figure 5.S7(c)** and **(d)** and **Table 5.5**. The thickness of all three adsorbed layers increased to 32, 33 and 35 Å with φ_s also increased to about 0.68. The high ionic strength thus screened the repulsion between cationic C_nLC molecules with aggregates and between them, leading to greater packing within the interfacial layers at the SiO_2/water interface as depicted in **Figure 5.6(c)**.

The combined SE and NR have provided a complementary evaluation of dynamic and structural changes at the SiO_2/water interface. NR is especially powerful at unravelling changes in the structure and composition within each adsorbed layer with typically ± 2 Å depth resolution. This sensitivity together with the accurate determination of changes in component volume fraction has offered us a useful outline of the main structural features of the adsorbed bilayer and their detailed changes as a function of acyl chain length, pH, and ionic strength. Because of the lack of lateral resolution, however, structural features relating to the in-plane packing can only be inferred to and the bilayer structure represents the averaged interpretation.

Advances in AFM studies have provided rich structural information about adsorbed surfactants, especially concerning surface induced aggregation around CMC. For example, Subramanian and Ducker have shown from their AFM study the successful determination of the shapes of micelles adsorbed at the SiO_2/water interface [41]. Their work reported that spherical surface micelles of hexadecyltrimethylammonium ions form in the presence of counterions, such as CH_3COO^-, CO_3^-, SO_4^{2-}, even at the ionic concentrations above 100 mM. Cl^- and Br^- promote slightly oblate micelles near their CMCs. Interestingly, the addition of Br^- can help transform to cylindrical micelles but the addition of Cl^- does not. The authors have interpreted these spherical-cylindrical changes in micellar shape to the different ability of the ions to bind to the surfactant head groups, thereby causing different electrostatic interactions. In light of the different structure of L-carnitine and its pH-dependent charge response, future studies will assess how pH, ion type and strength affect the transformation of micellar shape, a feature important for surface based self-assembly, nanostructuring and controlled drug loading and release.

4. Conclusion

Acyl-L-carnitines and their esters have fast become a group of amphiphiles with attractive potential in a range of applications including antimicrobial activity and gene delivery [13, 15] due to their biocompatibility and biodegradability inherent from their natural origin. However, their technological exploitation hinges on the understanding of their basic aggregation behavior and interfacial adsorption. Following our previous studies of their surface adsorption and solution aggregation in different environmental conditions, this work reports a first attempt to understand their adsorption at the solid/liquid interface. As bare SiO_2 surface has been widely used to rationalize surfactant adsorption, we have used it in this work to facilitate both

SE and NR measurements to understand how molecular structures, concentrations, pH, and ionic strength affect the adsorption behavior of C_nLCs (n = 12, 14 and 16) at the SiO_2/water interface. Whilst SE helped monitor dynamic adsorption NR in combination with deuterium labeled surfactants helped determine the structure of the adsorbed layers.

Our study has revealed that at pH 7 C_nLC surfactants behave broadly like nonionic C_nE_6 [29], with little adsorption at the SiO_2/water interface until the concentrations reach the CSACs which are about their 0.3 - 0.5× CMCs but which are lower than those for C_nE_6. The adsorbed amount then increases quickly with concentration and reaches a maximum above the CMC. The values of area per molecule of C_nLCs at plateau are 25, 24, and 22 $Å^2$ from both SE and NR; these values are 8 - 15 $Å^2$ lower than those of C_nE_6 [29], indicating closer packing in the C_nLC layers. These limiting molecular areas are nearly half of those in their monolayers formed at the air/water interface, suggesting the formation of a bilayer with the head-tail-head structure at the SiO_2/water interface. The total thicknesses of the adsorbed layers are 33, 35, and 37 Å with the symmetrical inner and outer head group layers of 6-7 Å thick and the central layer of 20 Å thick comprised of the interdigitated acyl chains.

When the pH decreases to 3, carboxyl groups become protonated. The repulsion within and between surface confined aggregates leads to reduced adsorbed amounts and thinning of the total thickness by 4 - 5 Å. These changes are consistent with the decreased surfactant volume fraction from around 0.8 to 0.5. Salt addition can effectively screen the repulsion between cationic C_nLC aggregates in acidic environment. Under high ionic strength, both thicknesses and volume fractions of the bilayer increase, but the total adsorbed amount is still slightly lower than that at pH 7.

This work has contributed to the understanding of the physicochemical properties of interfacial adsorption of C_nLCs in different conditions and also formed a useful basis for further exploring the detailed morphological transformations of the interfacial C_nLC micelles, e.g., caused by counterions or the chemical nature of the substrate surface, crucial for developing their technological applications.

Acknowledgments

Supporting Information

Further data in physical parameters of C_nLC, surface tension plots of C_{12}LC, C_{14}LC and C_{16}LC, the dynamic adsorption process of C_{12}LC and C_{16}LC, adsorption isotherms for C_nLC expressed in mg/m^2, adsorption amount of C_{12}LC and C_{16}LC at different pH and ionic strength measured by SE, NR profiles and the fitted parameters for C_{12}LC and C_{16}LC at pH 7 (IS: 1 mM) and pH 3 (IS: 1 and 151 mM).

References

[1] C.J. Gross, L.M. Henderson, Absorption of D-and L-Carnitine by the Intestine and Kidney Tubule in the Rat, Biochimica et Biophysica Acta (BBA)-Biomembranes 772(2) (1984) 209-219.

[2] I. Tamai, R. Ohashi, J.-i. Nezu, H. Yabuuchi, A. Oku, M. Shimane, Y. Sai, A. Tsuji, Molecular and Functional Identification of Sodium Ion-Dependent, High Affinity Human Carnitine Transporter Octn2, Journal of Biological Chemistry 273(32) (1998) 20378-20382.

[3] F.M. Vaz, R.J. Wanders, Carnitine Biosynthesis in Mammals, Biochemical Journal 361(3) (2002) 417-429.

[4] S. Ahmed, S. Ahsan, T. Iqbal, S.A. Burney, Relationship of Seminal Free L-Carnitine with Functional Spermatozoal Charac-Teristics: Results from an-Observational Study Conducted in a Ter-Tiary Care Hospital of Karachi, Pakistan, Journal of Pakistan Medical Association 67(2) (2017) 280-284.

[5] P.B. Celestino-Soper, S. Violante, E.L. Crawford, R. Luo, A.C. Lionel, E. Delaby, G. Cai, B. Sadikovic, K. Lee, C. Lo, A Common X-Linked Inborn Error of Carnitine Biosynthesis May Be a Risk Factor for Nondysmorphic Autism, Proceedings of the National Academy of Sciences 109(21) (2012) 7974-7981.

[6] J.L. Flanagan, P.A. Simmons, J. Vehige, M.D. Willcox, Q. Garrett, Role of Carnitine in Disease, Nutrition & metabolism 7(1) (2010) 1-14.

[7] S. Ahmad, L-Carnitine in Dialysis Patients, Seminars in Dialysis, Wiley Online Library, 2001, pp. 209-217.

[8] M.G. Schooneman, F.M. Vaz, S.M. Houten, M.R. Soeters, Acylcarnitines: Reflecting or Inflicting Insulin Resistance?, Diabetes 62(1) (2013) 1-8.

[9] C.B. Newgard, J. An, J.R. Bain, M.J. Muehlbauer, R.D. Stevens, L.F. Lien, A.M. Haqq, S.H. Shah, M. Arlotto, C.A. Slentz, A Branched-Chain Amino Acid-Related Metabolic Signature That Differentiates Obese and Lean Humans and Contributes to Insulin Resistance, Cell Metabolism 9(4) (2009) 311-326.

[10] M. Rousseau, F. Guénard, V. Garneau, B. Allam-Ndoul, S. Lemieux, L. Pérusse, M.-C. Vohl, Associations between Dietary Protein Sources, Plasma Bcaa and Short-Chain Acylcarnitine Levels in Adults, Nutrients 11(1) (2019) 173.

[11] B. Batchuluun, D. Al Rijjal, K.J. Prentice, J.A. Eversley, E. Burdett, H. Mohan, A. Bhattacharjee, E.P. Gunderson, Y. Liu, M.B. Wheeler, Elevated Medium-Chain Acylcarnitines Are Associated with Gestational Diabetes Mellitus and Early Progression to Type 2 Diabetes and Induce Pancreatic B-Cell Dysfunction, Diabetes 67(5) (2018) 885-897.

[12] T.N. Tarasenko, K. Cusmano-Ozog, P.J. McGuire, Tissue Acylcarnitine Status in a Mouse Model of Mitochondrial B-Oxidation Deficiency During Metabolic Decompensation Due to Influenza Virus Infection, Molecular Genetics and Metabolism 125(1-2) (2018) 144-152.

[13] M. Calvani, L. Critelli, G. Gallo, F. Giorgi, G. Gramiccioli, M. Santaniello, N. Scafetta, M.O. Tinti, F. De Angelis, L-Carnitine Esters as "Soft", Broad-Spectrum Antimicrobial Amphiphiles, Journal of Medicinal Chemistry 41(13) (1998) 2227-2233.

[14] J. Nivet, M. Le Blanc, J. Riess, Synthesis and Preliminary Evaluation of Perfluoroalkylacyl Carnitines as Surfactants for Biomedical Use, European Journal of Medicinal Chemistry 26(9) (1991) 953-960.

[15] J. Wang, X. Guo, Y. Xu, L. Barron, F.C. Szoka, Synthesis and Characterization of Long Chain Alkyl Acyl Carnitine Esters. Potentially Biodegradable Cationic Lipids for Use in Gene Delivery, Journal of Medicinal Chemistry 41(13) (1998) 2207-2215.

[16] H. Liu, X. Hu, Z. Li, K. Fa, H. Gong, K. Ma, M. Liao, P. Li, J.R. Webster, J.T. Petkov, R.K. Thomas, J.R. Lu, Surface Adsorption and Solution Aggregation of a Novel Lauroyl-L-Carnitine Surfactant, Journal of Colloid and Interface Science 591 (2021) 106-114.

[17] G. Mu, T. Zhao, M. Liu, T. Gu, Effect of Metallic Cations on Corrosion Inhibition of an Anionic Surfactant for Mild Steel, Corrosion 52(11) (1996) 853-856.

[18] M.L. Free, Understanding the Effect of Surfactant Aggregation on Corrosion Inhibition of Mild Steel in Acidic Medium, Corrosion Science 44(12) (2002) 2865-2870.

[19] Y. Yangxin, Z. Jin, A.E. Bayly, Development of Surfactants and Builders in Detergent Formulations, Chinese Journal of Chemical Engineering 16(4) (2008) 517-527.

[20] Y.-S. Cho, J. Laskowski, Effect of Flotation Frothers on Bubble Size and Foam Stability, International Journal of Mineral Processing 64(2-3) (2002) 69-80.

[21] H. Sis, S. Chander, Improving Froth Characteristics and Flotation Recovery of Phosphate Ores with Nonionic Surfactants, Minerals engineering 16(7) (2003) 587-595.

[22] D.L.M. Smida, TN), Process for the Production of a Fatty Acid/Carnitine Derivative, Lonza Ltd. (Visp, CH), United States, 2013.

[23] X. Hu, E. Pambou, H. Gong, M. Liao, P. Hollowell, H. Liu, W. Wang, C. Bawn, J. Cooper, M. Campana, K. Ma, P. Li, J.R.P. Webster, F. Padia, G. Bell, J.R. Lu, How Does Substrate Hydrophobicity Affect the Morphological Features of Reconstituted Wax Films and Their Interactions with Nonionic Surfactant and Pesticide?, Journal of Colloid and Interface Science 575 (2020) 245-253.

[24] F. Pan, Z. Li, T. Leyshon, D. Rouse, R. Li, C. Smith, M. Campana, J.R. Webster, S.M. Bishop, R. Narwal, C.F. van der Walle, J. Warwicker, J.R. Lu, Interfacial Adsorption of Monoclonal Antibody Coe-3 at the Solid/Water Interface, ACS Applied Materials & Interfaces 10(1) (2018) 1306-1316.

[25] F. Tiberg, B. Joesson, B. Lindman, Ellipsometry Studies of the Self-Assembly of Nonionic Surfactants at the Silica-Water Interface: Kinetic Aspects, Langmuir 10(10) (1994) 3714-3722.

[26] J. Buijs, P.A. van den Berg, W.T. James, W. Norde, J. Lyklema, Adsorption Dynamics of Igg and Its F (Ab′) 2and Fc Fragments Studied by Reflectometry, Journal of Colloid and Interface Science 178(2) (1996) 594-605.

[27] F. Pan, X. Zhao, S. Perumal, T.A. Waigh, J.R. Lu, J.R. Webster, Interfacial Dynamic Adsorption and Structure of Molecular Layers of Peptide Surfactants, Langmuir 26(8) (2010) 5690-5696.

[28] Z. Chang, X. Chen, Y. Peng, The Adsorption Behavior of Surfactants on Mineral Surfaces in the Presence of Electrolytes–a Critical Review, Minerals Engineering 121 (2018) 66-76.

[29] F. Tiberg, B. Joensson, J.-a. Tang, B. Lindman, Ellipsometry Studies of the Self-Assembly of Nonionic Surfactants at the Silica-Water Interface: Equilibrium Aspects, Langmuir 10(7) (1994) 2294-2300.

[30] B.-Y. Zhu, T. Gu, General Isotherm Equation for Adsorption of Surfactants at Solid/Liquid Interfaces. Part 1. Theoretical, Journal of the Chemical Society, Faraday Transactions 1: Physical Chemistry in Condensed Phases 85(11) (1989) 3813-3817.

[31] T. Gu, B.-Y. Zhu, The S-Type Isotherm Equation for Adsorption of Nonionic Surfactants at the Silica Gel—Water Interface, Colloids and surfaces 44 (1990) 81-87.

[32] B.-Y. Zhu, T. Gu, Surfactant Adsorption at Solid-Liquid Interfaces, Advances in colloid and interface science 37(1-2) (1991) 1-32.

[33] G. Fragneto, R.K. Thomas, A.R. Rennie, J. Penfold, Neutron Reflection from Hexadecyltrimethylammonium Bromide Adsorbed on Smooth and Rough Silicon Surfaces, Langmuir 12(25) (1996) 6036-6043.

[34] S.P. Moulik, M.E. Haque, P.K. Jana, A.R. Das, Micellar Properties of Cationic Surfactants in Pure and Mixed States, The Journal of Physical Chemistry 100(2) (1996) 701-708.

[35] S.H. Yalkowsky, G. Zografi, Potentiometric Titration of Monomeric and Micellar Acylcarnitines, Journal of Pharmaceutical Sciences 59(6) (1970) 798-802.

[36] S. Phanichphant, A. Nakaruk, D. Channei, Photocatalytic Activity of the Binary Composite Ceo2/Sio2 for Degradation of Dye, Applied Surface Science 387 (2016) 214-220.

[37] S. Garcia-Manyes, G. Oncins, F. Sanz, Effect of Ph and Ionic Strength on Phospholipid Nanomechanics and on Deposition Process onto Hydrophilic Surfaces Measured by Afm, Electrochimica Acta 51(24) (2006) 5029-5036.

[38] S. Ong, X. Zhao, K.B. Eisenthal, Polarization of Water Molecules at a Charged Interface: Second Harmonic Studies of the Silica/Water Interface, Chemical Physics Letters 191(3-4) (1992) 327-335.

[39] S. Manne, H.E. Gaub, Molecular Organization of Surfactants at Solid-Liquid Interfaces, Science 270(5241) (1995) 1480-1482.

[40] S.B. Velegol, B.D. Fleming, S. Biggs, E.J. Wanless, R.D. Tilton, Counterion Effects on Hexadecyltrimethylammonium Surfactant Adsorption and Self-Assembly on Silica, Langmuir 16(6) (2000) 2548-2556.

[41] V. Subramanian, W.A. Ducker, Counterion Effects on Adsorbed Micellar Shape: Experimental Study of the Role of Polarizability and Charge, Langmuir 16(10) (2000) 4447-4454.

Supporting information

Structural features of interfacially adsorbed acyl-L-carnitines

Huayang Liu[1], Ke Fa[1], Xuzhi Hu[1], Zongyi Li[1], Lin Zhang[1], Kun Ma[2], Armando Maestro[3], Peixun Li[2], John RP Webster[2], Jordan T. Petkov[4], Robert K. Thomas[5], Jian Ren Lu[1,]*

[1] Biological Physics Laboratory, School of Physics and Astronomy, University of Manchester, Oxford Road, Manchester, M13 9PL, UK.

[2] ISIS Neutron Facility, Rutherford Appleton Laboratory, STFC, Chilton, Didcot, Oxon OX11 0QX, UK.

[3] Institut Laue-Langevin, 71 Avenue des Martyrs, CS20156, 38042 Grenoble Cedex 9, France

[4] Arch UK Biocides Ltd, Lonza, Hexagon Tower, Delaunays Road, Blackley, Manchester M9 8ZS, UK.

[5] Physical and Theoretical Chemistry, University of Oxford, South Parks, Oxford OX1 3QZ, UK

*Author to whom correspondence should be addressed. Email: j.lu@manchester.ac.uk

Keywords: Antimicrobial surfactant, good compatibility, acyl-L-carnitine, pH responsive, interfacial adsorption.

Section A: Data analysis of spectroscopic ellipsometry (SE).

Changes in the polarization of light beam were measured by SE and analyzed by software (Complete EASE, J.A. Woollam Co. Inc) to give the thickness and refractive index of the adsorbed layer. The Cauchy equation was used to calculate the refractive index of the transparent and homogeneous surfactant layer [1]:

$$n(\lambda) = A + \frac{B}{\lambda^2} \tag{5.S1}$$

where λ is the wavelength of the light. A and B represents the Cauchy coefficients and are fixed at 1.37 and 0.01 in this work. The adsorption amount (Γ) of surfactant could be calculated by following De Feijter's formula [2]:

$$\Gamma = \frac{\tau(n\text{-}n_0)}{a} \tag{5.S2}$$

where τ is the thickness of the adsorbed layer, n is the layer's refractive index, n_0 is the refractive index of the sample solution, and $a = dn_0/dc$ represents the rate of change in refractive index of the solution as a function of sample concentration which is fixed at 0.18 cm^3/g in this work [3].

Section B: The physical parameters of acyl-L-carnitines (C_nLC) and surface tension of C_nLCs (n = 12, 14, 16) at the ambient temperature of 23 - 25 °C.

Table 5.S1: The parameters of acyl-L-carnitines used in data analysis for neutron reflection.

Segments	Extended length, τ_e (Å)	Scattering Length, b (Å×10⁻⁵)	Volume, V (Å³)	Scattering length density, ρ (Å⁻² ×10⁻⁶)
Protonanted tail ($C_{11}H_{23}$)	15.4	-12.9	323	-0.40
Deuterated tail ($C_{11}D_{23}$, 98%D)	15.4	226.5	323	7.01
Protonanted tail ($C_{13}H_{27}$)	18.0	-14.6	377	-0.38
Deuterated tail ($C_{13}D_{27}$, 98%D)	18.0	266.5	377	7.06
Protonanted tail ($C_{15}H_{31}$)	20.5	-16.3	430	-0.38
Deuterated tail ($C_{15}D_{31}$, 98%D)	20.5	306.5	430	7.13
Head (hL-carnitine with -C=O)		33.4	255	1.31
D_2O		19.1	30	6.35
CM1.31 (contrast matching the head group, 1.31×10⁻⁶ Å⁻²)				1.31
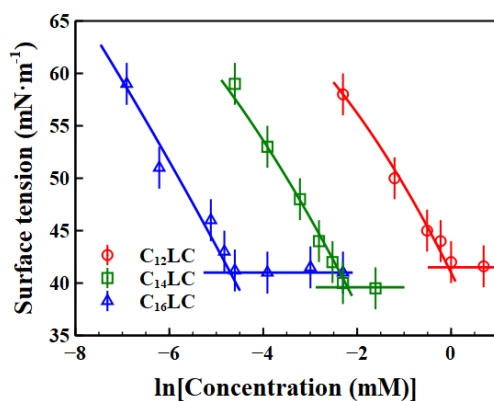
Figure 5.S1. Surface tension of C_nLCs measured in the concentration range studied in this work at pH 7 with ionic strength of 1 mM and room temperature (23-25 °C). The CMC values are 1, 0.1 and 0.01 mM for $C_{12}LC$, $C_{14}LC$ and $C_{16}LC$, respectively. These surfactants remained soluble over the entire concentration range in this study.

Section C: The dynamic adsorption of C_nLC.
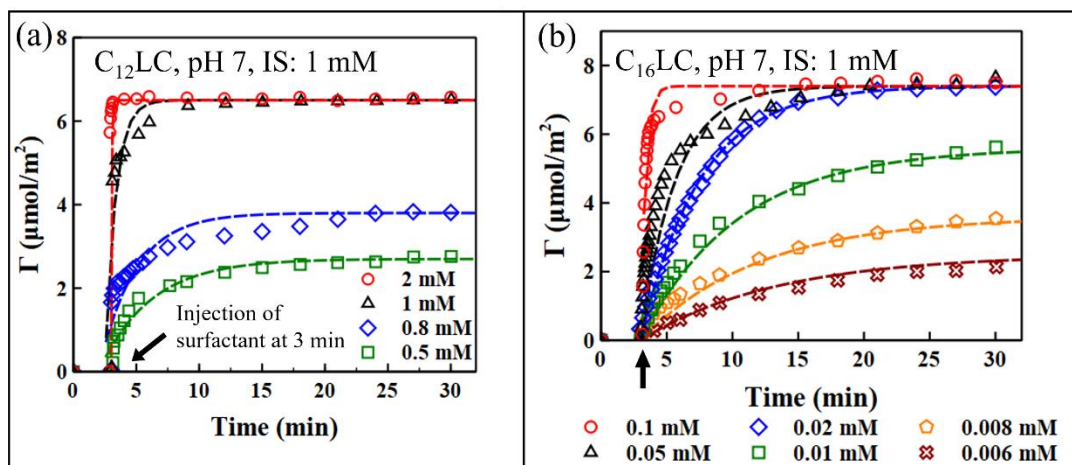
Figure 5.S2. (a) Adsorbed amounts of $C_{12}LC$ at the SiO_2/water interface against time at the concentrations of 0.5, 0.8, 1 and 2 mM at pH 7 and 23 - 25 °C with the ionic strength of 1 mM. The $C_{12}LC$ samples were injected at the 3rd min. The dashed lines represent the best fits from equation (1). (b) Adsorbed amounts of $C_{16}LC$ at SiO_2/water interface against time at the concentrations of 0.006, 0.008, 0.01, 0.02, 0.05 and 0.1 mM at pH 7 and 23 - 25 °C with the ionic strength of 1 mM. The $C_{16}LC$ samples were injected at the 3rd min. The dashed lines represent the best fits from equation (5.1).

Table 5.S2: The best fit parameters from the fitting to the measured adsorption kinetics shown in **Figure 5.S2** using equation (5.1).

	Conc (mM)	A^{-1} ($\mu mol \cdot m^{-2}$)	B ($\mu mol \cdot m^{-2} \cdot min^{-1}$)
C₁₂LC	2	6.54	126.75
	1	6.50	8.00
	0.8	3.80	1.34
	0.5	2.70	0.65
C₁₆LC	0.1	7.50	19.68

0.05	7.45	2.77
0.02	7.42	1.64
0.01	5.60	0.75
0.008	3.60	0.40
0.006	2.50	0.24
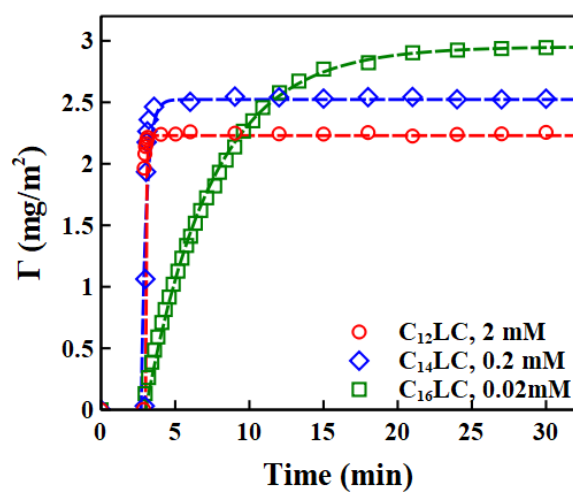
Figure 5.S3. Adsorbed amounts (expressed in mg/m^2) of C$_n$LC at the SiO$_2$/water interface versus time at 2× CMC at pH 7 and 23 - 25 °C with ionic strength of 1 mM. The dashed lines represent the best fits from equation (5.1). The samples were injected at 3 min.

Section D: Adsorption isotherms of C_nLC, NR measurements at pH 7 and the calculations with best fit parameters from NR. The dashed lines represent the best fits using equation (5.3).
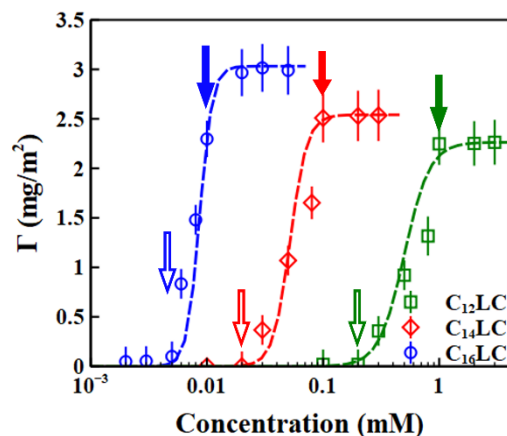
Figure 5.S4. Adsorption isotherms for $C_{12}LC$ (green squares), $C_{14}LC$ (red diamonds), and $C_{16}LC$ (blue circles) at pH 7 (IS: 1 mM) and 23-25 °C. The critical surface aggregation concentrations (CSACs) of C_nLCs are indicated by open arrows and the critical micellar concentrations (CMCs) are indicated by filled arrows. The dashed lines represent the best fits from equation (5.3). The adsorbed amount is expressed in mg/m^2.
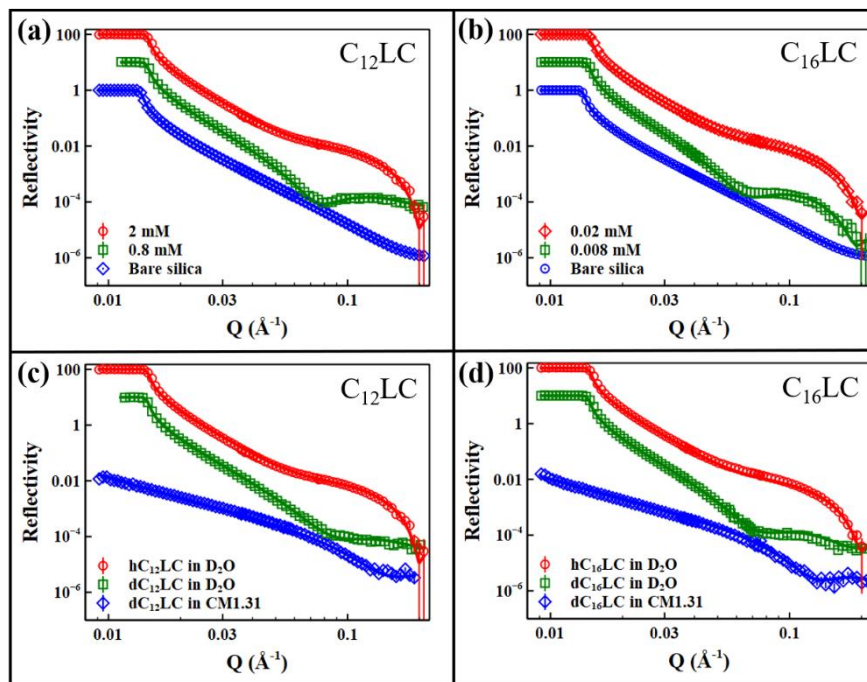
Figure 5.S5. (a) NR profiles of $hC_{12}LC$ at SiO_2/D_2O interface with concentrations of 0, 0.8, and 2 mM under pH 7 and ionic strength of 1 mM. (b) NR profiles of $hC_{16}LC$ at the SiO_2/D_2O interface with concentrations of 0, 0.008, and 0.02 mM under pH 7 and ionic strength of 1 mM. (c) NR profiles of 2 mM $C_{12}LC$ adsorbed at the $SiO_2/water$ interface under pH 7 and IS of 1 mM. These profiles were measured from three contrasts of $hC_{12}LC$ in D_2O (red circles), $dC_{12}LC$ in D_2O (green squares), and $dC_{12}LC$ in CM1.31 (blue diamonds). (d) NR profiles of 2 mM $C_{16}LC$ adsorbed at the $SiO_2/water$ interface under pH 7 and IS of 1 mM. These profiles were measured from three contrasts of $hC_{16}LC$ in D_2O (red circles), $dC_{16}LC$ in D_2O (green squares), and $dC_{16}LC$ in CM1.31 (blue diamonds). Continuous lines represent the best fits to the measured NR data. The data of green squares and red circles have been shifted vertically by the multiplying factor of 10 and 100 for better visualization.

The surfactant volume fraction (φ_s) in the layer, area per molecule (A) and adsorbed amount (Γ) could be calculated from the best fit NR parameters by the following equations:

$$\rho_l = \rho_s \times \varphi_s + \rho_b \times \varphi_b, \tag{5.S3}$$

$$\varphi_s + \varphi_b = 1, \tag{5.S4}$$

$$\varphi_s = \frac{\rho_l - \rho_b}{\rho_s - \rho_b}, \tag{5.S5}$$

$$A = \frac{v_s}{\tau \varphi_s}, \tag{5.S6}$$

$$\Gamma = \frac{1}{A N_a} \tag{5.S7}$$

where ρ_l, ρ_s and ρ_b represent the SLD of the adsorbed layer, surfactant and bulk solution, φ_s and φ_b represent the volume fraction of surfactant and bulk in the adsorbed layer, v_s is the volume of surfactant molecule, τ is the thickness of the layer and N_a is the Avogadro number.

Section E: Adsorbed amount of $C_{12}LC$ and $C_{16}LC$ at different pH measured by SE and NR measurements at pH 3 with ionic strength of 1 mM.
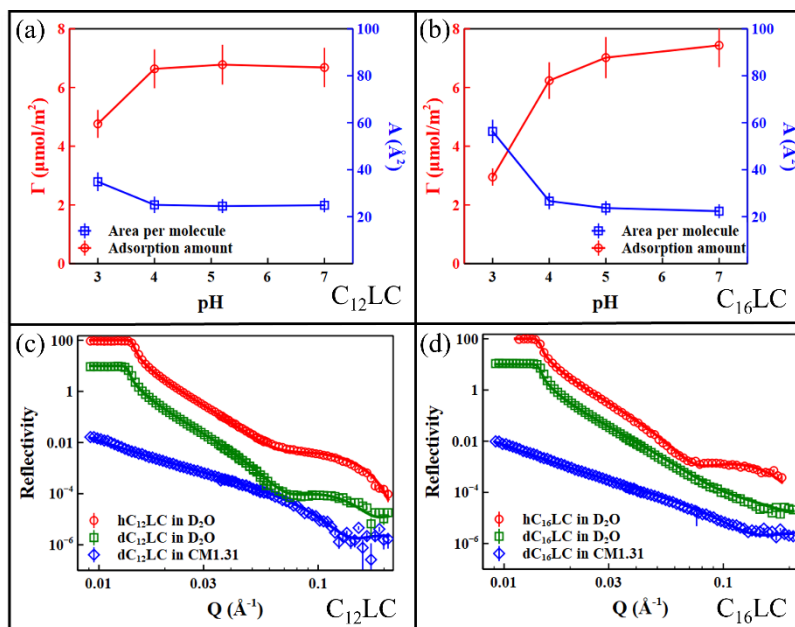
Figure 5.S6. The adsorbed amount (Γ) and area per molecule (A) of (a) $C_{12}LC$ at 2 mM and (b) $C_{12}LC$ at 0.02 mM under different pH. NR profiles of (c) 2 mM $C_{12}LC$ and (d) 0.02 mM $C_{16}LC$ adsorbed at the SiO_2/water interface under pH 3 and ionic strength of 1 mM with three contrasts. Continuous lines represent the best fit for NR data. The data of the green squares and red circles have been shifted vertically by the multiplying factor of 10 and 100 for better visualization.
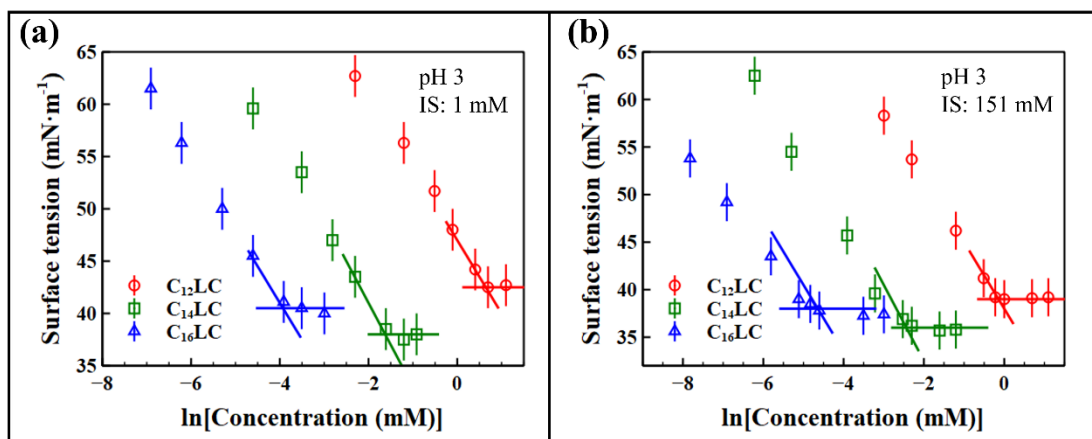
Figure 5.S7. Surface tension of C_nLC at pH 3 as a function of surfactant concentration with ionic strength (IS) of 1 mM (a) and IS of 151 mM (b). The solid lines are drawn to help determine the CMC values. The CMCs are 1.7 ± 0.5, 0.20 ± 0.05 and 0.02 ± 0.05 mM at pH 3 with IS of 1 mM for $C_{12}LC$, $C_{14}LC$ and $C_{16}LC$, respectively. At pH 3 with IS of 151 mM the CMCs are 1.0 ± 0.5, 0.10 ± 0.02 and 0.010 ± 0.005 mM

Section F: Adsorbed amount of $C_{12}LC$ and $C_{16}LC$ at pH 3 with different ionic strength measured by SE and NR measurements at pH 3 with ionic strength of 151 mM.
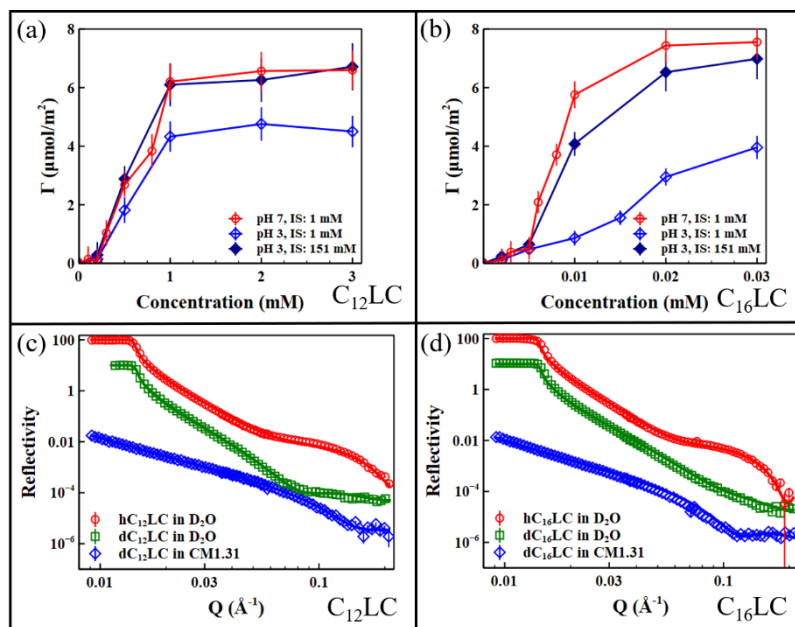
Figure 5.S8. Adsorption isotherms for (a) $C_{12}LC$ and (b) $C_{16}LC$ at pH 3 and room temperature with the ionic strength (IS) of 1 (open diamonds) and 151 mM (filled diamonds). The data at pH 7 is plotted here for comparison. The solid lines are drawn to help read the data. NR profiles of 0.2 mM (c) $C_{12}LC$ and (d) $C_{16}LC$ adsorbed at the SiO_2/water interface under pH 3 and IS of 151 mM. These profiles were measured from three contrasts of $hC_{14}LC$ in D_2O (red circles), $dC_{14}LC$ in D_2O (green squares) and $dC_{14}LC$ in CM1.31 (blue diamonds). Continuous lines represent the best fit for the NR data. The data of green squares and red circles have been shifted vertically by the multiplying factor of 10 and 100 for better visualization.

Section G: The best-fit parameters for the uniform layer and 3-layer model for C_nLC with 3 contrasts at different concentrations, pH and ionic strength (IS).

Table 5.S3: The best-fit parameters from the uniform layer model for C_nLC under 3 isotopic contrasts at different concentrations, pH and ionic strength (IS)

Conc, pH, IS	Contrasts	$\tau \pm 2$ (Å)	$\rho \pm 0.2$ (Å^{-2} × 10^{-6})
	$hC_{12}LC/D_2O$	33	2.0
2 mM, pH 7, IS: 1 mM	$dC_{12}LC/D_2O$	32	4.8
	$dC_{12}LC/CM1.31$	33	3.5
	$hC_{12}LC/D_2O$	29	2.5
2 mM, pH 3, IS: 1 mM	$dC_{12}LC/D_2O$	30	4.9
	$dC_{12}LC/CM1.31$	29	3.0
	$hC_{12}LC/D_2O$	33	2.2
2 mM, pH 3, IS: 151 mM	$dC_{12}LC/D_2O$	32	4.9
	$dC_{12}LC/CM1.31$	32	3.9
	$hC_{14}LC/D_2O$	35	1.8
0.2 mM, pH 7, IS: 1 mM	$dC_{14}LC/D_2O$	35	5.0
	$dC_{14}LC/CM1.31$	34	3.5
	$hC_{14}LC/D_2O$	31	2.4
0.2 mM, pH 3, IS: 1 mM	$dC_{14}LC/D_2O$	32	5.2
	$dC_{14}LC/CM1.31$	31	3.3
	$hC_{14}LC/D_2O$	33	2.0
0.2 mM, pH 3, IS: 151 mM	$dC_{14}LC/D_2O$	35	5.1
	$dC_{14}LC/CM1.31$	33	3.5
	$hC_{16}LC/D_2O$	37	1.5
0.02 mM, pH 7, IS: 1 mM	$dC_{16}LC/D_2O$	37	5.0
	$dC_{16}LC/CM1.31$	36	3.3
	$hC_{16}LC/D_2O$	30	3.4
0.02 mM, pH 3, IS: 1 mM	$dC_{16}LC/D_2O$	31	5.6
	$dC_{16}LC/CM1.31$	31	2.6
0.02 mM, pH 3, IS: 151 mM	$hC_{16}LC/D_2O$	35	2.1

	dC$_{16}$LC/D$_2$O	36		5.4
	dC$_{16}$LC/CM1.31	36		2.8

Table 5.S4: The best-fit parameters for the 3-layer model for C$_n$LC with 3 contrasts at different concentrations, pH and ionic strength (IS)

Conc, pH, IS	Contrasts	$\tau_1 \pm 2$ (Å)	$\rho_1 \pm 0.2$ (Å$^{-2} \times 10^{-6}$)	$\tau_2 \pm 2$ (Å)	$\rho_2 \pm 0.2$ (Å$^{-2} \times 10^{-6}$)	$\tau_3 \pm 2$ (Å)	$\rho_3 \pm 0.2$ (Å$^{-2} \times 10^{-6}$)
2 mM, pH 7, IS: 1 mM	hC$_{12}$LC/D$_2$O	7	2.5	19	1.6	7	2.5
	dC$_{12}$LC/D$_2$O	7	2.5	19	6.6	7	2.5
	dC$_{12}$LC/CM-1.31	6	1.3	18	5.0	7	1.3
2 mM, pH 3, IS: 1 mM	hC$_{12}$LC/D$_2$O	7	3.3	16	2.1	7	3.3
	dC$_{12}$LC/D$_2$O	8	3.1	14	6.4	8	2.4
	dC$_{12}$LC/CM-1.31	7	1.3	16	4.2	7	1.3
2 mM, pH 3, IS: 151 mM	hC$_{12}$LC/D$_2$O	7	2.6	19	1.4	7	2.6
	dC$_{12}$LC/D$_2$O	7	2.7	17	6.4	7	2.7
	dC$_{12}$LC/CM-1.31	7	1.3	18	4.9	7	1.3
0.2 mM, pH 7, IS: 1 mM	hC$_{14}$LC/D$_2$O	7	2.7	20	1.2	7	2.7
	dC$_{14}$LC/D$_2$O	7	2.3	20	6.6	7	2.3
	dC$_{14}$LC/CM-1.31	5	1.3	18	4.6	7	1.3
0.2 mM, pH 3, IS: 1 mM	hC$_{14}$LC/D$_2$O	7	3.2	17	1.9	7	3.2
	dC$_{14}$LC/D$_2$O	5	3.4	18	6.4	5	3.4
	dC$_{14}$LC/CM-1.31	7	1.3	17	4.2	7	1.3
0.2 mM, pH 3, IS: 151 mM	hC$_{14}$LC/D$_2$O	7	2.7	19	1.3	7	2.7
	dC$_{14}$LC/D$_2$O	8	2.8	18	6.6	8	2.8
	dC$_{14}$LC/CM-1.31	5	1.3	17	4.9	7	1.3
0.02 mM, pH 7, IS: 1 mM	hC$_{16}$LC/D$_2$O	7	2.5	22	0.9	7	2.5
	dC$_{16}$LC/D$_2$O	7	2.2	21	6.6	7	2.2
	dC$_{16}$LC/CM-	7	1.3	22	3.9	7	1.3

				1.31		
0.02 mM, pH 3, IS: 1 mM	$hC_{16}LC/D_2O$	7	3.9	17	2.9	7	3.7
	$dC_{16}LC/D_2O$	7	4.0	17	6.5	7	4.2
	$dC_{16}LC/CM-1.31$	7	1.3	17	3.6	7	1.3
0.02 mM, pH 3, IS: 151 mM	$hC_{16}LC/D_2O$	7	2.7	21	2.0	7	2.7
	$dC_{16}LC/D_2O$	7	3.1	21	6.3	7	3.1
	$dC_{16}LC/CM-1.31$	7	1.3	21	3.3	7	1.3

Reference

[1] Z. Li, F. Pan, R. Li, E. Pambou, X. Hu, S. Ruane, D. Ciumac, P. Li, R.J. Welbourn, J.R. Webster, Coadsorption of a Monoclonal Antibody and Nonionic Surfactant at the Sio2/Water Interface, ACS applied materials & interfaces 10(51) (2018) 44257-44266.

[2] J. De Feijter, d.J. Benjamins, F. Veer, Ellipsometry as a Tool to Study the Adsorption Behavior of Synthetic and Biopolymers at the Air–Water Interface, Biopolymers: Original Research on Biomolecules 17(7) (1978) 1759-1772.

[3] J. Wang, D. Jia, K. Tao, C. Wang, X. Zhao, M. Yaseen, H. Xu, G. Que, J.R. Webster, J.R. Lu, Interfacial Assembly of Lipopeptide Surfactants on Octyltrimethoxysilane-Modified Silica Surface, Soft Matter 9(40) (2013) 9684-9691.

Chapter 6 Conclusions and future perspectives

Contents

6.1 Main concluding remarks

As natural biosurfactants, acyl-L-carnitines (C_nLC) play important roles in metabolic processes. Meanwhile, they manifest interesting surface adsorption and solution aggregation inherent of their amphiphilic structure. However, few experiments had been carried out before this project to investigate their basic physicochemical properties. The lack of such basic understanding has limited the effort to exploit their applications. Thus, the understanding of their solubility, solution aggregation and interfacial adsorption from this work is of direct relevance to the further development of their technological uses.

In this project, the aqueous solubility and hydrodynamic sizes of acyl-L-carnitines were investigated by dynamic light scattering (DLS), and the structural features of the micelles were examined by small angle neutron scattering (SANS). Also, surface tension measurements, spectroscopic ellipsometry (SE) and neutron reflection (NR) were used to study the adsorption behavior of C_nLCs at air/water and SiO_2/water interfaces.

Firstly, $C_{14}LC$ and $C_{16}LC$ are hard to dissolve fully in water at high concentrations and room temperature during the preparation of sample solutions, but $C_{12}LC$ shows a better solubility than $C_{14}LC$ and $C_{16}LC$, indicating the effect of acyl chain length. High temperature and low pH solution can help to dissolve the insoluble C_nLC samples. These observations indicate that the aqueous solubility of C_nLCs are dependent on the concentration, temperature and pH and acyl chain length. DLS was employed to detect the appearance/disappearance of insoluble substances because of its high sensitivity to the size of particles and its accurate control of temperature. The results indicated $C_{14}LC$ and $C_{16}LC$ are fully dissolved at around 28 and 43 °C during heating, and the insoluble substances appear in their solutions at around 13 and 33 °C during cooling. These temperature boundaries increase little with increasing concentration. Besides, there is a significant improvement for the solubility of $C_{14}LC$

and $C_{16}LC$ in low pH solutions. However, $C_{12}LC$ is always fully dissolved from 4 – 50 °C up to 200 mM. In this project, all measurements were undertaken in the temperature and concentration ranges where C_nLCs are fully dissolved. DLS was then used to measure the hydrodynamic radii of the aggregation which were found to be 26, 29 and 32 Å for $C_{12}LC$, $C_{14}LC$ and $C_{16}LC$, respectively. SANS was then employed to further investigate the structure of C_nLC micelles. The results showed that the micelles have the core-shell spherical structure with a similar shell thickness of 11 Å, but their core radii increased with acyl chain length. Furthermore, the micellar structures remained unchanged under different concentrations, temperatures, pH and ionic strength as studied in this project. The low pH environment led to strong repulsive interaction between positively charged micelles, but high ionic strength could screen this repulsion. The aggregational properties of surfactants are influenced by the structure of surfactant molecules. Patra et al. synthesized a single chain carnitine derived surfactant with an amide bond between the dodecyl amine and the carboxyl group in carnitine which has a more linear shape compared to the T-shape structure of C_nLC [1]. H-bonding between their head groups strengthens the flat bilayer leading to the formation of vesicles in aqueous solution and the size increases with concentration. Hence, the different structures of the nanoaggregates formed are caused by the position of the hydrophobic chain and the removal of the weak acidic charge [2].

Next, the CMCs were found to be 1, 0.1, and 0.01 mM for $C_{12}LC$, $C_{14}LC$, and $C_{16}LC$ as determined by surface tension measurements, showing a sharp decrease with increasing acyl chain length at pH 7. Ionic strength had no effect on its surface tension and CMC due to its zwitterionic form at this pH. C_nLCs became cationic in the acidic environment, resulting in higher CMC values, but salt addition could decrease the CMC, which is similar to ionic surfactants such as DTAB and SDS [3]. In combination with the Gibbs equation, the values of area per molecule were found to be 46-49 $Å^2$, smaller than those of C_nSO_4Na and C_nPC [4-7]. NR results showed the

C_nLC molecules formed a monolayer at the air/water interface with a thickness of 21-24 Å. The acyl chains in the air region were tilted away from the interface normal, with a tilting angle of 38-48°. The acidic environment had little effect on the thickness of the adsorbed layers, but the repulsion induced by net positive charges of head groups resulted in different head groups packing. However, salt addition could screen this electrostatic interaction.

Next, C_nLC adsorption behavior at the SiO_2/water interface was studied by SE and NR under varied pH from 7 to 3 and ionic strength from 1 to 151 mM. The adsorbed amount remained low until the concentration reached their critical surface aggregation concentrations (CSAC). Below their CMCs, C_nLC molecules formed discrete aggregates on the SiO_2 surface, leading to high water volume fraction. As the concentration increased, more molecules adsorbed into the space between these aggregates on the SiO_2 surface and the adsorbed amount reached the plateau values when the concentrations were over their CMCs. In plateau conditions, NR results showed that C_nLC molecules formed a bilayer with a head-tail-head structure. However, the C_nLC molecules could not fully cover the SiO_2 surface with some water 'holes' in the bilayer. In the acidic environment, the cationic C_nLC micelles adsorbed at the interface with some distance between these micelles, which were caused by the repulsive interaction. As a result, the adsorbed amount had a significant decrease, but this phenomenon could be weakened by the screening effect from high ionic strength.

Overall, C_nLC molecules can aggregate into micelles in the bulk and adsorb at the air/water and SiO_2/water interfaces as normal surfactants. Their micelles have a stable core-shell spherical structure under different concentrations, temperatures, pH and ionic strength. The micelles carry positive charges in the acidic environment due to the protonation of carboxyl groups. C_nLC molecules form a monolayer at the air/water interface and adsorb as aggregates at the SiO_2/water interface. The adsorbed amounts both reach the maximal values at their CMCs, and C_nLC molecules form a

bilayer structure at the SiO_2/water interface above the CMC resulting in the area per molecule being about half of that at the air/water interface under plateau adsorption.

6.2 Future perspectives

This project has focused on the solution aggregation and interfacial adsorption of C_nLCs under different conditions including concentration, temperature, pH, and ionic strength. Different lines of work can be planned in the future to improve our understanding of C_nLCs' antimicrobial ability and potential application in medicine and health care.

First of all, commercial surfactant products are predominantly supplied as mixtures of surfactants. Further experimental studies can look at the changes in solubility, solution aggregation and interfacial adsorption of mixtures of C_nLC with other surfactants including cationic, ionic, zwitterionic, and nonionic surfactants. This is an essential next step towards exploring the potential applications of C_nLCs, as the actual scientific understanding is lacking. The size of the aggregates can be studied by DLS and the structural information can be further examined by SANS experiments.

The interfacial adsorption behaviors of C_nLCs is interesting for further investigation. In this project, air/water and SiO_2/water interfaces were chosen as they are already well known models. In real life applications, there are other conditions that need to be considered, such as roughness, hydrophilicity or hydrophobicity, surface charge and specific chemical nature. Besides, it is also worthy to investigate co-adsorption with protein and the interaction with the model lipid bilayer to explore their suitability in biological, medical, and pharmaceutical fields. These studies could be an important focal point to enhance fundamental understanding of C_nLC interfacial adsorption and explore new insights for their potentially interfacial applications. Langmuir trough can be used to monitor the surface pressure of the lipid layer and NR experiments can be employed to study the structure of the lipid membrane model and the structural difference after interaction with surfactants.

A more practical case is to examine their antimicrobial ability. Alkyl/acyl-L-carnitine esters have been claimed as antimicrobials against a wide range of bacteria, yeasts and fungi [8]. From the work described in this thesis, C_nLC is pH-responsive in the zwitterionic form in neutral pH and in the cationic form in the acidic condition. Ionic surfactants are normally more toxic than zwitterionic or nonionic surfactants. For example, in the toxicity experiment, the survival of 3T3 cells are less than 5% at 1/10 CMC for $C_{12}TAB$ while that of $C_{12}E_6$ is about 65% [3]. The membrane-lytic activity of surfactants is important for their toxicity. The lipid small unilamellar vesicles (SUVs) and spread monolayer are suitable models to study the interactions of the surfactants with membrane models. $C_{12}TAB$ monomers show measurable membrane-lytic activity below its CMC due to the electrostatic attraction between the cationic monomers and anionic membranes [3]. In contrast, disruption of the charged SUVs occurs at CMC for $C_{12}E_6$ where the micelles start to form. The NR experiments with spread lipid monolayer in Langmuir trough show that the cationic amphiphilic peptides can strongly bind to the anionic lipid membranes, but have weak interactions with non-charged zwitterionic membranes, indicating the selectivity of cationic peptides to kill bacteria with low toxicity to the cells [9]. As mentioned above, the charge of C_nLC is pH-responsive due to its weak acidic group (carboxyl). Thus, C_nLC shows good biocompatibility in neutral environments with its zwitterionic form. In acidic environments, the cationic form can enhance its antimicrobial activity. As a result, C_nLC can be potentially employed as a controllable antimicrobial according to different pH conditions, especially in acidic environment. Measurements of the minimum inhibitory concentration (MIC) and dynamic killing experiments could directly evaluate the antimicrobial ability. The interaction between C_nLC and SUVs or lipid monolayer in a Langmuir trough can enhance our understanding to its membrane-lytic activity. These studies are important to future exploitation in their antimicrobial applications.

Another interesting potential use is to employ C_nLC to deliver drugs and release them to targeted sites. Surfactants have been widely used to encapsulate a wide variety of poorly soluble drugs with their vesicular or micellar aggregates in solution [10, 11]. The amount of loaded drug can be estimated by H-NMR spectrum and the structural information can be studied by DLS and SANS [11].Thus, C_nLCs can potentially encapsulate some hydrophobic drugs or nutrients. From our studies, stimuli including temperature, concentration, ionic strength have no effect on the structure of C_nLC micelles which could also increase the stability of drugs and nutrients. The pH-sensitive charge response could be used as a signal to contribute to release these drugs and nutrients in targeted sites, such as the stomach (about pH 2) and skin (about pH 5). Many studies also have shown that some polymers can form hydrogels to deliver drugs [12]. Polymers have great advantages in terms of stimuli responsiveness and could also mitigate the costs. Zwitterionic surfactants have good biocompatibility and can be used in gene delivery and protein protection [1, 13]. Thus, the co-formulated hydrogels of polymers with C_nLC represent another challenging task and the addition of C_nLC can improve the biocompatibility of hydrogels and lead to varied structures under different conditions. But this work requires careful characterisations and tuning for future exploitation.

Molecular dynamics (MD) simulation is fast becoming attractive to support experimental studies [14, 15]. Although it is clear that the surfactant molecules have a trend to form aggregates in aqueous solution and adsorb at the water surface, it is also important for us to focus on these processes [16]. MD simulation could provide insights at the molecular and membrane levels to investigate the aggregation and adsorption behaviors of C_nLCs and their selective membrane interactions which can help explore how the molecular structure affects these behaviors. Stephenson's work introduced the thermodynamic integration free-energy method and indicated which model was closer to the experimental data by evaluating the free-energy change associated with changing micellar composition [16]. Liu's team indicated that the

micellization of surfactant in aqueous is an entropy-driven process and the stability of micelles increases with hydrophobic chain length [17, 18]. However, simulation explorations on drug delivery and interactions with lipid membranes still remain sparse. The difficulty lies in how to mimic the force field and model C_nLC molecules with the lowest computational costs whilst remaining practically relevant and useful. An immediately attractive step would to develop MD capabilities to model NR and SANS data. This effort could lead to structural insights in membranes and micelles that are difficult to extract from any current modelling exercises.

Reference

[1] T. Patra, S. Ghosh, J. Dey, Cationic Vesicles of a Carnitine-Derived Single-Tailed Surfactant: Physicochemical Characterization and Evaluation of in Vitro Gene Transfection Efficiency, Journal of Colloid and Interface Science 436 (2014) 138-145.

[2] H. Liu, X. Hu, Z. Li, K. Fa, H. Gong, K. Ma, M. Liao, P. Li, J.R. Webster, J.T. Petkov, R.K. Thomas, J.R. Lu, Surface Adsorption and Solution Aggregation of a Novel Lauroyl-L-Carnitine Surfactant, Journal of Colloid and Interface Science 591 (2021) 106-114.

[3] F. Pan, Z. Li, H. Gong, J.T. Petkov, J.R. Lu, Membrane-Lytic Actions of Sulphonated Methyl Ester Surfactants and Implications to Bactericidal Effect and Cytotoxicity, Journal of Colloid and Interface Science 531 (2018) 18-27.

[4] J.R. Lu, A. Marrocco, T.J. Su, R.K. Thomas, J. Penfold, Adsorption of Dodecyl Sulfate Surfactants with Monovalent Metal Counterions at the Air-Water Interface Studied by Neutron Reflection and Surface Tension, Journal of Colloid and Interface Science 158(2) (1993) 303-316.

[5] M. Koshinuma, T. Sasaki, Activity Measurement and Colloid Chemical Studies of Aqueous Sodium Tetradecyl Sulfate Solutions, Bulletin of the Chemical Society of Japan 48(10) (1975) 2755-2759.

[6] A. Zdziennicka, K. Szymczyk, J. Krawczyk, B. Jańczuk, Activity and Thermodynamic Parameters of Some Surfactants Adsorption at the Water–Air Interface, Fluid Phase Equilibria 318 (2012) 25-33.

[7] M. Yaseen, J. Lu, J. Webster, J. Penfold, Adsorption of Single Chain Zwitterionic Phosphocholine Surfactants: Effects of Length of Alkyl Chain and Head Group Linker, Biophysical Chemistry 117(3) (2005) 263-273.

[8] M. Calvani, L. Critelli, G. Gallo, F. Giorgi, G. Gramiccioli, M. Santaniello, N. Scafetta, M.O. Tinti, F. De Angelis, L-Carnitine Esters as "Soft", Broad-Spectrum Antimicrobial Amphiphiles, Journal of Medicinal Chemistry 41(13) (1998) 2227-2233.

[9] H. Gong, J. Zhang, X. Hu, Z. Li, K. Fa, H. Liu, T.A. Waigh, A. McBain, J.R. Lu, Hydrophobic Control of the Bioactivity and Cytotoxicity of De Novo-Designed Antimicrobial Peptides, ACS Appl Mater Interfaces 11(38) (2019) 34609-34620.

[10] G.P. Kumar, P. Rajeshwarrao, Nonionic Surfactant Vesicular Systems for Effective Drug Delivery—an Overview, Acta Pharmaceutica Sinica B 1(4) (2011) 208-219.

[11] X. Hu, H. Gong, Z. Li, S. Ruane, H. Liu, P. Hollowell, E. Pambou, C. Bawn, S. King, S. Rogers, How Does Solubilisation of Plant Waxes into Nonionic Surfactant Micelles Affect Pesticide Release?, Journal of Colloid and Interface Science 556 (2019) 650-657.

[12] M. Cao, Y. Wang, X. Hu, H. Gong, R. Li, H. Cox, J. Zhang, T.A. Waigh, H. Xu, J.R. Lu, Reversible Thermoresponsive Peptide–Pnipam Hydrogels for Controlled Drug Delivery, Biomacromolecules 20(9) (2019) 3601-3610.

[13] A. Erfani, N.H. Flynn, J.D. Ramsey, C.P. Aichele, Increasing Protein Stability by Association with Zwitterionic Amphiphile Cocamidopropyl Betaine, Journal of Molecular Liquids 295 (2019) 111631.

[14] M. Poorsargol, M. Alimohammadian, B. Sohrabi, et al.Dispersion of graphene using surfactant mixtures: Experimental and molecular dynamics simulation studies[J].Applied Surface Science,2019, 464: 440-450.

[15] Z. Liu, G. Zhou, S. Li, C. Wang, R. Liu, W. Jiang, Molecular Dynamics Simulation and Experimental Characterization of Anionic Surfactant: Influence on Wettability of Low-Rank Coal, Fuel 279 (2020) 118323.

[16] P. Shi, H. Zhang, L. Lin, C. Song, Q. Chen, Z. Li, Molecular Dynamics Simulation of Four Typical Surfactants in Aqueous Solution, RSC advances 9(6) (2019) 3224-3231.

[17] G. Liu, D. Gu, H. Liu, W. Ding, Z. Li, Enthalpy–Entropy Compensation of Ionic Liquid-Type Gemini Imidazolium Surfactants in Aqueous Solutions: A Free Energy Perturbation Study, Journal of colloid and interface science 358(2) (2011) 521-526.

[18] G. Liu, D. Gu, H. Liu, W. Ding, H. Luan, Y. Lou, Thermodynamic Properties of Micellization of Sulfobetaine-Type Zwitterionic Gemini Surfactants in Aqueous Solutions–a Free Energy Perturbation Study, Journal of colloid and interface science 375(1) (2012) 148-153.